(a) $K^{*-}(892)$ CA mass peak region

(b) $K^{*-}(1430)$ and $K^{*-}(1680)$ mass region

(c) $K^{*+}(892)$ DCS mass region

(d) higher mass $(K_S\pi^+)$ projection

(e) $\rho - \omega$ mixing interference region

(f) higher mass $(\pi^+\pi^-)$ projection with $f_0(980)$

Figure 3.16: *Zoom of particular regions of the Breit-Wigner fit result: $K^*(892)$ mass peak region, $K^*(1430)$ and $K^*(1680)$ on the Cabibbo allowed $(K_s\pi^-)$ projection, the region of interference between the CA-DCS decays involving $K^*(892)$ mesons, the higher mass $(K_S\pi^+)$ region, the $\rho - \omega$ mixing interference region, the higher mass $(\pi^+\pi^-)$ projection with $f_0(980)$.*

where $F_1(s)$ is the contribution of $\pi\pi$ S-wave states,

$$F_1(s) = \sum_j [I - iK(s)\rho(s)]^{-1}_{1j} P_j(s) . \tag{3.13}$$

Here, s is the squared mass of the $\pi\pi$ system $(m^2_{\pi^+\pi^-})$, I is the identity matrix, K is the matrix describing the S-wave scattering process, ρ is the phase-space matrix, and P is the initial production vector [37],

$$P_j(s) = \sum_\alpha \frac{\beta_\alpha g_j^\alpha}{m_\alpha^2 - s} + f_{1j}^{\text{prod}} \frac{1 - s_0^{\text{scatt}}}{s - s_0^{\text{scatt}}} . \tag{3.14}$$

The index j represents the jth channel ($1 = \pi\pi$, $2 = K\overline{K}$, $3 =$multi-mesons (referred to a final state with four pions), $4 = \eta\eta$, $5 = \eta\eta'$ [46]). The parameters β_α and f_{11}^{prod} represent the amplitude of the different components of the $\pi\pi$ S-wave and will be let float in the fit.

The K-matrix parameters are obtained from Ref. [46] from a global fit of the available $\pi\pi$ scattering data from threshold up to 1900 MeV/c^2. The K-matrix parameterization is:

$$K_{ij}(s) = \left\{ \sum_\alpha \frac{g_i^\alpha g_j^\alpha}{m_\alpha^2 - s} + f_{ij}^{\text{scatt}} \frac{1.0 - s_0^{\text{scatt}}}{s - s_0^{\text{scatt}}} \right\} \frac{(1 - s_{A0})}{(s - s_{A0})}(s - s_A m_\pi^2/2), \tag{3.15}$$

where g_i^α is the coupling constant of the K-matrix pole m_α to the ith channel. The parameters f_{ij}^{scatt} and s_0^{scatt} describe the slowly-varying part of the K-matrix element. The Adler zero factor $(1 - s_{A0})(s - s_A m_\pi^2/2)/(s - s_{A0})$ [47] suppresses false kinematical singularity at $s = 0$ in the physical region near the $\pi\pi$ threshold [48]. The production vector has the same poles as the K-matrix, otherwise the F_1 vector would vanish (diverge) at the K-matrix (P-vector) poles. The parameter values used in this analysis are listed in Tab. 3.4 [49]. The parameters f_{ij}^{scatt}, for $i \neq 1$, are all set to zero since they are not related to the $\pi\pi$ scattering process.

The phase space matrix is diagonal, $\rho_{ij}(s) = \delta_{ij}\rho_i(s)$, where

$$\rho_i(s) = \sqrt{1 - \frac{(m_{1i} + m_{2i})^2}{s}} \tag{3.16}$$

with m_{1i} (m_{2i}) denoting the mass of the first (second) final state particle of the ith channel. The normalization is such that $\rho_i \rightarrow 1$ as $s \rightarrow \infty$. An analytic continuation of the ρ_i

m_α	$g^\alpha_{\pi\pi}$	$g^\alpha_{K\overline{K}}$	$g^\alpha_{4\pi}$	$g^\alpha_{\eta\eta}$	$g^\alpha_{\eta\eta'}$
0.651	0.229	-0.554	0.000	-0.399	-0.346
1.204	0.941	0.551	0.000	0.391	0.315
1.558	0.369	0.239	0.556	0.183	0.187
1.210	0.337	0.409	0.857	0.199	-0.010
1.822	0.182	-0.176	-0.797	-0.004	0.224
	f^{scatt}_{11}	f^{scatt}_{12}	f^{scatt}_{13}	f^{scatt}_{14}	f^{scatt}_{15}
	0.234	0.150	-0.206	0.328	0.354
	s^{scatt}_0	s_{A0}	s_A		
	-3.926	-0.15	1		

Table 3.4: *K-matrix parameters as obtained from Refs. [46, 49]. Pole masses (m_α) and coupling constants (g^α_i) are given in GeV/c^2, s^{scatt}_0 and s_{A0} are in GeV^2/c^4.*

functions below threshold is used. The expression of the multi-meson state phase space is written as [46]

$$\rho_3(s) \;\; = \left\{ \begin{array}{ll} \rho_{31} & s < 1 \; GeV^2 \\ \rho_{32} & s > 1 \; GeV^2 \end{array} \right\} \tag{3.17}$$

where

$$\rho_{31}(s) \;\; = \;\; \rho_0 \int\int \frac{ds_1}{\pi}\frac{ds_2}{\pi} \frac{M^2\Gamma(s_1)\Gamma(s_2)\sqrt{(s+s_1-s_2)^2-4ss_1}}{s[(M^2-s_1)^2+M^2\Gamma^2(s_1)]\,[(M^2-s_2)^2+M^2\Gamma^2(s_2)]} \; ,$$
$$\rho_{32}(s) \;\; = \;\; \frac{s-16m_\pi^2}{s} \; . \tag{3.18}$$

Here s_1 and s_2 are the squared invariant mass of the two di-pion systems, M is the ρ meson mass, and $\Gamma(s)$ is the energy-dependent width. The factor ρ_0 provides the continuity of $\rho_3(s)$ at $s = 1 \; GeV^2$. Energy conservation in the di-pion system must be satisfied when calculating the integral. This complicated expression reveals the fact that the ρ meson has an intrinsic width. Setting $\Gamma(s) = \delta(s)$, where δ is the Dirac δ function, the usual two-body phase space factor is obtained.

Fig. 3.17 shows the real part of the $\pi\pi$ phase space factor and the 4π phase-space factor. Fig. 3.18 shows the K-matrix solution of the AS parameterization [46] of the $\pi\pi$ scattering wave. The left plot shows the $\pi\pi$ S-wave intensity, where the absence of a simple Breit-Wigner-like structure is apparent. The right plot shows the Argand Plot Diagram for the $\pi\pi$ S-wave: it is clear that K satisfies unitarity, which is a fundamental requirement of the S-matrix. In contrast, it is well known that unitarity is not respected generally in the BW model. Fig. 3.19 shows the $\pi\pi$ scattering phase shift. There is a
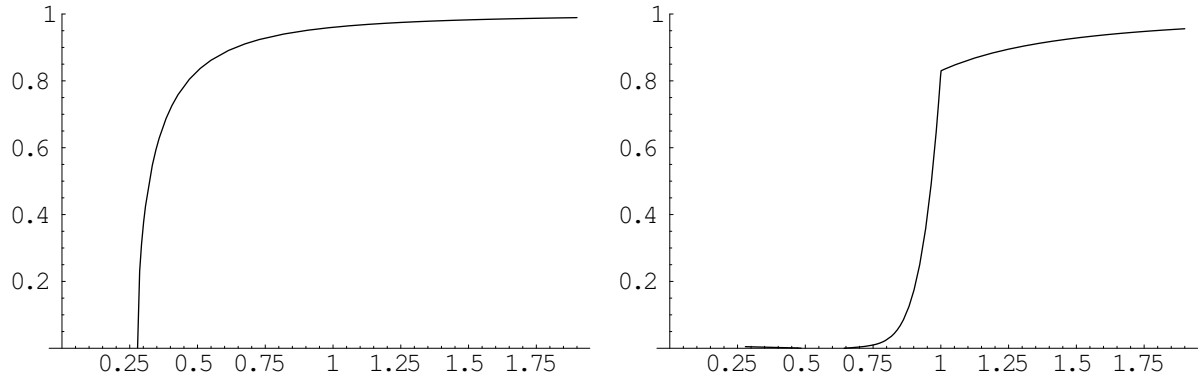
Figure 3.17: **Left:** *The $\pi\pi$ phase-space factor.* **Right:** *The 4π phase-space factor. $\rho(s) \to 1$ as $s \to \infty$. The x axis represents $\sqrt{s}$ in GeV.*
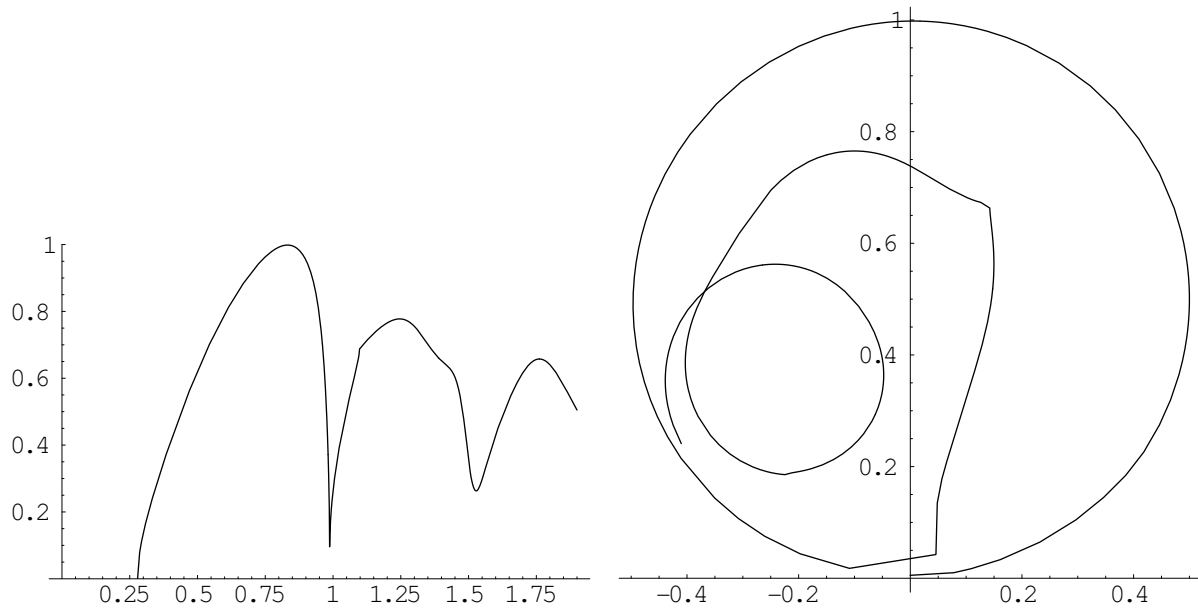

Figure 3.18: **Left:** *The $\pi\pi$ S-wave intensity, showing the lack of a simple Breit-Wigner resonance structure. The x axis represents $\sqrt{s}$ in GeV.* **Right:** *The Argand Plot Diagram for the $\pi\pi$ S-wave component, showing the unitarity of the K-matrix parameterization.*
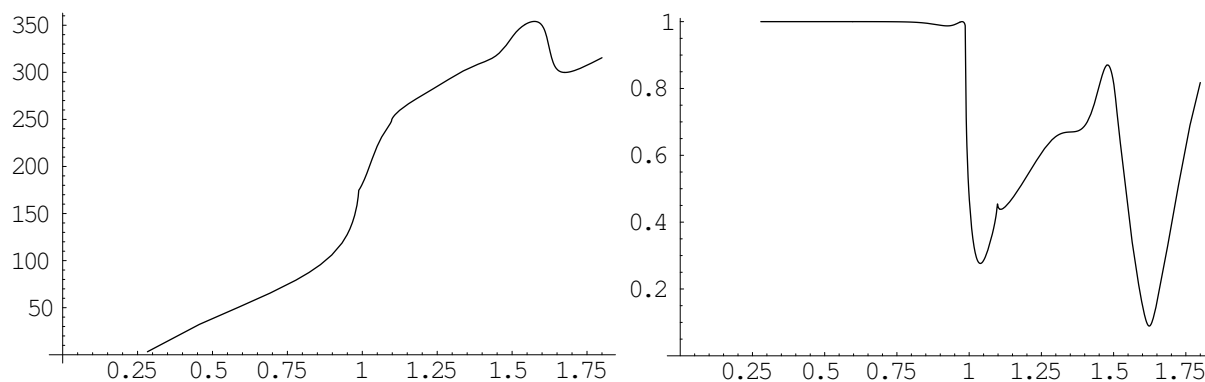
Figure 3.19: **Left:** *The $\pi\pi$ S-wave phase shift.* **Right:** *The elasticity plot, indicating the purely-elastic nature of the scattering process below 1 GeV. The x axis represents $\sqrt{s}$ in GeV.*
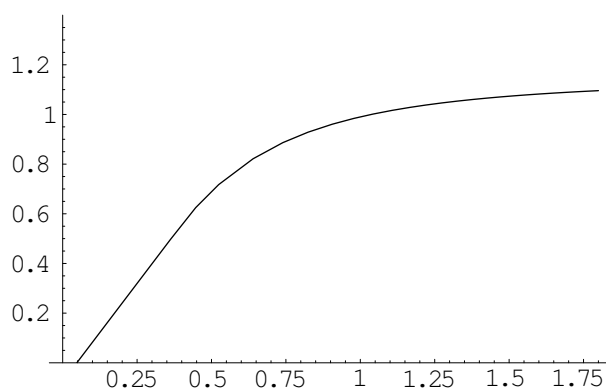

Figure 3.20: *The Adler zero factor. The $\pi\pi$ threshold is suppressed when s near the threshold. The x axis represents $\sqrt{s}$ in GeV.*

strong phase variation around $\sqrt{s} = 1$ GeV and 1.5 GeV, which corresponds to the narrow $f_0(980)$ and $f_0(1500)$ scalar resonances. The right plot shows the elasticity plot of for $\pi\pi$ scattering. The process is purely elastic up to 1 GeV, while new channels (*e.g.* $K\bar{K}$) open up at higher energies and the scattering process becomes inelastic.

The masses and the widths of the other resonances are the same used for the Breit-Wigner fit except the $K^*(1680)$, which is incorrectly averaged by the PDG [50]. The LASS experiment found the $K^*(1680)$ in the $K^-p \rightarrow K^-\pi^+n$ and $K^-p \rightarrow \overline{K^0}\pi^+\pi^-n$ channels, but with quite different masses and widths. Since only the $K^*(1680) \rightarrow K\pi$ channel is considered, the average value should not be used. Tab. 3.5 lists the masses and widths of the resonances used by the K-matrix fit.

3.3.2 Fit results

An unbinned maximum-likelihood fit is used to describe the population on the Dalitz plot and to extract the Real and the Imaginary part of the complex amplitude of the different components: $Re\{a_r e^{i\phi_r}\}$ and $Im\{a_r e^{i\phi_r}\}$. The use of the Cartesian coordinates helps to better estimate the components with lower amplitudes. The likelihood function is written in the following way:

$$L = x \cdot P_{sig} + (1 - x) \cdot P_{bkg} \ , \tag{3.19}$$

where

$$P_{sig}(m_\pm^2, m_\mp^2) = \frac{\epsilon(m_\pm^2, m_\mp^2) \left| f(m_\pm^2, m_\mp^2) \right|^2}{\int \epsilon(m_\pm^2, m_\mp^2) \left| f(m_\pm^2, m_\mp^2) \right|^2 d\mathcal{DP}} \ . \tag{3.20}$$

Here x is the fraction of the signal events and $1 - x$ is the fraction of background events. $f(m_\pm^2, m_\mp^2)$ is the signal Dalitz pdf which is described in Sec. 3.3.1. The background Dalitz distribution $P_{bkg}(m_\pm^2, m_\mp^2)$ is described in Sec. 3.1.4. The efficiency $\epsilon(m_\pm^2, m_\mp^2)$ is determined in signal Monte Carlo simulation, where the D^0 is allowed to decay isotropically (Sec. 3.1.5).

Tab. 3.6 gives the result of the K-Matrix Dalitz fit. Fig. 3.23 shows the Dalitz distribution of the $\pi\pi$ S-wave component resulting from the K-Matrix fit and the sum of the four $\pi\pi$ scalar resonances from the Breit-Wigner fit. Fig. 3.21 shows projections of the fit result on top of data distributions and Fig. 3.22 shows zoom of particular regions of the K-Matrix fit result.

Resonance	Mass (MeV/c^2)	Width (MeV/c^2)	Spin
$K^*(892)$	891.66	50.8	1
$K_0^*(1430)$	1412	294	0
$K_2^*(1430)$	1425.6	98.5	2
$K^*(1680)$	1677	205	1
$\rho^0(770)$	775.8	146.4	1
$\omega(782)$	782.6	8.5	1
$f_2(1270)$	1275.4	185.1	2
$\rho(1450)$	1406	455	1

Table 3.5: *Values for the masses and widths of the resonances used for the fit in the K-matrix model. Besides $K^*(1680)$, other values are fixed according to the PDG2004 [41] values.*

Component	$Re\{a_r e^{i\phi_r}\}$	$Im\{a_r e^{i\phi_r}\}$	Fit fraction (%)
$K^*(892)^-$	-1.127 ± 0.013	1.370 ± 0.012	59.71
$K_0^*(1430)^-$	2.473 ± 0.044	-0.699 ± 0.041	8.73
$K_2^*(1430)^-$	0.772 ± 0.023	-0.774 ± 0.028	2.84
$K^*(1410)^-$	-0.106 ± 0.030	0.037 ± 0.023	0.02
$K^*(1680)^-$	-1.268 ± 0.121	0.304 ± 0.108	0.75
$K^*(892)^+$	0.118 ± 0.005	-0.135 ± 0.004	0.61
$K_0^*(1430)^+$	0.388 ± 0.035	-0.149 ± 0.039	0.23
$K_2^*(1430)^+$	0.055 ± 0.022	-0.049 ± 0.023	0.01
$\rho(770)$	1 (fixed)	0 (fixed)	22.38
$\omega(782)$	-0.022 ± 0.001	0.034 ± 0.001	0.59
$f_2(1270)$	0.834 ± 0.023	-0.423 ± 0.029	3.09
$\rho(1450)$	0.410 ± 0.040	-0.043 ± 0.067	0.15
β_1	-3.338 ± 0.068	1.854 ± 0.080	
β_2	8.957 ± 0.113	2.467 ± 0.220	
β_4	14.163 ± 0.404	-0.879 ± 0.372	
f_{11}^{prod}	-10.008 ± 0.181	-4.756 ± 0.202	
sum of $\pi^+\pi^-$ S-wave			15.48

Table 3.6: *Complex amplitudes $a_r e^{i\phi_r}$ and fit fractions of the different components ($K_S\pi^-$ and $K_S\pi^+$ resonances, and $\pi^+\pi^-$ poles) obtained from the fit of the $D^0 \to K_S\pi^-\pi^+$ Dalitz distribution from $D^{*+} \to D^0\pi^+$ events. Errors are statistical only. Masses and widths of all resonances are taken from [41], while the pole masses and scattering data are from [46, 49]. The fit fraction is defined for the resonance terms ($\pi\pi$ S-wave term) as the integral of $a_r^2|\mathcal{A}_r(m_-^2, m_+^2)|^2$ ($|F_1(s)|^2$) over the Dalitz plane divided by the integral of $|\mathcal{A}_D(m_-^2, m_+^2)|^2$. The sum of fit fractions is 1.15.*

(a) $M^2_{K_S\pi^-}$

(b) $M^2_{K_S\pi^+}$

(c) $M^2_{pi^+\pi^-}$
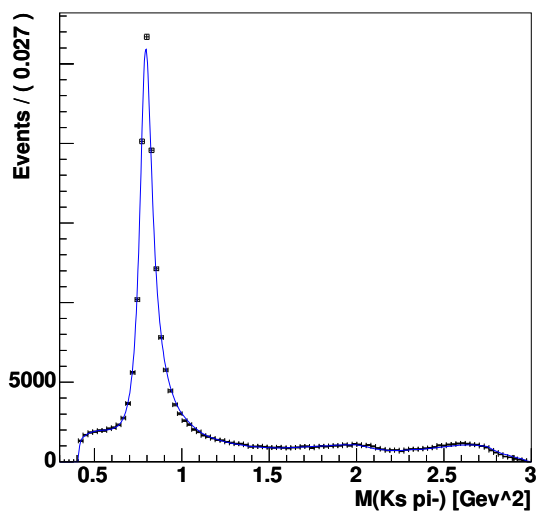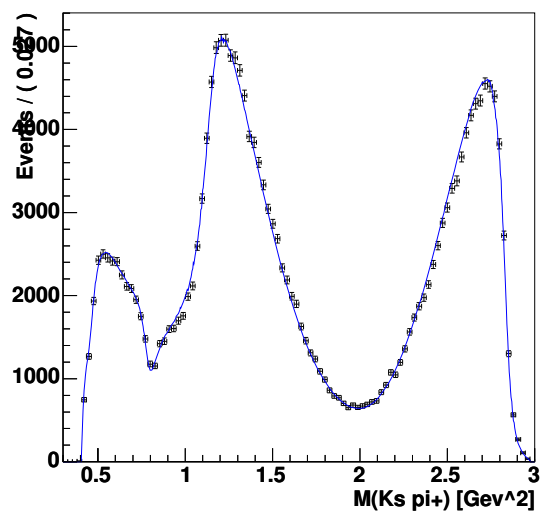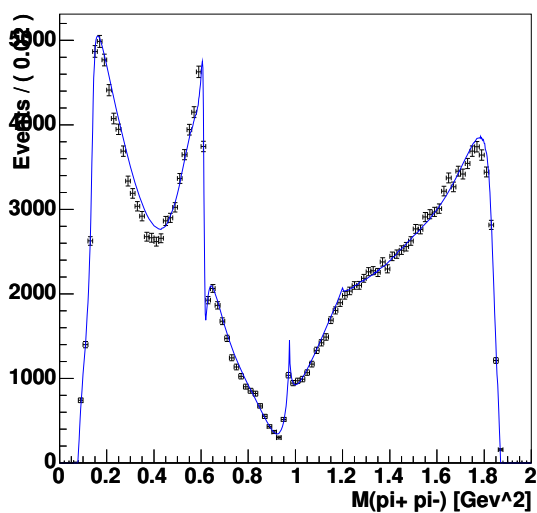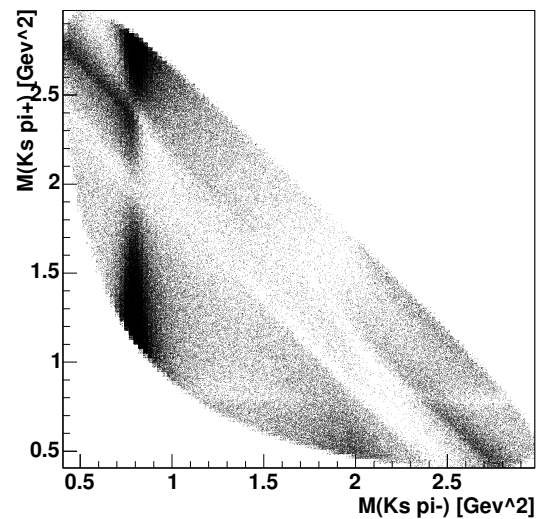
(d) Dalitz plot

Figure 3.21: *Result of the K-Matrix fit to the* $D^0 \to K_s\pi^-\pi^+$ *Dalitz plot, using the flavor tagged D sample from the continuum :* $D^{*\pm} \to D^0\pi^{\pm}_s$. *The three projections are displayed : Cabibbo allowed* $(K_s\pi^-)$, *the* $(K_s\pi^+)$ *and the* $(\pi^+\pi^-)$. *The Dalitz distribution of generated events according to the fit result is also shown.*
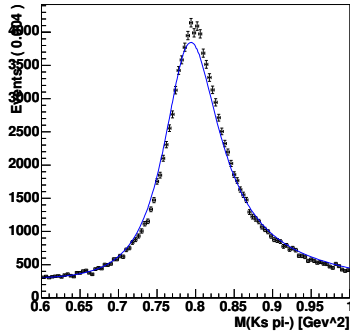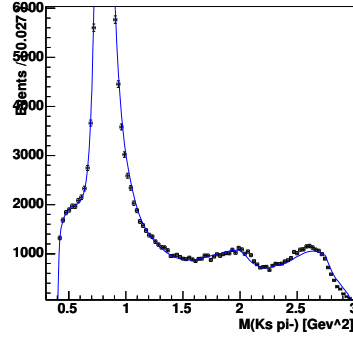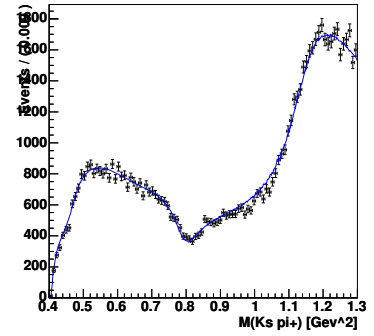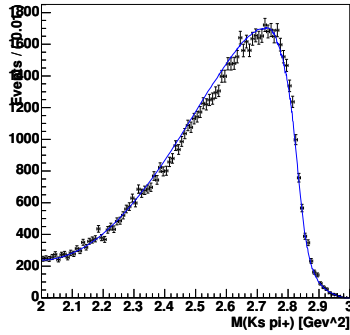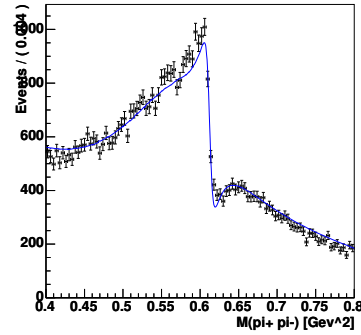
(a) $K^{*-}(892)$ CA mass peak region

(b) $K^{*-}(1430)$ and $K^{*-}(1680)$ mass region

(c) $K^{*+}(892)$ DCS mass region

(d) higher mass $(K_S\pi^+)$ projection

(e) $\rho - \omega$ mixing interference region
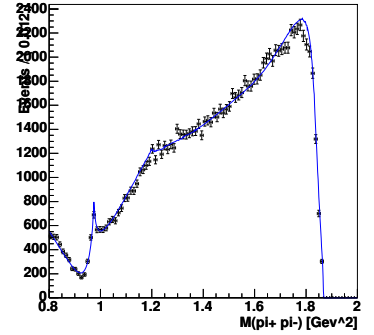
(f) higher mass $(\pi^+\pi^-)$ projection with $f_0(980)$

Figure 3.22: *Zoom of particular regions of the K-Matrix fit result: $K^*(892)$ mass peak region, $K^*(1430)$ and $K^*(1680)$ on the Cabibbo allowed $(K_s\pi^-)$ projection, the region of interference between the CA-DCS decays involving $K^*(892)$ mesons, the higher mass $(K_S\pi^+)$ region, the $\rho - \omega$ mixing interference region, the higher mass $(\pi^+\pi^-)$ projection with $f_0(980)$.*

(a) K-Matrix fit   (b) Breit-Wigner fit

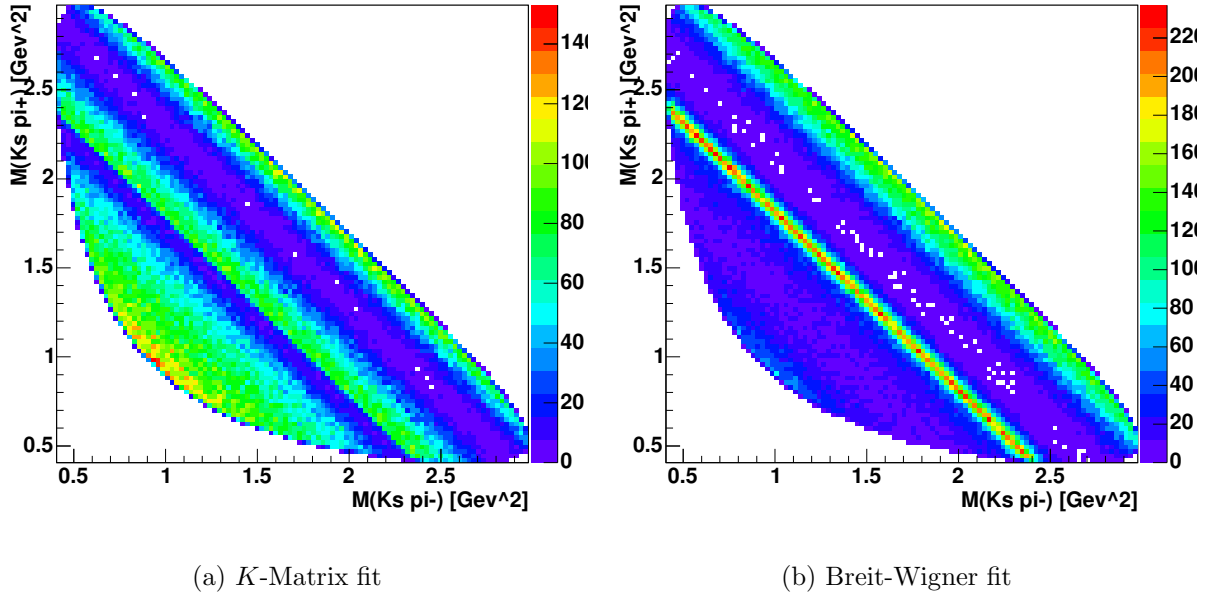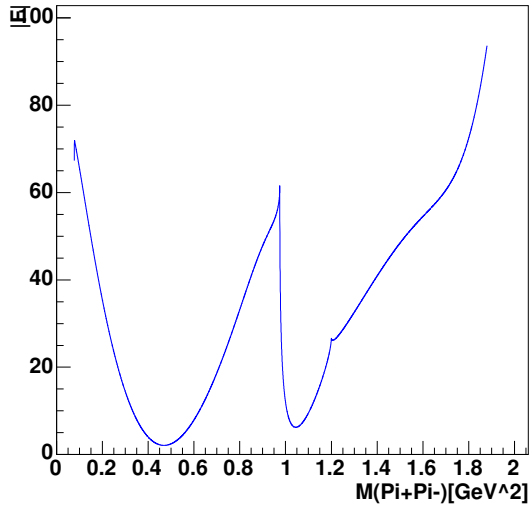Figure 3.23: *Dalitz distribution of the $\pi\pi$ S-wave component resulting from the K-Matrix fit and the sum of the four $\pi\pi$ scalar resonances from the Breit-Wigner fit.*

3.4   Fits comparison

Both Breit-Wigner and K-Matrix fit give a good description of the data. The Breit-Wigner fit needs to introduce two non-established resonances σ and σ'. This is due to the fact that the Breit-Wigner parameterization works only in case of isolated resonances. The $\pi\pi$ S-wave component, instead, is composed of different contributions that overlap significantly. K-Matrix parameterization gives the correct parameterization in the case of overlapping resonances and does not need the presence of the two resonances σ and σ'.

Fig. 3.24 shows amplitude and phase of the F-vector (see. Eq. 3.13) resulting from the K-Matrix fit and the corresponding quantity, defined as the sum of the four scalar $\pi\pi$ Breit-Wigner functions, resulting from the Breit-Wigner fit. Both amplitude and phase shapes result quite different in the two cases; in particular the $f_0(980)$ peak presents a very different shape.

Fig. 3.25 shows the phase in function of the Dalitz plot for the two fits and the difference of the two fits result. The value of the phase is sensibly different only in the regions of the $f_0(980)$ and σ. Since these regions give small sensitivity to the γ

(a) KM fit: amplitude of the F vector
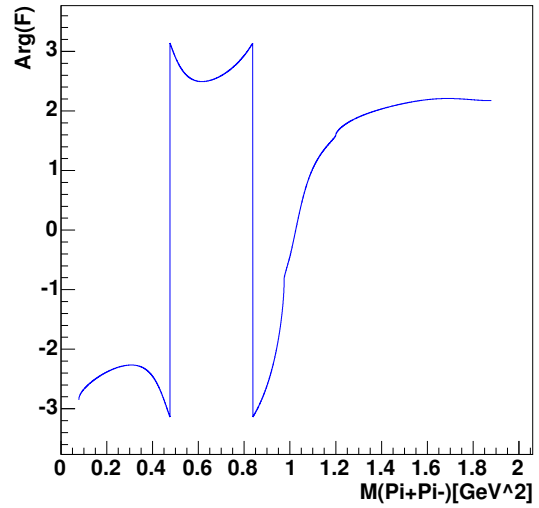
(b) KM fit: phase of the F vector [rad.]
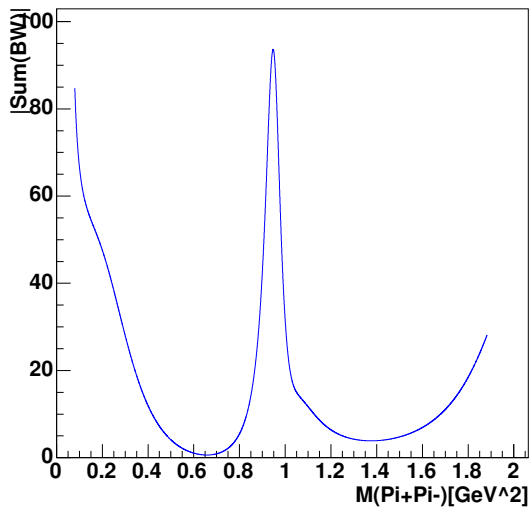
(c) BW fit: amplitude of the $\pi\pi$ S-wave
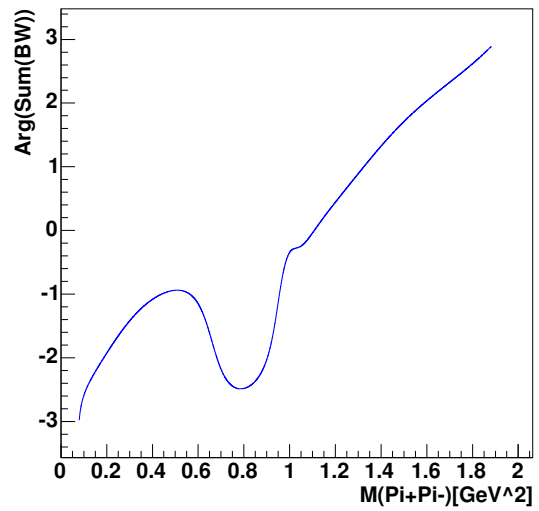
(d) BW fit: phase of the $\pi\pi$ S-wave [rad.]

Figure 3.24: *Amplitude and phase of the F-vector (see. Eq. 3.13) resulting from the K-Matrix fit and the corresponding quantity, defined as the sum of the four scalar $\pi\pi$ Breit-Wigner function, resulting from the Breit-Wigner fit.*

(a) Phase of the KM fit result as a function of the Dalitz plot [rad.]

(b) Phase of the BW fit result as a function of the Dalitz plot [rad.]

(c) Difference of the phase of the two fits result [rad.]

(d) Difference of the phase of the two fits result [rad.]
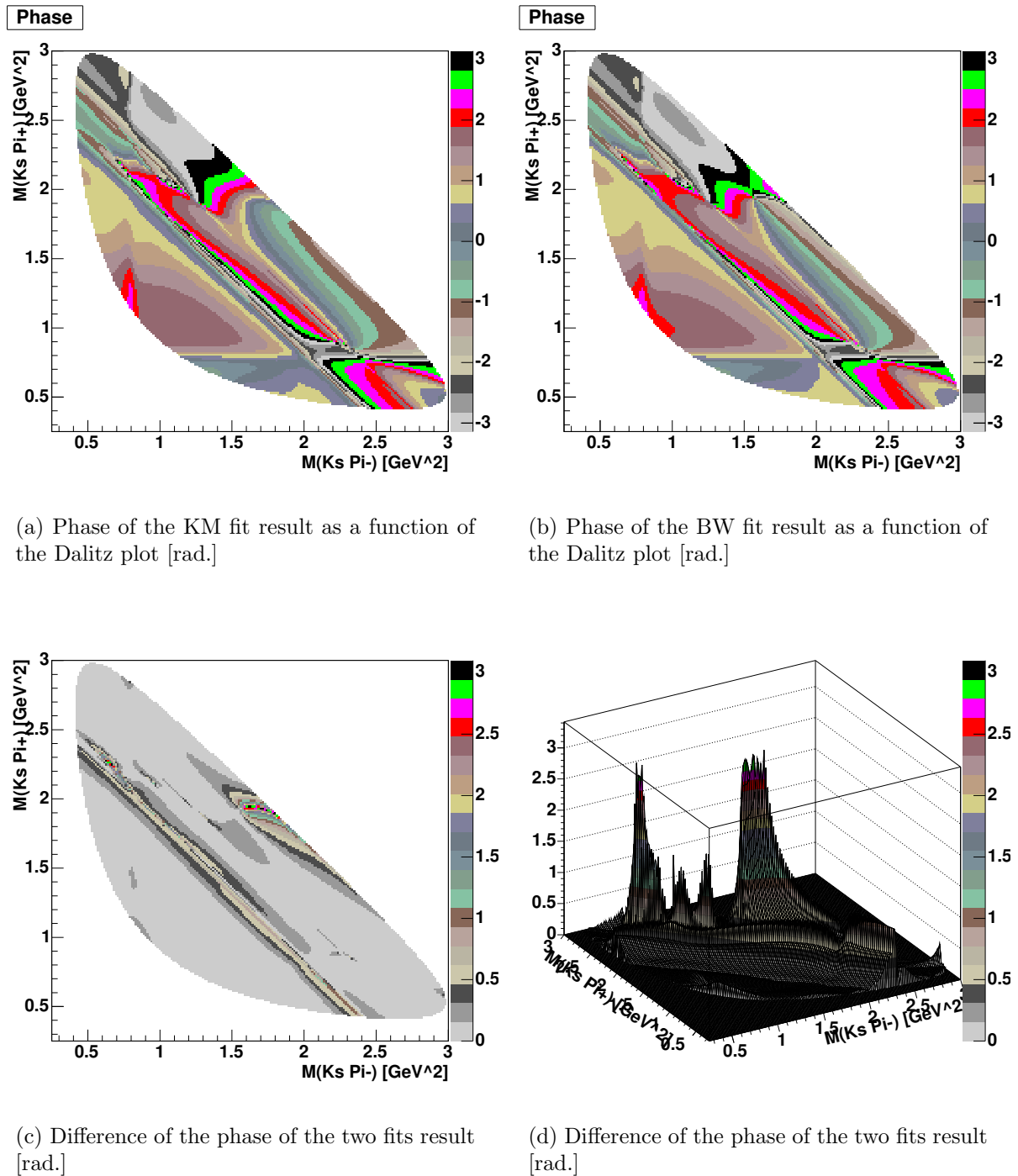
Figure 3.25: *Phase in function of the Dalitz plot for the two fits result and the difference of the two.*

measurement (see Sec. 5.2) it is expected to have a small systematic effect on γ coming from the parameterization of the $\pi\pi$ S-wave component.

The sum of the fit fractions is smaller in the K-matrix fit (KM=1.15, BW=1.24). This is due to the minor number of components in the K-matrix fit: four $\pi\pi$ scalar resonances in the Breit-Wigner fit and only the F-vector in the K-matrix fit. The fit fractions of the other components remain practically unchanged.

Chapter 4

Event selection

4.1 Introduction

This chapter presents the B meson reconstruction. The importance of the different discriminant variables and the background composition are discussed and the fixed parameters of the Likelihood function used for the extraction of the CP parameters are given. A detailed description of the Likelihood function will be provided in Chapter 5.

The B mesons are reconstructed in three decay modes: $B^- \to \tilde{D}^0 K^-$, $B^- \to \tilde{D}^{*0} K^-$ and $B^- \to \tilde{D}^0 K^{*-}$. The B meson decays are reconstructed from the informations recorded from the different detectors in the interactions with the decays final states. Then the informations coming from the single detectors are combined in order to produce B candidates and, at the end, the candidate with the larger probability to be a real particle is chosen.

4.1.1 Pre-selection

The first step of the event selection, common to all the decay modes under study, is the selection of multihadron events among the events logged by the on-line data acquisition chain; many of them are in fact due, not to e^+e^- collision chain but to beam-gas or beam-wall interaction.

A clockwise frame, called laboratory frame, is used with the z axis along the electron beam line, the y axis along the vertical line toward the up direction with the origin in the interaction point and the x axis along the center of the PEP-II ring. The polar angle θ is evaluated from the z axis, the azimuthal angle ϕ is evaluated from the x axis.

Multihadron events are requested to have a minimum of three charged tracks in a fiducial angular region $(0.41 < \theta < 2.54)$rad. The tracks above are requested to have a

momentum less than 10 GeV/c (to avoid non physical tracks), to be reconstructed in the DCH and to originate within 1.5 cm in the xy plane (transverse to the beam axis) and 10 cm on z (along the beam axis) of the nominal beam-spot position. The primary vertex, constructed from the tracks above, must be within 0.5 cm of the average position of the interaction point in the xy plane and within 6 cm in z. Tracks with a large contribution to the χ^2 of the primary vertex fit are removed until the χ^2 probability is greater than 1% (or only two tracks remain). Electromagnetic bumps in the calorimeter not associated with charged tracks, that have an energy greater than 30 MeV in the fiducial volume defined as $(0.41 < \theta < 2.409)$rad and shower shape consistent with photon interaction, are taken as neutral candidates. Charged tracks and neutral candidates are required to have a total energy in the fiducial region greater then 4.5 GeV.

In order to reduce background from continuum events, the normalized second Fox-Wolfram [51] moment of the event (R_2) is required to be less than 0.5. The lth Fox-Wolfram moment H_l is the momentum weighted sum of Legendre polynomial of the lth order computed from the cosine of the angle between all pairs of tracks:

$$H_l = \sum_{ij} \frac{|p_i||p_j|P_l(cos(\theta_{ij}))}{E_{vis}^2} \ , \tag{4.1}$$

where P_l is the Legendre polynomial, i and j run over the tracks, p_{ij} are the tracks momenta, θ_{ij} is the opening angle between the tracks i and j, E_{vis} is the visible energy of the event. Neglecting the particle masses, energy-momentum conservation requires that $H_0 = 1$. For continuum events, $H_1 = 0$, $H_l \sim 1$ for l even and $H_l \sim 0$ for l odd. R_2 is the ratio H_2/H_0.

The ratio R_2 is one of the possible topological variables witch discriminate signal events from continuum $q\bar{q}$ ($q = u, d, s, c$) events on the basis of their characteristic topologies. In a signal event, the primary e^+e^- pair produces a $B\bar{B}$ par via the $\Upsilon(4S)$ resonance. the B mesons have low momentum in the $\Upsilon(4S)$ frame (~ 340 MeV/c), so the decay of each B meson is nearly isotropic. Moreover, in a signal event there is no correlation between the direction of the decay products coming from the two B mesons. On the contrary, in a $q\bar{q}$ continuum event, the event shape has a two-jet structure, then there is a direction which characterize the whole event (the jet axes). Fake B candidates from such events tend to have less isotropic decay shape in the $\Upsilon(4S)$ rest frame, and the direction of the decay products of the two B mesons candidates tend to be correlated, since they lie within the two jets.

The selection efficiency of the multihadron selection for $B\bar{B}$ events is about 95%.

4.1.2   Data sample

For this analysis the data recorded from the $BaBar$ experiment in the period $(1999-2004)$ are used. This data sample corresponds to an integrated luminosity of 208 fb^{-1} recorded at the $\Upsilon(4S)$ resonance, corresponding to $218 \cdot 10^6$ $B\bar{B}$ couples, and 21.6 fb^{-1} collected at a center-of-mass energy 40 MeV below (off-peak data). The off-peak data are useful to study the behavior of the continuum $q\bar{q}$ events. Moreover a large Monte Carlo sample is used for background studies.

4.2 $B^- \to \tilde{D}^0 K^-$ selection

4.2.1   The K_S and D^0 reconstruction

The K_S are reconstructed from pairs of oppositely charged pions. The invariant mass of the two pions is required to be within 9 MeV/c^2 the nominal neutral kaon mass. Since the K_S decay vertex is distant from the beam-spot the tracks momentum is evaluated on the K_S decay vertex.

The D^0 are reconstructed by making all possible combinations between the candidate K_S and two pions of opposite electric charge. The measured position of the D^0 decay vertex and momentum together with their measurement errors, are used to reconstruct a D^0 particle. The invariant mass of the D^0 candidate is required to be within 12 MeV/c^2 its nominal mass. The neutral kaon and the two pions are tested for geometrical compatibility with a single vertex asking that the fit procedure has converged. A kinematic mass constraint is also applied refitting daughters D^0 momenta.

The direction of the K_S can be evaluated from the momentum of the two pions (dir_1) as well as from the direction of the flight distance from the K_S and the D^0 decay vertexes (dir_2). For a genuine candidate these two directions coincide. Defining $\alpha_{K_S} = (dir_1, dir_2)$, a cut on $\cos(\alpha_{K_S}) > 0.99$ is required. This cut has a property of rejecting the not genuine K_S and in particular helps in removing possible contamination from decays of D^0 into four pions.

The distribution of $\cos(\alpha_{K_S})$ for the different Monte Carlo samples is shown in Fig. 4.1.
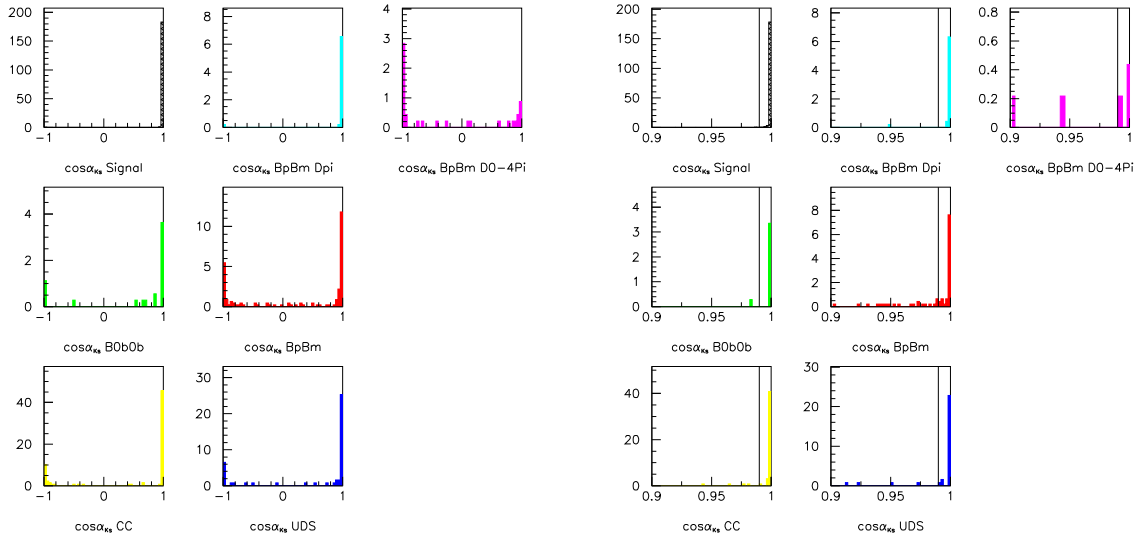
Figure 4.1: *The $cos\alpha_{K_S}$ distribution obtained applying the final selection criteria. (Left plot) Top row - from left to right - signal, $D\pi$ and $D^0 \rightarrow 4\pi$ samples. Middle row - from left to right - $B^0 - \bar{B}^0$ and B^+B^- samples. Bottom row - from left to right - $c\bar{c}$ and uds samples. (Right plot) Same zoomed in the [0.9-1] range.*

4.2.2   The B meson reconstruction

A candidate B^- is obtained combining a D^0 candidate with one of the identified bachelor kaon. The bachelor kaon is required to be identified as a *tight* kaon as described in Sec.2.5.1. To guarantee the quality of this vertex the fit procedure is required to converge.

The main variables used in the B meson selection are the *beam energy-substituted mass* (m_{ES}) and the *energy difference* (ΔE).

The *beam energy-substituted mass* is defined as:

$$m_{ES} = \sqrt{(\sqrt{s}/2)^2 - p_B^{*2}} \,, \tag{4.2}$$

where p^* is the B candidate momentum in the $\Upsilon(4S)$ (CM) rest frame. Since $|p_B^*| \ll \sqrt{s}/2$, the experimental resolution on m_{ES} is dominated by beam energy fluctuations. Then with an excellent approximation, the shapes of the m_{ES} distributions for B meson reconstructed in a final states with charged tracks only are Gaussian and practically identical. Otherwise the presence of neutrals in the final states, in case they are not fully contained in the calorimeter, can introduce tails.

The *energy difference* is defined (making use of energy conservation) as:

$$\Delta E = E_B^* - \sqrt{s}/2 \; , \tag{4.3}$$

where E_B^* is the energy of the B candidate in the $\Upsilon(4S)$ rest frame and $\sqrt{s}$ is the total energy of the e^+e^- system in the CM rest frame. The resolution of this variable is affected by the detector momentum resolution and by the particle identification since a wrong mass assignment implies a shift in ΔE. Signal events are Gaussian distributed in ΔE around zero, continuum and part of the $B\bar{B}$ background have a polynomial distribution and background due to misidentification gives shifted Gaussian peaks. The resolution of this variable depends essentially on the reconstructed B mode and can vary from 20 to 40 MeV.

Since the sources of experimental smearing are uncorrelated (beams energy for m_{ES} and detector momentum resolution for ΔE), the two variables m_{ES} and ΔE are, in practice, uncorrelated.

The overall efficiency on the signal events is equal to 18.0 ± 0.1 % (the efficiency is calculated considering $B^- \to D^0 K^-$ and $D^0 \to K_S \pi^- \pi^+$ and $K_S \to \pi^+ \pi^-$).

The final selection is optimized in order to maximize the statistical significance and to reduce the expected error on γ (using a Toy Monte Carlo technique):

- $|cos\theta_{thr.}| < 0.8$

- tight K-id on bachelor Kaon

- $|M(D^0) - M(PDG)| < 12$ MeV$/c^2$

- $|M(K_S) - M(PDG)| < 9$ MeV$/c^2$

- D^0 and B vertex fit procedure required to converge

- $cos(\alpha_{K_S}) > 0.99$

- $|\Delta E| < 30$ MeV

- $m_{ES} > 5.2$ GeV$/c^2$

The number of events with more than one B candidate is very small (about 1% for the final sample of events with m_{ES} in [5.2, 5.3] GeV$/c^2$ and ΔE in [-30, 30] MeV). The candidate with the D^0 mass closest to the PDG value is retained.
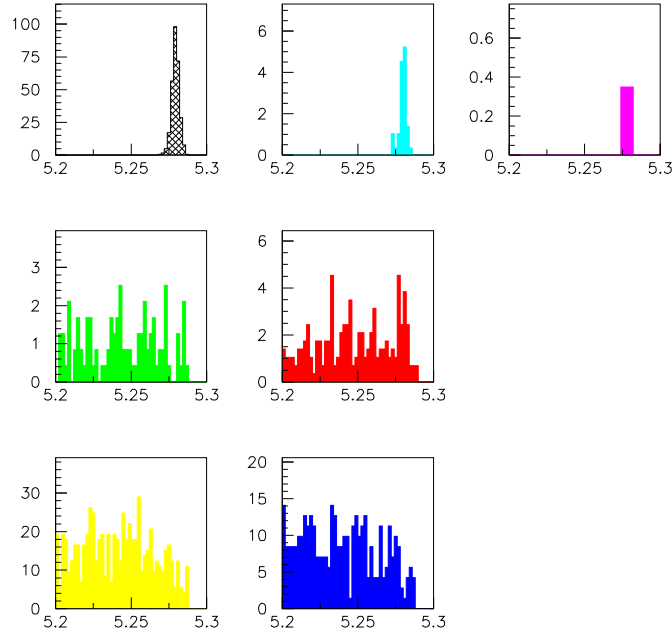
Figure 4.2: *m_{ES} distribution obtained after applying the final selection criteria. Top row - from left to right - signal, $D\pi$ and 4π samples. Middle row - from left to right - $B^0 - \bar{B}^0$ and B^+ samples. Bottom row - from left to right - $c\bar{c}$ and uds samples.*

Fig. 4.2 shows the m_{ES} distribution of the different components after applying the final selection criteria.

4.2.3   Continuum background suppression

The larger component to the background comes from continuum $q\bar{q}$ events. To suppress this background the following topological variables are used.

- $cos(\theta_B^*)$: the polar angle of the reconstructed B meson in the $\Upsilon(4S)$ center of mass system

- the Legendre monomials (L_0 and L_2): $L_j = \sum_i^{tracks} p_i |\cos(\theta_i)|^j$

- $cos(\theta_{thr.})$: the angle between the rest of event thrust axis and the B direction

The thrust axis [52] of an event is defined as the direction which maximizes the sum of the longitudinal momenta of the particles. In a typical background event for a two-body

decay, the decay products of each B candidate lie in one of the two jets, and they are therefore approximately back-to-back. Thus the decay axis of the B candidate is roughly collinear with the thrust axis for the rest of the event. For a true signal event, the B decay axis is uncorrelated with the thrust axis of the rest of the event, which in that case comes from the decay of the other B meson. A cut on $|cos(\theta_{thr})| < 0.8$ is requested.

If there is no correlation between the variables, no information is lost in simply making separate requirements on each one, otherwise to fully exploit the power rejection of the discriminating variables a linear combination of them is needed. In Linear Discriminant Analysis [53], also known as the Fisher method, the discriminating variables which characterize the events, are combined linearly to provide the best separation between the two classes of events:

$$\mathcal{F} = \sum_{i=1}^{N} \alpha_i x_i . \tag{4.4}$$

The discrimination task consists of determining an axis in the R^N space of the discriminating variables such that the two classes are maximally separated. In order to apply this method, one needs to know just the mean values of each variable over the full sample, ($\bar{\mu}$), the means over signal and background separately, ($\bar{\mu}_b$, $\bar{\mu}_s$), and the total variance-covariance matrix, $U_{ij}^{b,s}$, that characterizes the dispersion of the events relative to the center of gravity of their own sample. The distance between the projected points will naturally be maximum along the direction defined by the line between μ_b and μ_s. Then the segment ($\bar{\mu}_b, \bar{\mu}_s$) is the projection axis. The coefficients in Eq. 4.4 could be easily computed from the equation:

$$\alpha_i = \sum_{j=1}^{N} (U^b + U^s)_{ij}^{-1} (\mu_j^b - \mu_j^s) . \tag{4.5}$$

The distribution of the Fisher variable, using the variables described before, for Monte Carlo continuum and signal events is shown in Fig. 4.3.

4.2.4 Data - Monte Carlo comparison

In order to test the goodness of the background composition obtained from Monte Carlo a study of Data - Monte Carlo comparison is performed for the different variables used in the analysis. For all the plots the colored histograms display the various Monte Carlo components and the points the data. Comparisons for the relevant variables used for
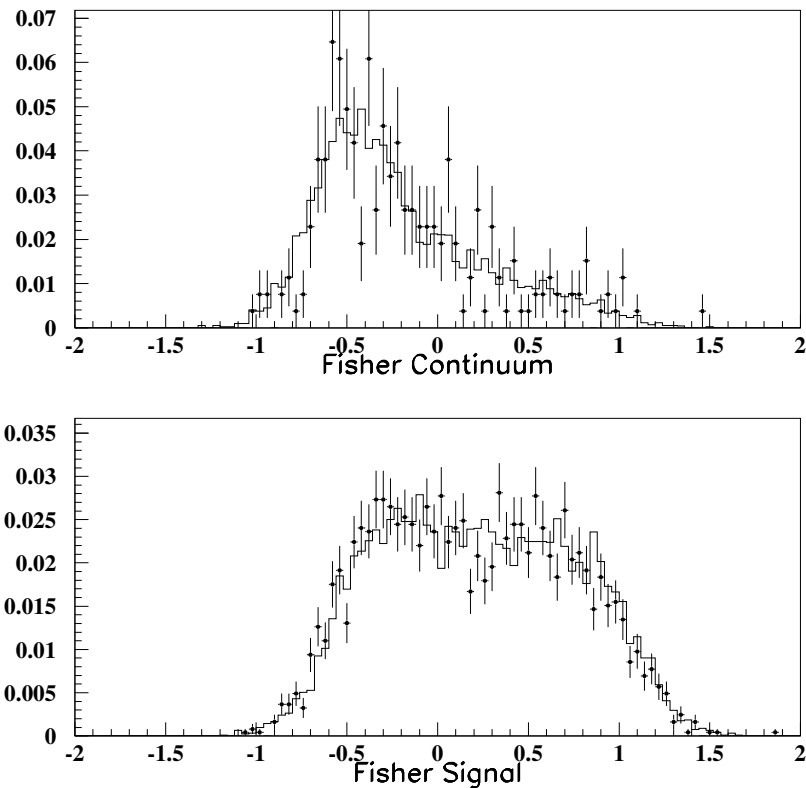
Figure 4.3: *Distribution of the Fisher discriminant variable for continuum (top plot) and $B\bar{B}$ events (bottom plot). The distributions with points are obtained from off-peak data for the top plot and from $D^0\pi$ control sample for the bottom plot. The histograms are obtained from continuum Monte Carlo events for the top plot and signal Monte Carlo events for the bottom plot.*

the selection cuts are shown in Fig. 4.4. The K_S and D^0 invariant mass distributions are plotted with respect to the PDG mass. The data distributions are slightly shifted compared to the Monte Carlo ones, the cuts are far enough so that the efficiency obtained on Monte Carlo will still be correct. These plots are obtained after having applied all the cuts but the one on the displayed variable.

4.2.5   Sample composition

To fit the m_{ES} distribution, it is used a Gaussian for the signal and an empirical function suggested by the ARGUS collaboration [54] for background. The ARGUS function is
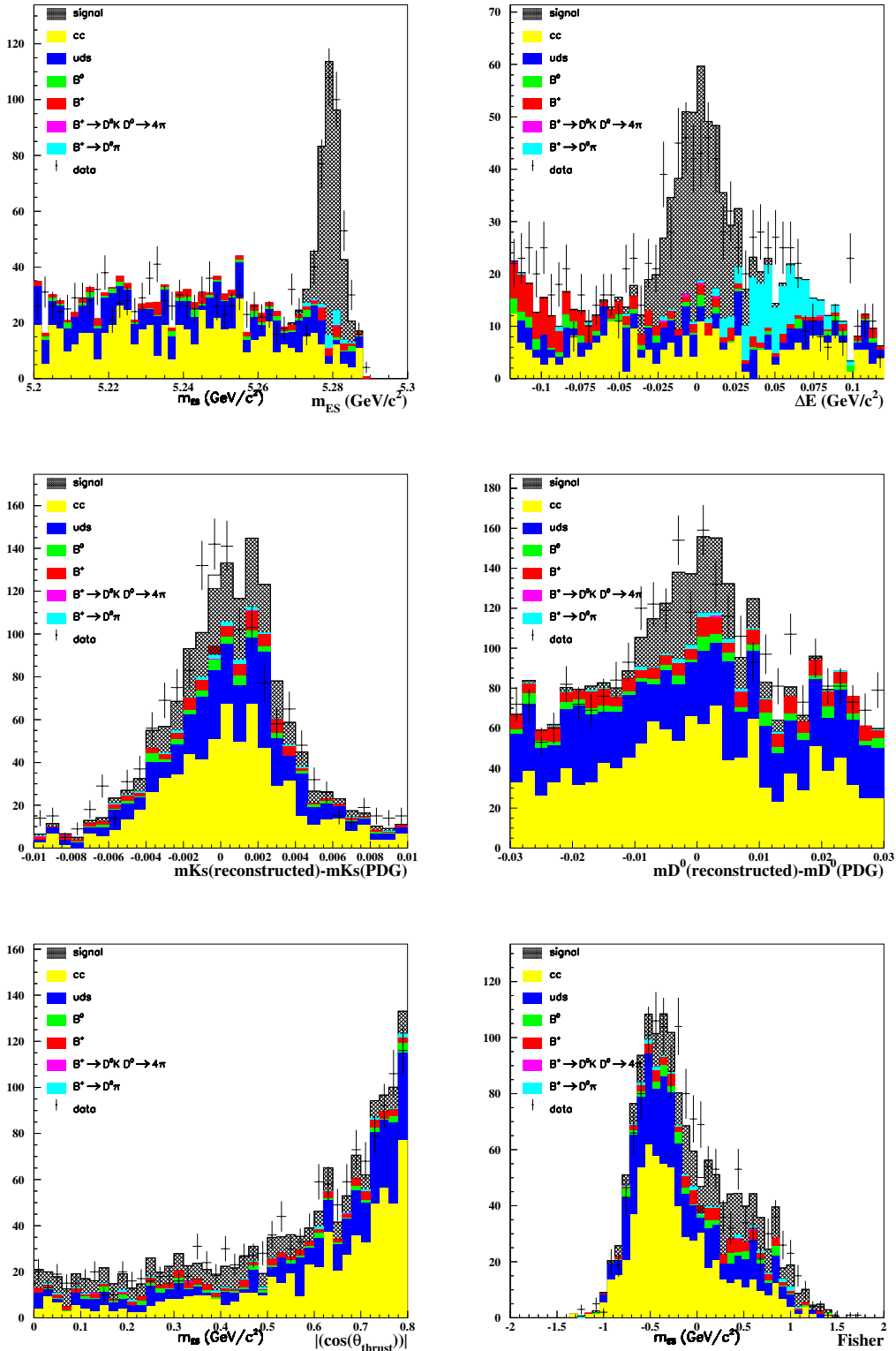
Figure 4.4: *Data Monte Carlo comparison for the relevant variables used for the selection cuts: m_{ES} and ΔE (first row), K_S e D^0 invariant mass (second row), $|cos(\theta_{thr.})|$ and the Fisher (third row). The distributions are obtained after having applied all the other cuts.*

defined as:

$$\frac{dN}{dm_{ES}} = N \cdot m_{es} \cdot \sqrt{1 - x^2} \cdot \exp\left(-\xi \cdot (1 - x^2)\right) , \qquad (4.6)$$

where $x = m_{es}/m_{\max}$ and the parameter ξ is determined from the fit. The $m_{\max}$, that represent the endpoint of the ARGUS distribution, is fixed in the fit to m_{ES}, since it depends only on the beam energy.

From this fit the parameter $f_s = \frac{N(DK)+N(D\pi)+N(4\pi)}{N_{\mathrm{cand}}}$ is extracted in the m_{ES} signal region (>5.272 GeV/c^2, see Tab. 4.1).

It is important to notice that the contribution from the "peaking background" (the background that presents a peak in the m_{ES} signal region) is very small and is essentially due to the $B^- \to D^0\pi^-$ events. The fraction of this background can be obtained from simple counting of Monte Carlo events or by fitting the ΔE distribution (see Tab. 4.1).

Fig. 4.5 shows the ΔE distribution of the different components with the final selection criteria in the m_{ES} signal region ($m_{ES} >5.272$ GeV/c^2). In order to to exclude the contribution from the $B^- \to \tilde{D}^*K^-$ events only the region between [-0.100,0.120] GeV is considered in the fit. The events from DK and $D\pi$ are parameterized with a Gaussian distribution. For the DK events the Gaussian is centered on zero and its width is $\sigma(DK)(MC) = (14.6 \pm 0.2)$ MeV.

The Gaussian distribution for the $D\pi$ events is centered on $< \mu > (D\pi)(MC) = (50.2 \pm 1.2)$ MeV with width $\sigma(DK)(MC) = (18.7 \pm 1.0)$ MeV. The parameters from the two Gaussian distributions are related. In fact the Gaussian describing the ΔE distribution of the $D\pi$ events is shifted by about 50 MeV and its resolution is the result of the convolution of the bachelor track momentum resolution and the ΔE resolution of the DK events:

$$\begin{aligned} N &= N(DK)e^{-(\Delta E-\mu)/2\ \sigma^2(DK)} + N(D\pi)e^{-(\Delta E-(\mu+0.05))/2\ \sigma^2(D\pi)} + P_1(y) , \quad (4.7)\\ &\sigma^2(D\pi) = \sigma^2(DK) + K , \\ &K = \sqrt{\sigma^2(D\pi)(MC) - \sigma^2(DK)(MC)} = 0.010 . \end{aligned}$$

The global fit on the data and Monte Carlo are performed using Eq. 4.7 where the width of the Gaussian distribution $\sigma(DK)$ is obtained from the $D\pi$ control sample (see section 4.2.7). The results of the fits are shown in Fig. 4.5 and in Tab. 4.1.

The D^0 Dalitz distribution of $B^- \to D^0\pi^-$ is the same of $B^- \to D^0K^-$ events without the opposite D^0 flavor admixture. Another possible source of peaking background, $D^0 \to 4\pi$ has a negligible contribution ($< 1\%$) after the cut on $\cos(\alpha_{K_S})$.
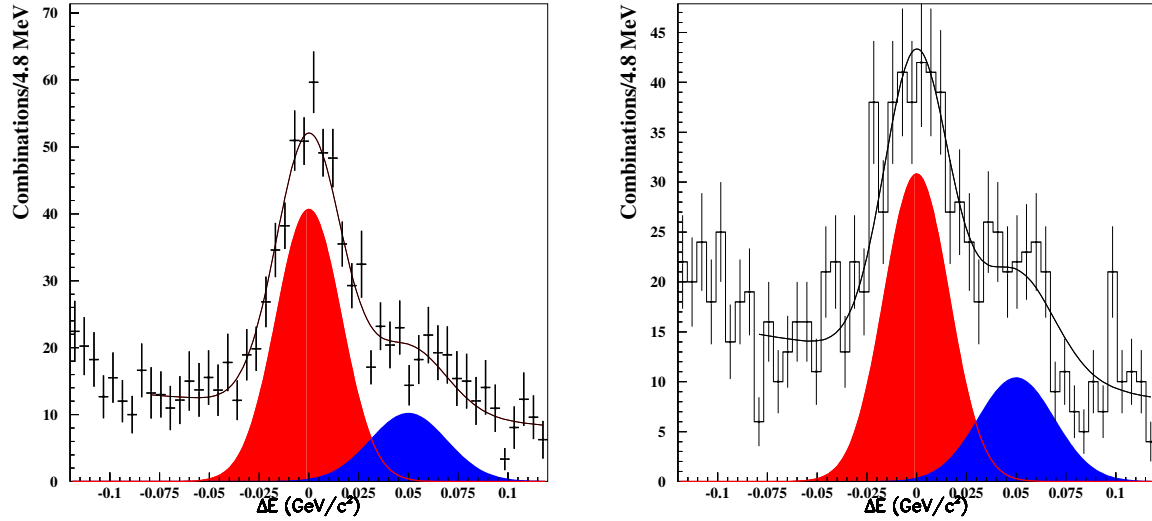
Figure 4.5: *The plots on right (left) show the ΔE distribution as obtained on the data (Monte Carlo) with the fit superimposed. The two Gaussian distributions for the DK and the $D\pi$ events are also shown.*
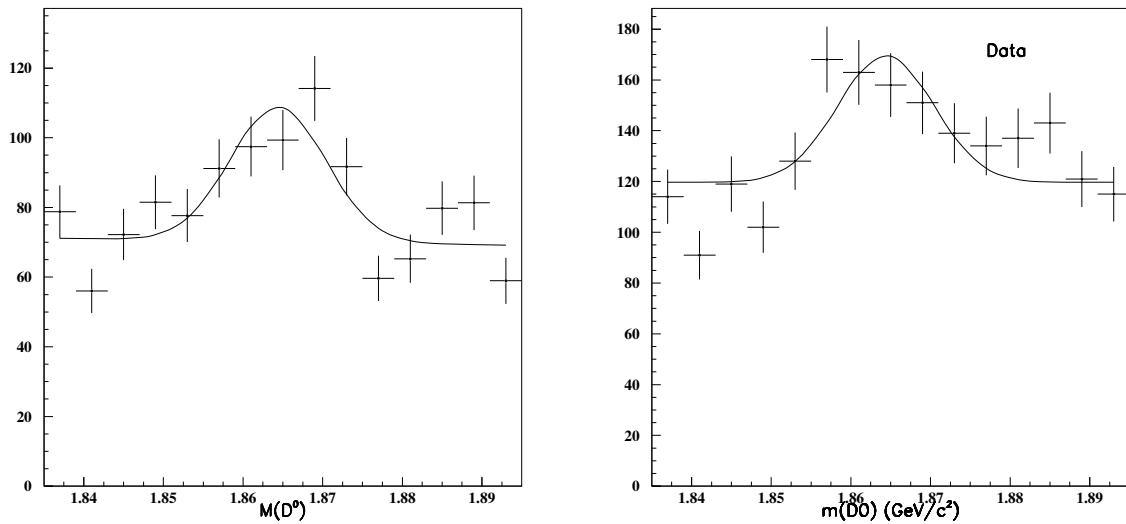

Figure 4.6: *The plots on right (left) show the D^0 invariant mass distribution as obtained on the data (simulation) for events satisfying $m_{ES} < 5.27$ GeV/c^2 and having removed the cut on the D^0 mass. The result of the fit is superimposed.*

Parameter	Value from Data	Value from Monte Carlo
f_s ($m_{ES} > 5.272$ GeV/c^2)	0.672 ± 0.049	0.669 ± 0.065
f_s ($m_{ES} > 5.2$ GeV/c^2)	0.219 ± 0.016	0.221 ± 0.023
$f_{D\pi}$	0.059 ± 0.012	0.028 ± 0.012
f_{cont} ($m_{ES} > 5.272$ GeV/c^2)	-	0.854 ± 0.040
f_{cont} ($m_{ES} > 5.2$ GeV/c^2)	-	0.905 ± 0.012
$R_{Cont.}$	0.221 ± 0.042	0.27 ± 0.06
R^{RS}	-	0.208 ± 0.033

Table 4.1: *Values for parameters used in the likelihood. Whenever possible the values obtained from Data are used. Most of the parameters are evaluated directly with the likelihood fit (see. Sec. 5.1).*

The fraction of combinatoric background events is obtained from a fit in all the m_{ES} region.

To properly parameterize the Dalitz distributions of the background it is important to evaluate the possible presence of true D^0 (D^0 decaying in $K_S\pi^-\pi^+$) and the charge correlation with the bachelor kaon. The presence of true D^0, in fact, combined with a randomly flavor-tagged kaon could be a potentially important background because for half of the cases the kaon is of opposite sign and these events can be taken as $B^+ \rightarrow \bar{D}^0 K^+$ events. For this reason the background is separated in continuum background and background from $B\bar{B}$ events, and in each category the number of true D^0 is evaluated. The relative fraction, normalized to the total non peaking background, of the continuum events is obtained by fitting the m_{ES} distribution from the simulated data. The fraction of true D^0 coming from D^* decays is expected to be small due to the ΔE cut. In the simulation events the fraction of this events is $< 2\%$ then its contribution can be neglected. A sizable contribution, instead, is found in the continuum events, totally coming from the $c\bar{c}$ events.

The total fraction of the true D^0 in the combinatorial background can be obtained on the data and compared with the one from the Monte Carlo. For this purpose the events satisfying $m_{ES} < 5.272$ GeV/c^2 are considered, having removed the cut on the D^0 mass. Fig. 4.6 shows the D^0 invariant mass for data and Monte Carlo events. For simulated events the plot are obtained using the corrected relative integrated luminosities processed for the uds, $c\bar{c}$ and the $B\bar{B}$ events. The fit to the D^0 invariant mass is performed by fixing the mean and the width of the D^0 to 1864 MeV/c^2 and 6 MeV/c^2 as found on the

$c\bar{c}$ simulation. The values are corrected considering that the only true D^0 come from the $c\bar{c}$, and are shown if Tab. 4.1 ($R_{Cont.}$). Another important parameter is the fraction of events with a true D^0 associated with a negative charged kaon (R^{RS}). This fraction is obtained from simulation because there is not enough off-peak data.

In case of a true D^0 the Dalitz distribution can be taken from the one of the D^0 or $\bar{D}^0$ depending of the charge correlation with the Kaon and according to this fraction. The summary of the values and errors obtained for the different parameters is given in Tab. 4.1.

4.2.6 Efficiency over the Dalitz plot and related systematics

The efficiency on the signal events over the Dalitz plot ($m^2(K_s\pi^+) \equiv x$ *vs* $m^2(K_s\pi^-) \equiv y$) is evaluated using a signal Monte Carlo sample with a flat Dalitz distribution. The Dalitz plot is binned and the efficiency is fitted with a symmetric third-order polynomial function:

$$eff(x,y) = a_0[1 + a_1(x+y) + a_2(x^2 + y^2 + xy) + a_3(x^3 + y^3 + x^2y + xy^2)] \ . \qquad (4.8)$$

It is checked that the shape of the efficiency correction, in Fig. 4.7, does not depend from the Fisher and m_{ES} discriminating variables. The coefficients for the three subsamples, $B^- \to D^0K^-$, $B^- \to (D^0\pi^0)K^-$ and $B^- \to (D^0\gamma)K^-$, are consistent within statistical errors, therefore for the final fit the parameterization by combining all modes is taken.

For the systematics evaluation due to tracking and K_S reconstruction, the efficiency over the Dalitz plot has to be weighted according to the tracking efficiency and K_S reconstruction.

4.2.7 The use of the $B^- \to D^0\pi^-$ events

The $B^- \to D^0\pi^-$ events can be used as a control sample to obtain some parameters for the analysis. All the $B^- \to D^0\pi^-$ selection criteria are identical to those applied for the $B^- \to \tilde{D}^0K^-$ analysis except that the events are selected in the ΔE region in the range [+0.020-0.080] GeV (see Fig. 4.5). In order to have completely independent samples the bachelor pion is required to be not identified as a loose kaon (see Sec. 2.5.1).

The overall background fraction is smaller than in the DK sample. Nevertheless the $B\overline{B}$ background shows more important and complicated peaking structure coming from many different components (charmless events, $\ell^+\ell^-$ K_s π events .....) with respect to DK case. Considering that r_B, thus the fraction of $b \to u$-type decays, for this sample is much
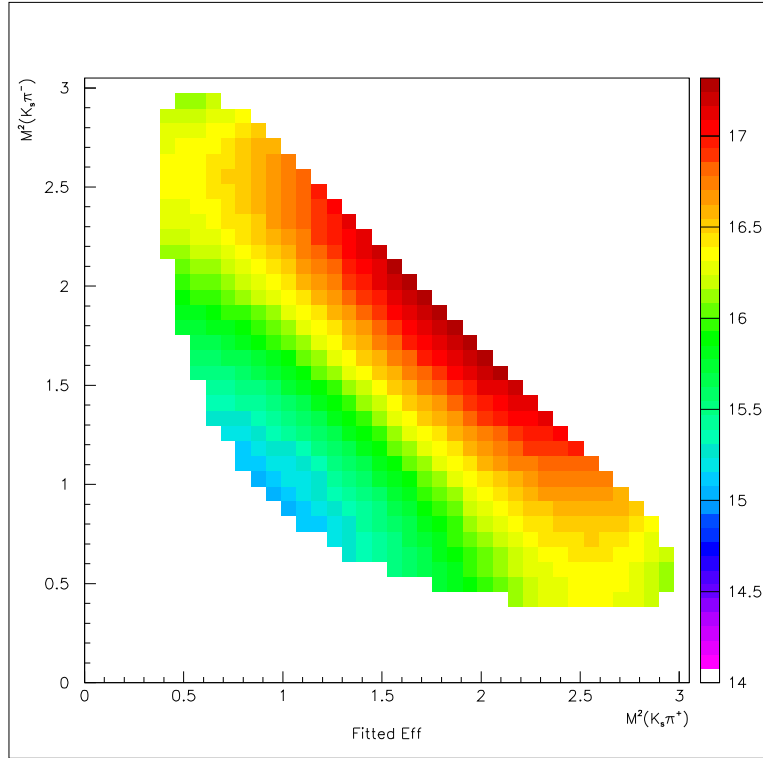
Figure 4.7:   *Fitted efficiency over the Dalitz $(K_s\pi^+)$ vs $(K_s\pi^-)$ for the Monte Carlo sample. The color code indicates the value (in percent) of the fitted efficiency, note that the color code is only meaningful inside the kinematically allowed Dalitz region. This is taken from high statistics $B^- \to D^{*0}K^-$ signal Monte Carlo.*

smaller that for $B^- \to \tilde{D}^0 K^-$ sample, it seems to be difficult to consider the use of this sample for fitting the angle γ, but, being that in the signal region ($m_{ES} > 5.272$) the $B\bar{B}$ events amounts to about 95% of the total number of the events, this sample can be used to obtain the Fisher parameterization of the $B\bar{B}$ events. The Fisher parameterization of the continuum events is obtained using off-peak data sample in the signal region for m_{ES} distribution.

For continuum events the distribution of the Fisher variable $\mathcal{F}$ is fitted with a double Gaussian distribution:

$$f \times e^{-\frac{(\mathcal{F}-\mu_1)^2}{2\sigma_1^2}} + (1-f) \times e^{-\frac{(\mathcal{F}-\mu_2)^2}{2\sigma_2^2}} \ . \tag{4.9}$$

Since on peak data in the signal box contains 94% of $B\bar{B}$ events, the distribution is fitted using a double Gaussian for the $B\bar{B}$ events and for the residual 6% of background events fixing the parameters of a double Gaussian distribution as obtained from the fit on the continuum events. The double peak structure is due to the very important weight of the

$|cos\theta_{thr.}|$ variable in the Fisher variable. This effect can also be seen in Fig. 4.9 where the Fisher variable with respect to $|\cos\theta_{thr.}|$ is shown.

4.2.8 Background Dalitz shape

In order to perform the CP fit (described in Sec. 5) the Dalitz distributions for the various backgrounds are parameterized. the Dalitz shape for continuum $q\bar{q}$ is parameterized from off-resonance data events selecting the D^0 mass sidebands in order to exclude the real D^0 ($Mass(D^0) < 1.85$ GeV/c^2 or $Mass(D^0) > 1.88$GeV/c^2 is requested). For generic $B\bar{B}$ Monte Carlo events with no real D^0 is used. The selection cuts are identical to those used for the $B^- \to D^0K^-$, except the ΔE cut which is relaxed to have larger statistics. Both the distributions ($q\bar{q}$ and $B\bar{B}$) are fitted by a symmetric second order polynomial function:

$$a_0 + a_1(x + y) + a_2(x^2 + y^2 + xy) , \qquad (4.10)$$

with $m^2(K_S\pi^-) \equiv x$ and $m^2(K_S\pi^+) \equiv y$.

The fit result for $q\bar{q}$ is shown in Fig. 4.10. For the $B\bar{B}$ Monte Carlo the true D^0 candidates are removed and the $m^2(K_S, \pi^{\pm})$ versus $m^2(K_S, \pi^{\mp})$ distribution is made. The fit result is shown in Fig. 4.11.

4.3 $B^- \to \tilde{D}^{*0}K^-$ selection

4.3.1 Events selection

The D^0 and the K_S are reconstructed using the same selection criteria used for the $B^- \to D^0K^-$ selection. The D^{*0} is reconstructed in the two channels: $D^{*0} \to D^0\pi^0$ and $D^{*0} \to D^0\gamma$. The γ candidates for $D^{*0} \to D^0\gamma$ are requested to have a maximum lateral moment (LAT, see Sec. 2.6.1) of 0.8. The π^0 candidates are reconstructed combining couples of photon with a energy greater than 30 MeV. The selected π^0 are requested to have a momentum in the interval [70,450] MeV/c and a mass in the interval [115,150] MeV/c^2. To improve the momentum resolution, the π^0 candidates are kinematically fit with their mass constrained to the nominal π^0 mass. Before combining a D^0 candidate with a soft π^0 or a photon to form a D^{*0}, a mass-constrained fit is applied to the D^0. The resolution of the $D^{*0} - D^0$ mass difference (Δm) is ~ 1.2 MeV/c^2 for $D^{*0} \to D^0\pi^0$ and ~ 5.0 MeV/c^2 for $D^{*0} \to D^0\gamma$. Fig. 4.12 shows the Δm distributions for D^{*0} from Monte Carlo signal events.

P1	0.6869 ±	0.8235E-01
P2	-0.4240 ±	0.3544E-01
P3	0.2612 ±	0.2389E-01
P4	0.3012 ±	0.1310
P5	0.4476 ±	0.5576E-01

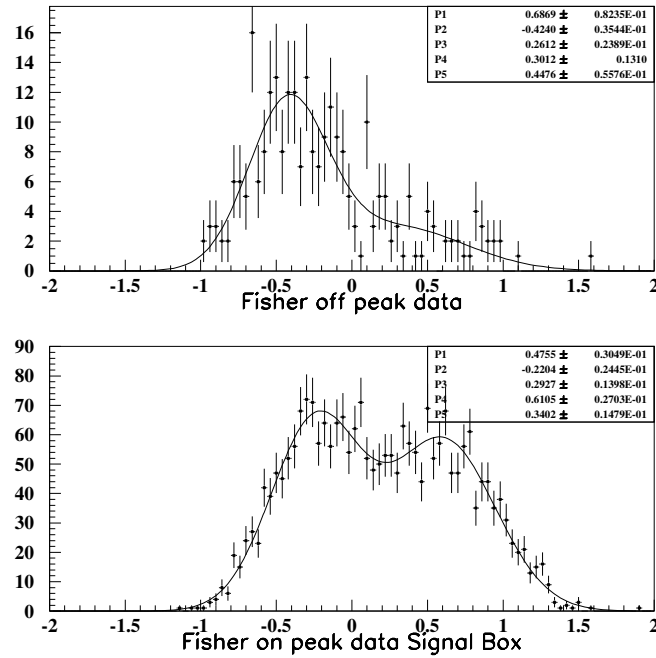| P1 | 0.4755 ± | 0.3049E-01 |
P2	-0.2204 ±	0.2445E-01
P3	0.2927 ±	0.1398E-01
P4	0.6105 ±	0.2703E-01
P5	0.3402 ±	0.1479E-01

Figure 4.8: *Fisher discriminant variable obtained from the $B^- \to D^0\pi^-$ analysis for $B\bar{B}$ events (top distribution) and for continuum events (bottom distribution).*
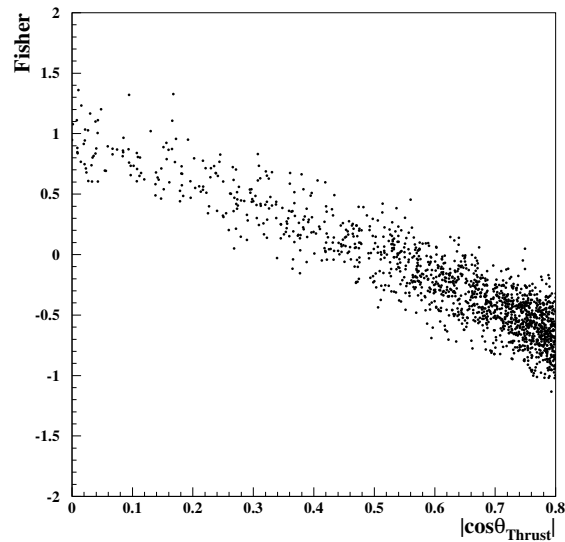

Figure 4.9: *Fisher discriminant variable versus $|\cos\theta_{thr.}|$ on continuum Monte Carlo events. The correlation is clearly visible.*

Figure 4.10: *Distributions of $m^2(K_S, \pi^{\pm})$ for $B^{\pm}$ candidates (top plot) and $m^2(K_S, \pi^{\mp})$ for $B^{\pm}$ candidates (bottom plot). The points represent the $q\bar{q}$ off-resonance data events, the histogram the result of the second order polynomial fit and the dashed histogram the projection of an uniform distribution.*
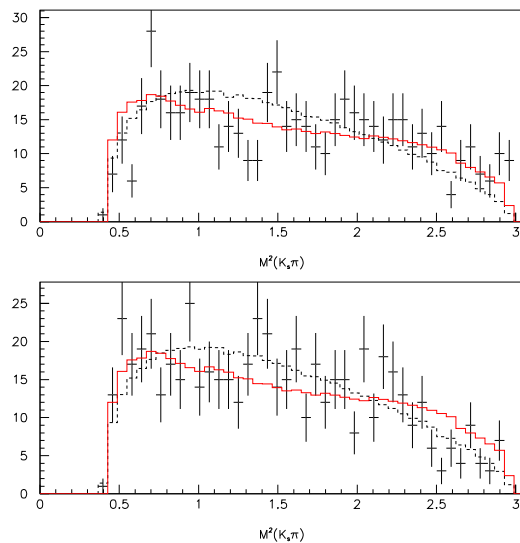

Figure 4.11: *Distributions of $m^2(K_S, \pi^{\pm})$ for $B^{\pm}$ candidates (top plot) and $m^2(K_S, \pi^{\mp})$ for $B^{\pm}$ candidates (bottom plot). The points represent the $B\bar{B}$ Monte Carlo events, the histogram the result of the second order polynomial fit and the dashed histogram the projection of an uniform distribution.*
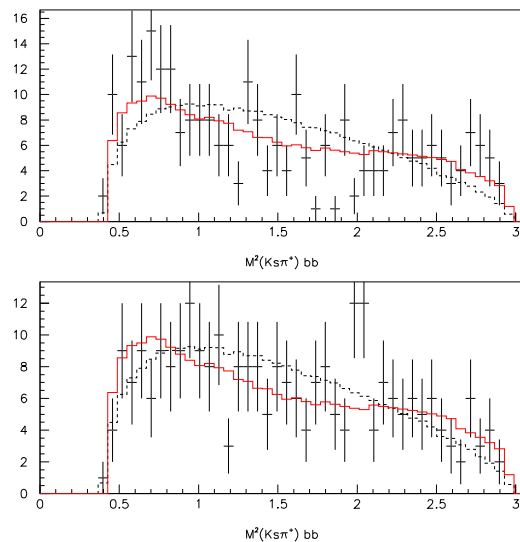
The charged B is reconstructed adding the kaon to the D^{*0} candidate and a kinematic and geometric fit is performed to the whole decay. In this fit charged B and D^0 decay vertexes are reconstructed. In order to improve the m_{ES} and ΔE resolution in the kinematic fit the D^{*0} and D^0 masses are fixed to their nominal value. The resolutions, measured on MC signal events, are 2.6 MeV/c^2 and 16.7 MeV for m_{ES} and ΔE, respectively. As in the $B^- \rightarrow \tilde{D}^0 K^-$ selection, the cut $|\cos\theta_{thr.}| < 0.8$ is required to suppress the background from continuum production of light quarks. If multiple B candidates are found in the same event after all the selection criteria are applied, the candidate with the smallest $\chi^2 = \chi^2(\Delta m, m_{\pi^0})$ for $D^0\pi^0$ and $\chi^2 = \chi^2(\Delta m)$ for $D^0\gamma$ is chosen. The fraction of events with multiple B candidates is 9% for $D^0\pi^0$ and 3% for $D^0\gamma$. After the best choice selection the contamination of background events coming from true $D^0\gamma$ signal events into the $D^0\pi^0$ signal sample and viceversa is completely negligible. The best choice algorithm has an efficiency on signal Monte Carlo events of $(75\pm3.0)\%$ for $D^0\pi^0$ and $(63\pm7)\%$ for $D^0\gamma$. The correlation among the variables used in the χ^2 calculation and the fitted parameters, $m^2(K_s\pi^+)$ and $m^2(K_s\pi^-)$, is evaluated on signal Monte Carlo and it is negligible.

The final selection criteria, optimized in order to maximize the statistical significance, are:

- $|cos\theta_{thr.}| < 0.8$

- tight K-id on bachelor Kaon

- $|M(D^0) - M(PDG)| < 12$ MeV/c^2

- $|M(K_S) - M(PDG)| < 9$ MeV/c^2

- $|\Delta m - \Delta m(PDG)| < 2.5$ MeV/c^2 in the $D^0\pi^0$ and < 10 MeV/c^2 in the $D^0\gamma$

- $cos(\alpha_{K_S}) > 0.99$

- $|\Delta E| < 30$ MeV

- $M_{ES} > 5.2$ GeV/c^2

The overall efficiency is 4.3% for the $D^0\pi^0$ and 8.1% for the $D^0\gamma$ decay mode.
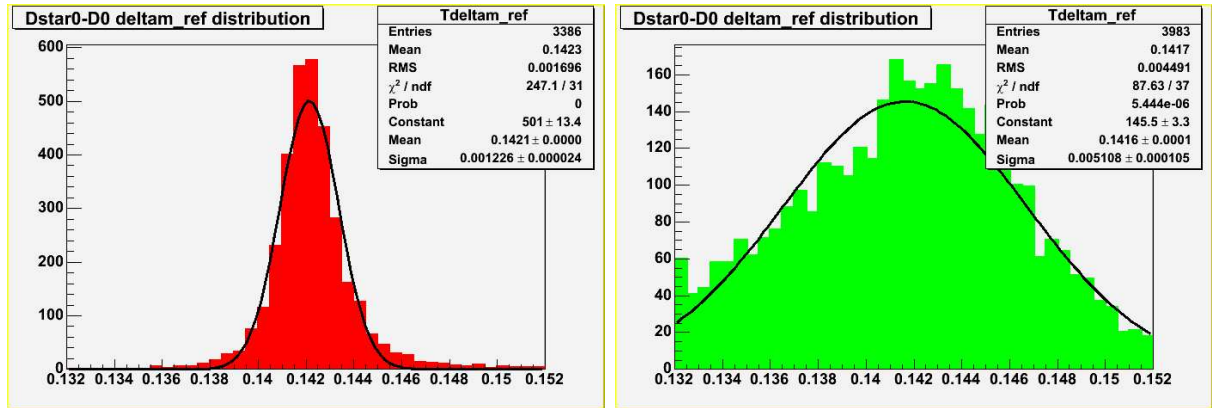
Figure 4.12: *The Δm mass difference distribution for signal MC events. The distributions are fitted with a single Gaussian in order to estimate the width and the mean value. For the $D^0 \gamma$ the Gaussian fit gives a rough estimation of the mean and of the width of the distribution.* **Left plot:** *the Δm width of $D^0 \pi^0$ is around* 1.2 *MeV/c^2.* **Right plot:** *the Δm width of $D^0 \gamma$ is around* 5.1 *MeV/c^2.*

4.3.2   Sample composition

Like the $B^- \to \tilde{D}^0 K^-$ selection, a fit to the m_{ES} distribution is performed after applying the selection criteria in order to obtain an estimate of the event yield $f_s = \frac{N(D*K)+N(D*\pi)}{N_{\mathrm{cand}}}$ and Data-Monte Carlo comparison. Fig. 4.13 shows the data m_{ES} distribution with the fit superimposed.

The background can be divided in two main categories: continuum background and $B\bar{B}$ background; the continuum is the dominant background. The $B\bar{B}$ background is composed by a peaking (in m_{ES}) component and a non-peaking component. The non-peaking component can be parameterized as the continuum background and then is easy to reduce. The peaking background, instead, is more difficult to reduce and is essentially constituted from $D^{*0}\pi$ events that can be considerably suppressed applying the tight kaon-id requirement on the bachelor track and the tight $|\Delta E| < 30$ MeV cut. The Fraction of $B^- \to D^{*0}\pi^-$ ($f(D\pi) = \frac{N(D\pi)}{N(DK)+N(D\pi)}$) events can be estimate simply counting the number of events in Monte Carlo simulation or directly from the Data, evaluating the $D^{*0}\pi$ contribution fitting the ΔE distribution. The $D^{*0}\pi$ signal is parameterized with a Gaussian with a mean of (50.8 ± 0.2) MeV and a width of (21.0 ± 0.2) MeV, both fixed to the Monte Carlo value. The fraction of $D^{*0}\pi$ events evaluated on data in the range ΔE [-30,30] MeV is given in Tabs. 4.2 and 4.3 and the fit result is shown in Fig. 4.14.

Another peaking background component comes from $D^0 \to 4\pi$ decay but it has a
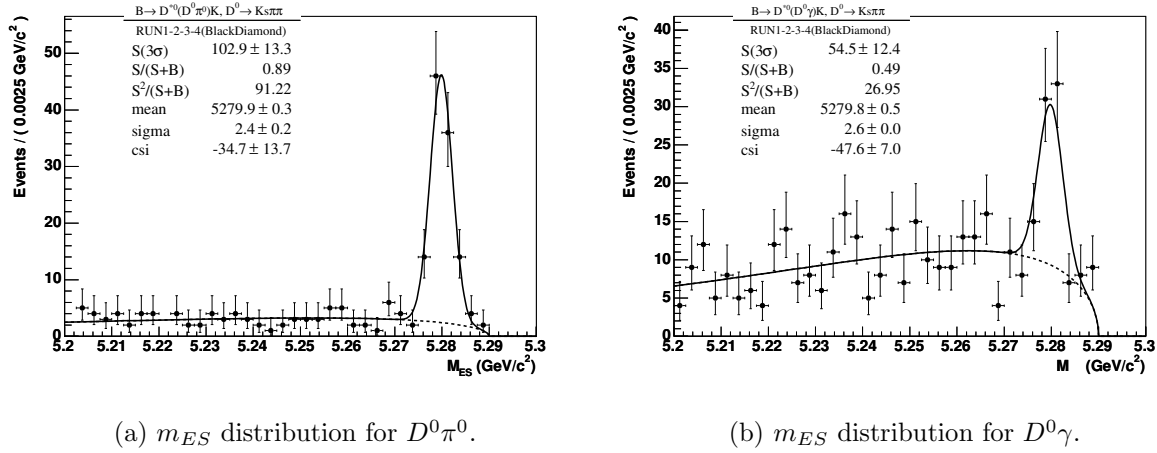
(a) m_{ES} distribution for $D^0\pi^0$.

(b) m_{ES} distribution for $D^0\gamma$.

Figure 4.13: *The m_{ES} distribution obtained after applying the final selection criteria on data. Data are represented by point with error bars, the fit PDF is superimposed.*

negligible contribution after the cut on $cos(\alpha_{K_S})$.

The background composition is similar in the $D^{*0} \to D^0\pi^0$ and the $D^{*0} \to D^0\gamma$, but the amount of background is larger in the $D^{*0} \to D^0\gamma$ channel (see Fig. 4.13).

Like the $B^- \to \tilde{D}^0 K^-$ selection, the background is divided in continuum events and $B\bar{B}$ events as the two contribution in principle have different impact on the γ measurement. The $B\bar{B}$ events have similar shape variables to the signal events and they can have a higher weight in the likelihood fit with respect to the $c\bar{c}$ events; the $B\bar{B}$ events have also different fraction of true D^0 and charge correlation with the bachelor charged track. The relative fraction of continuum events ($f_{cont.}$) is evaluated on Monte Carlo simulated events. In the final CP fit this fraction will be directly estimated from the data sample exploiting the Fisher variable information as discussed in Sec. 5).

As for the $B^- \to \tilde{D}^0 K^-$ case, to properly parameterize the Dalitz distributions of the background is important to evaluate the possible presence of true D^0 (D^0 decaying in $K_S\pi^-\pi^+$) in both $c\bar{c}$ and $B\bar{B}$ background events ($R_{B\bar{B}}$ and $R_{c\bar{c}}$). The fraction of true D^0 can be estimated from Monte Carlo simulation by simply counting the number of true D^0 and false D^0 of each background sample after having applied all the cuts. The fraction of true D^0 for the overall background, can be estimated also in data with a D^0 mass fit, selecting events satisfying $m_{ES} < 5.272$ MeV/c^2 and having removed the cut on the D^0 mass. Fig. 4.15 shows the D^0 invariant mass for data. In the fit to the D^0 invariant mass

(a) ΔE distribution for $D^0\pi^0$.

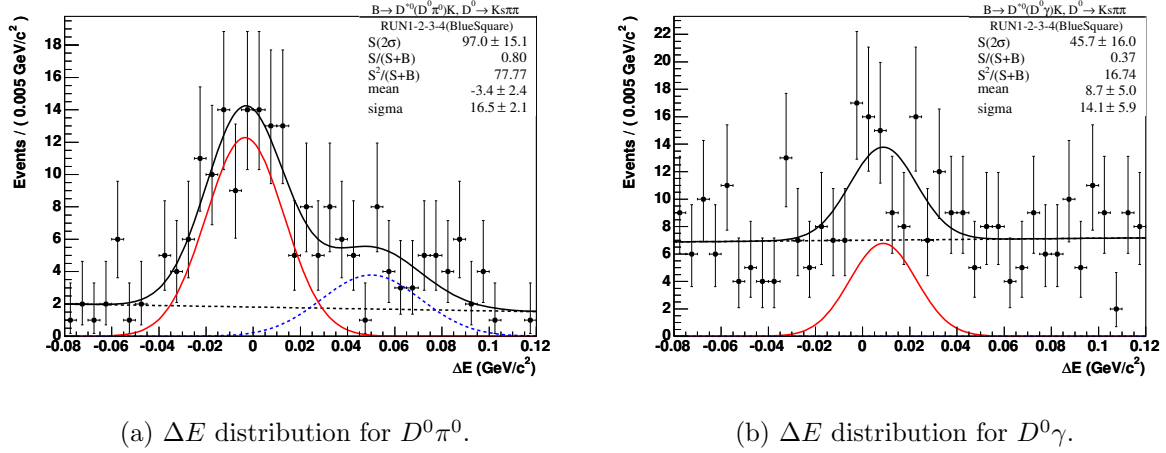(b) ΔE distribution for $D^0\gamma$.

Figure 4.14: *The ΔE distribution obtained after applying the final selection criteria on data. Data are represented by point with error bars, the fit PDF is superimposed. The signal PDF is shown in red, while the PDF contribution for the $D^{*0}\pi$ sample is reported in blue.*

the mean and the width of the D^0 are fixed to 1864 MeV/c^2 and 7 MeV/c^2 as found on the Monte Carlo simulation.

Another important parameter is the fraction of events with a true D^0 associated with a negative charged kaon. This fraction is obtained from Monte Carlo $c\bar{c}$ ($R_{c\bar{c}}^{RS}$) and $B\bar{B}$ ($R_{B\bar{B}}^{RS}$) events and is given in Tabs. 4.2 and 4.3.

Even if the uncertainty on this fraction is large, the level of this background is low and the systematic error is expected to be small. This is confirmed by ToyMC studies.

The summary of the values and errors obtained for the different parameters for the CP Fit is given in Tab. 4.2 for $D^0\pi^0$ and in Tab. 4.3 for $D^0\gamma$.

4.3.3 Data - Monte Carlo comparison

The Data - Monte Carlo comparison is performed for the relevant variables used in the event selection. The agreement is pretty nice after the cut $|cos(\theta_{thr.}) < 0.8|$ is applied. For all the plots the colored histograms display the various Monte Carlo components and the points the data. Comparisons for K_S and D^0 mass, $cos(\theta_{thr.})$, Δm, m_{ES}, ΔE are shown in Fig. 4.16 for $D^0\pi^0$ and in Fig. 4.17 for $D^0\gamma$.

Parameter	Value from Data	Value from Monte Carlo
f_s ($m_{ES} > 5.272$ GeV/c^2)	0.92 ± 0.04	0.91 ± 0.05
f_s ($m_{ES} > 5.2$ GeV/c^2)	0.53 ± 0.08	0.50 ± 0.07
$f_{D\pi}$	0.06 ± 0.07	0.05 ± 0.05
f_{cont} ($m_{ES} > 5.272$ GeV/c^2)	-	0.64 ± 0.13
f_{cont} ($m_{ES} > 5.2$ GeV/c^2)	-	0.88 ± 0.03
$R_{c\bar{c}}$	-	0.27 ± 0.08
$R_{B\bar{B}}$	-	0.11 ± 0.06
$R_{c\bar{c}}^{RS}$	-	0.23 ± 0.11
$R_{B\bar{B}}^{RS}$	-	1

Table 4.2: *Values for parameters for $D^0\pi^0$ used in the likelihood. Whenever possible the values obtained from Data are used. Most of the parameters are evaluated directly with the likelihood fit (see. Sec. 5.1).*

Parameter	Value from Data	Value from Monte Carlo
f_s ($m_{ES} > 5.272$ GeV/c^2)	0.47 ± 0.10	0.62 ± 0.08
f_s ($m_{ES} > 5.2$ GeV/c^2)	0.22 ± 0.04	0.16 ± 0.04
$f_{D\pi}$	0.00	0.01 ± 0.09
f_{cont} ($m_{ES} > 5.272$ GeV/c^2)	-	0.66 ± 0.06
f_{cont} ($m_{ES} > 5.2$ GeV/c^2)	-	0.86 ± 0.01
$R_{c\bar{c}}$	-	0.13 ± 0.02
$R_{B\bar{B}}$	-	0.16 ± 0.03
$R_{c\bar{c}}^{RS}$	-	0.16 ± 0.06
$R_{B\bar{B}}^{RS}$	-	1

Table 4.3: *Values for parameters for $D^0\gamma$ used in the likelihood. Whenever possible the values obtained from Data are used. Most of the parameters are evaluated directly with the likelihood fit (see. Sec. 5.1).*
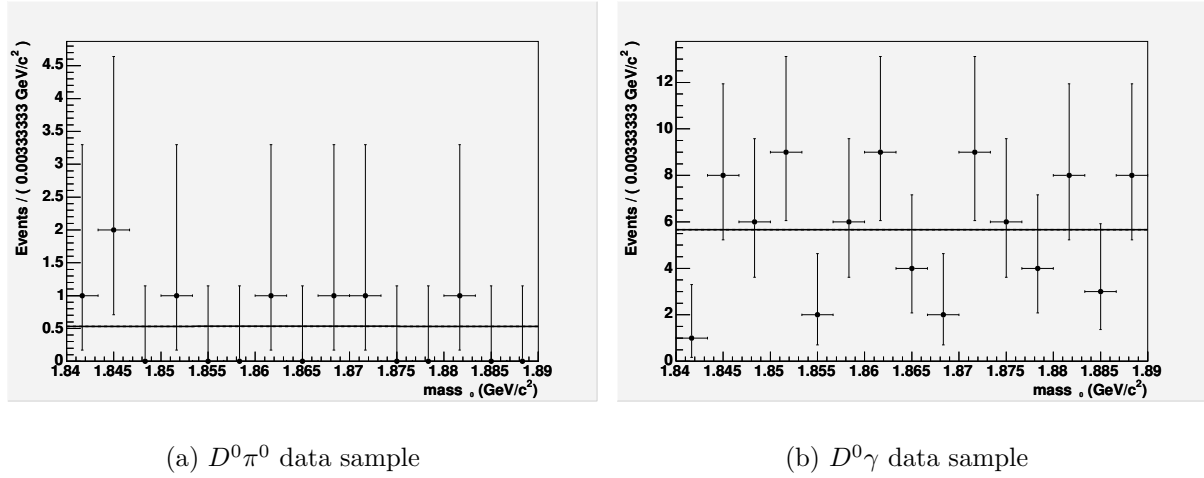
(a) $D^0\pi^0$ data sample   (b) $D^0\gamma$ data sample

Figure 4.15: D^0 *invariant mass distribution as obtained on the data satisfying* $m_{ES} <$ 5.272 GeV/c^2 *and having removed the cut on the* D^0 *mass for* $D^0\pi^0$ *and* $D^0\gamma$*. The result of the fit is superimposed.*

4.3.4 The use of the $B^- \to D^{*0}\pi^-$ events

The $B^- \to D^{*0}\pi^-$ control sample is very useful for resolution studies and for the parameterization of the shapes of the relevant distributions as Fisher discriminant, ΔE and m_{ES}. The selection criteria are the same as for the $B^- \to \tilde{D}^{*0}K^-$ except the request for the bachelor track not to be identified as a notAPion as described in Sec 2.5.1. The $|\Delta E| < 30$ MeV cut is applied using the pion hypothesis for the mass of the bachelor track. The background composition is quite different with respect to the $B^- \to \tilde{D}^{*0}K^-$ and the peaking background is more consistent. The distribution of ΔE for the $D^0\gamma$ shows a contribution from $D^0\pi$ events with a γ coming from combinatorial background, those events present a peak in m_{ES} and are shifted around $+100$ MeV in ΔE, as confirmed from the Monte Carlo simulation. They are parameterized with a second Gaussian in the ΔE distribution (Fig. 4.18).

Since the helicity distribution of the D^0 respect to the D^{*0} flight direction has different shapes for $D^0\pi^0$ and $D^0\gamma$, it can, in principle, be used to characterize the signal distribution. The D^* is a vector meson and it has to be fully polarized when it comes from the $B^- \to \tilde{D}^{*0}K^-$ decay. This explains the shapes of the helicity distribution which can be calculated assuming a decay of a polarized vector meson into 2 pseudoscalar in the case of $D^0\pi^0$, and into 1 pseudoscalar plus 1 vector in the case of $D^0\gamma$. The helicity

(a) $m_{ES}[\text{GeV}/c^2]$

(b) $\Delta E[\text{GeV}]$

(c) $M(K_S)$ $[\text{GeV}/c^2]$

(d) $M(D^0)$ $[\text{GeV}/c^2]$

(e) Δm $[\text{GeV}/c^2]$

(f) $|cos\theta_{thr.}|$
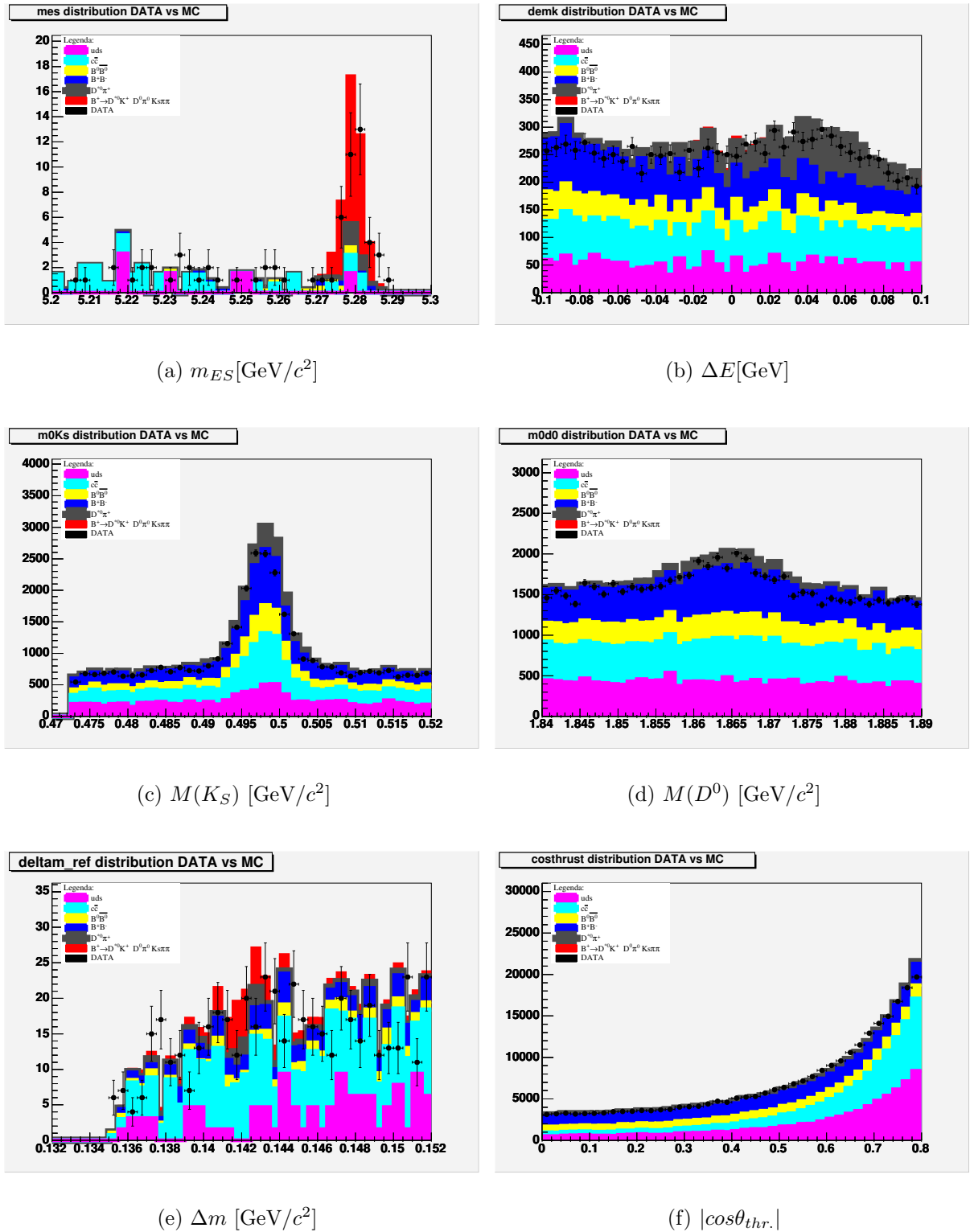
Figure 4.16: *Data - Monte Carlo comparison for $D^0\pi^0$ for the relevant variables used for the selection cuts.*

(a) m_{ES} [GeV/c^2]

(b) ΔE [GeV]

(c) $M(K_S)$ [GeV/c^2]

(d) $M(D^0)$ [GeV/c^2]

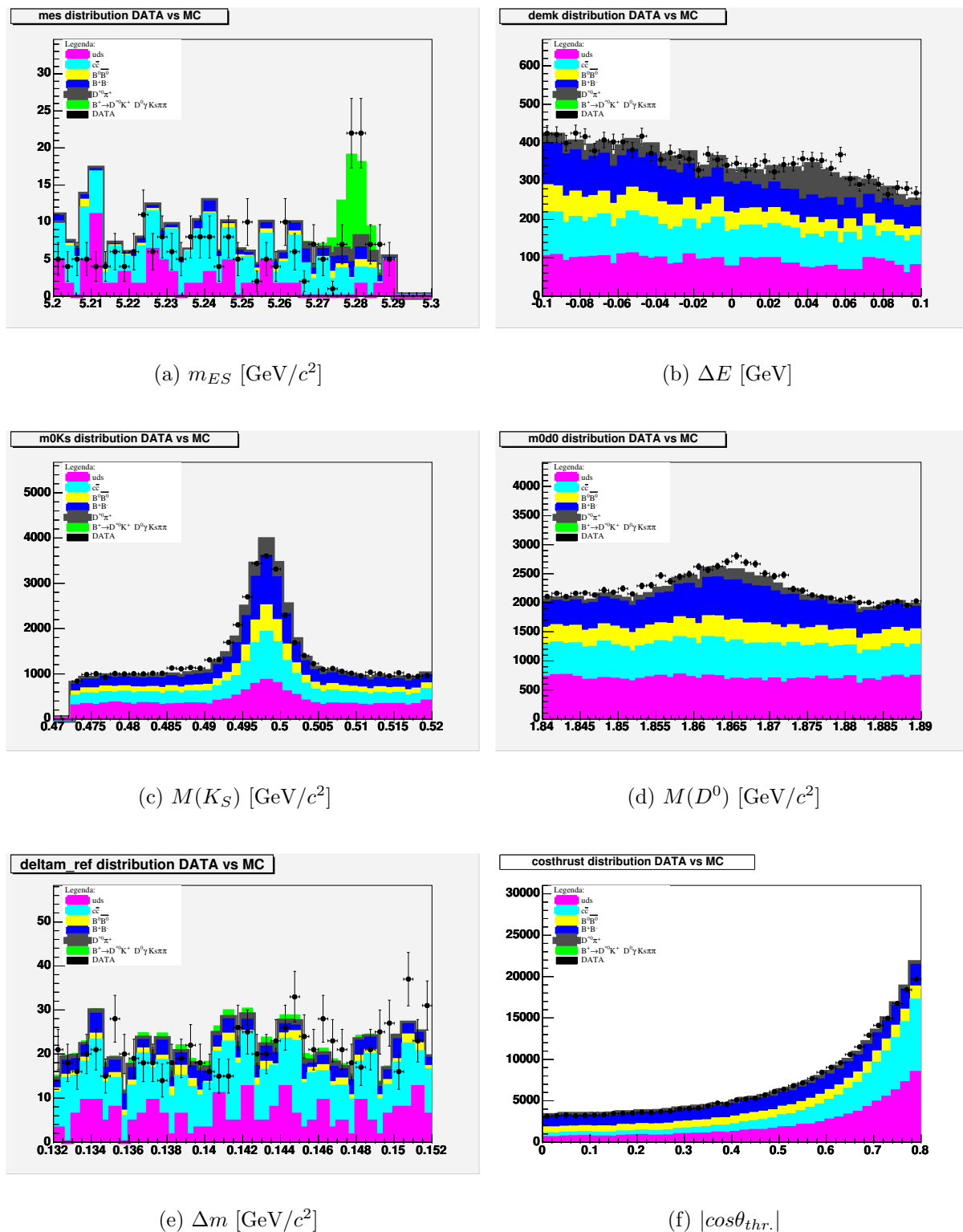(e) Δm [GeV/c^2]

(f) $|cos\theta_{thr.}|$

Figure 4.17: *Data - Monte Carlo comparison for $D^0\gamma$ for the relevant variables used for the selection cuts.*

shape is then $\propto cos(\theta_{Hel})^2$ for $D^0\pi^0$ and $\propto sin(\theta_{Hel})^2$ for $D^0\gamma$. Fig. 4.19 shows the Data-MC comparison after the selection cuts for the $B^- \rightarrow D^{*0}\pi^-$. Helicity cuts have been considered for the signal $B^- \rightarrow D^{*0}K^-$ but the significance and the purity of the sample does not improve significantly, for this reason this variable is avoided from the selection.

The background composition is studied for the $B^- \rightarrow D^{*0}\pi^-$. The composition of the background is quite different respect to the $B^- \rightarrow D^{*0}K^-$ sample due to the more relevant contribution of the $B\bar{B}$ events. The contamination of events $B^- \rightarrow D^{*0}K^-$ in the ΔE window (30 MeV with the pion hypothesis) is negligible. The fraction of signal events can be estimated from the m_{ES} fit: $f_s = \frac{N(D^*\pi)+N(peak)}{N_{\text{cand}}} = 0.96 \pm 0.03$ for $D^0\pi^0$ and 0.84 ± 0.02 for $D^0\gamma$, where $N(peak)$ is the number of peaking events in m_{ES}. The peaking contribution can be parameterized as a Gaussian on top of the ARGUS function which describes the combinatorial background as shown in Fig. 4.20.

The number of peaking events can be estimated on data performing a fit with the relative fraction $f_{rel} = 0.10 \pm 0.04$, of the peaking Gaussian to the ARGUS function fixed to the value from the fit on MC simulation. The fraction is consistent for $D^0\pi^0$ and $D^0\gamma$ and a common mean value is used. The parameters of the peaking Gaussian are also fixed to the values $\sigma_{peak} = 3.4$ MeV$/c^2$, $\mu_{peak} = 5.280$ MeV$/c^2$, from MC simulation fit. Fig. 4.21 shows the m_{ES} distribution and the fit result for $B^- \rightarrow D^{*0}\pi^-$ obtained after applying the final selection criteria.

4.3.5 Fisher discriminant

The major source of background events in this analysis is represented from continuum events. To separate these events a Fisher discriminant is used. The variables used in the Fisher discriminant are $cos\,\theta_{thr.}$, $cos\,\theta_B$ and the two Legendre monomials function of order 0 and of order 2. $\theta_{thr.}$ is the angle of the thrust axis of the B meson with respect to the rest of the event, while θ_B is the angle of the B meson with respect to the nominal z direction of the beams. A detailed description of the events shape variables and of the Fisher discriminant is given in Sec. 4.2.3. The $\theta_{thr.}$ is useful to separate jet events for which the variable is peaked around 1, from $B\bar{B}$ spherical events for which the variable is almost uniformly distributed. The $cos\,\theta_B$ variable takes into account the $\propto sin\theta_B^2$ distribution of the $B\bar{B}$ events with respect to the $\propto 1 + cos\theta_B^2$ of the continuum events in the rest frame of the $\Upsilon(4S)$.

The Fisher discriminant distribution is fitted with a double Gaussian for off resonance

(a) ΔE distribution for $D^0\pi^0$.

(b) ΔE distribution for $D^0\gamma$.

Figure 4.18: *The ΔE distribution for $B^- \to D^{*0}\pi^-$ obtained after applying the final selection criteria. Data are represented by point with error bars, the fit PDF is superimposed.*

(a) $cos(\theta_{Hel})$ distribution for $D^0\pi^0$.

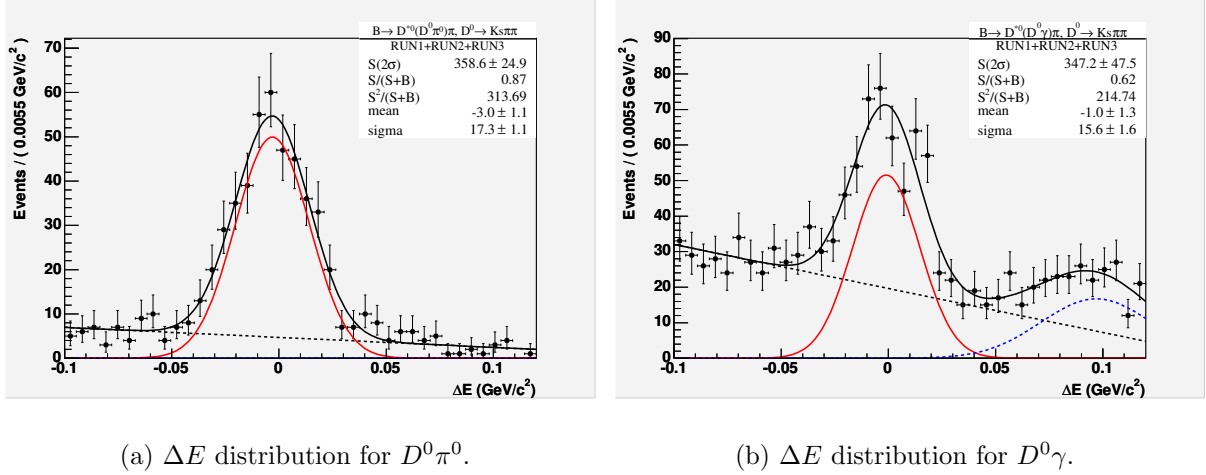(b) $cos(\theta_{Hel})$ distribution for $D^0\gamma$.
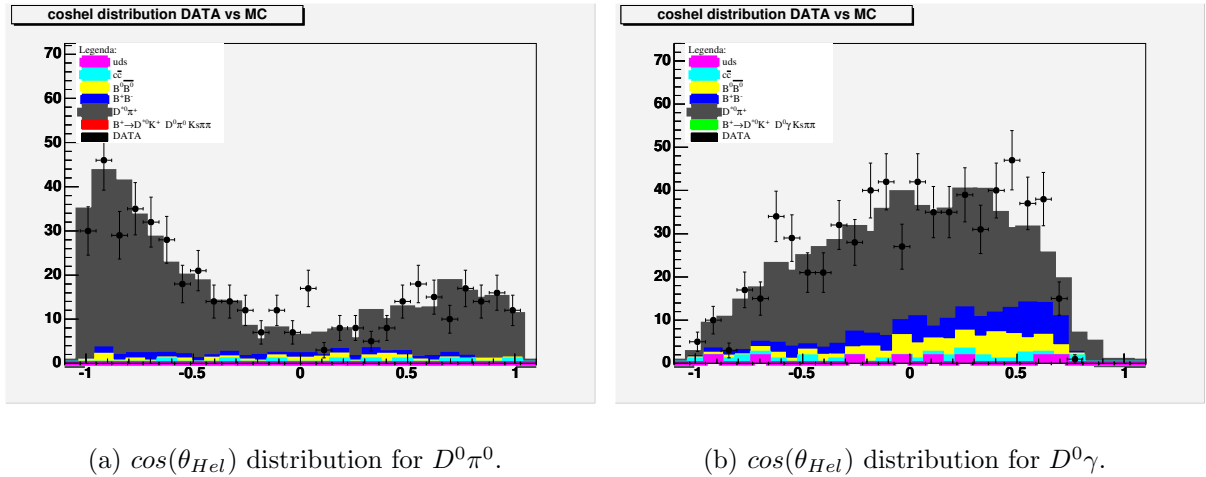
Figure 4.19: *The $cos(\theta_{Hel})$ distribution for $B^- \to D^{*0}\pi^-$ obtained after applying the final selection criteria. Data are represented by point with error bars.*
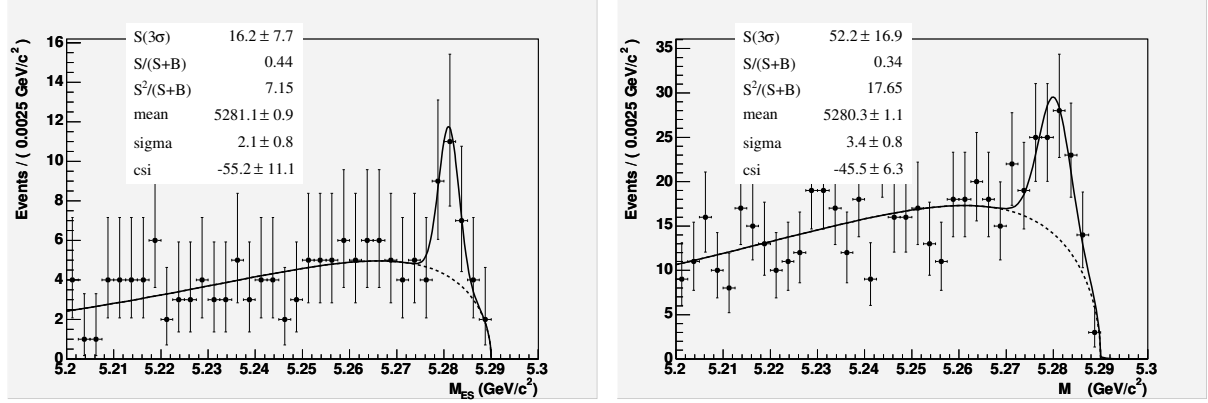
(a) m_{ES} distribution for $D^0\pi^0$ bkg events.

(b) m_{ES} distribution for $D^0\gamma$ bkg events.

Figure 4.20: *The m_{ES} distribution for $B^- \to D^{*0}\pi^-$ background events obtained after applying the final selection criteria. Data are represented by point with error bars, the fit PDF is superimposed. It is evident the contribution of peaking events which is parameterized with a Gaussian function on top of the ARGUS function.*

(a) Data m_{ES} distribution for $D^0\pi^0$

(b) Data m_{ES} distribution for $D^0\gamma$

Figure 4.21: *m_{ES} distribution for $B^- \to D^{*0}\pi^-$ obtained after applying the final selection criteria. Data are represented by point with error bars, the fit PDF is superimposed.*
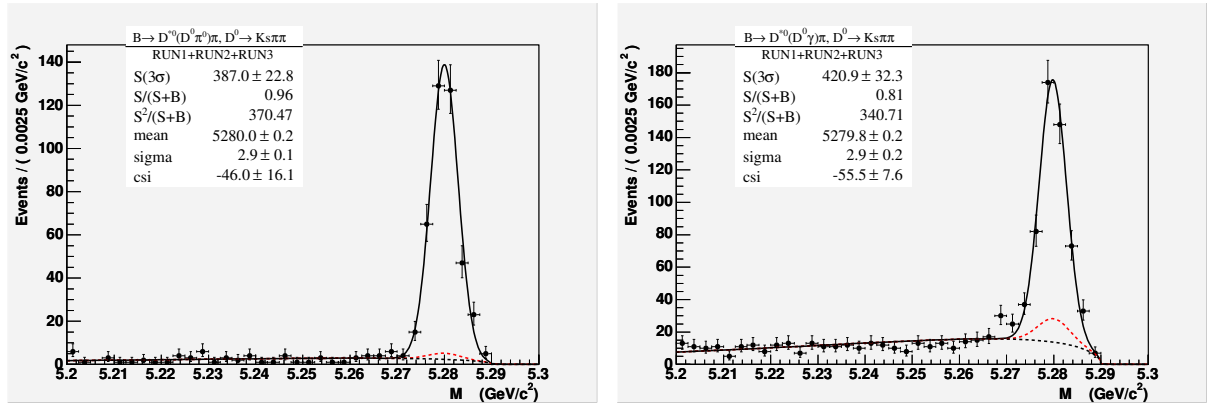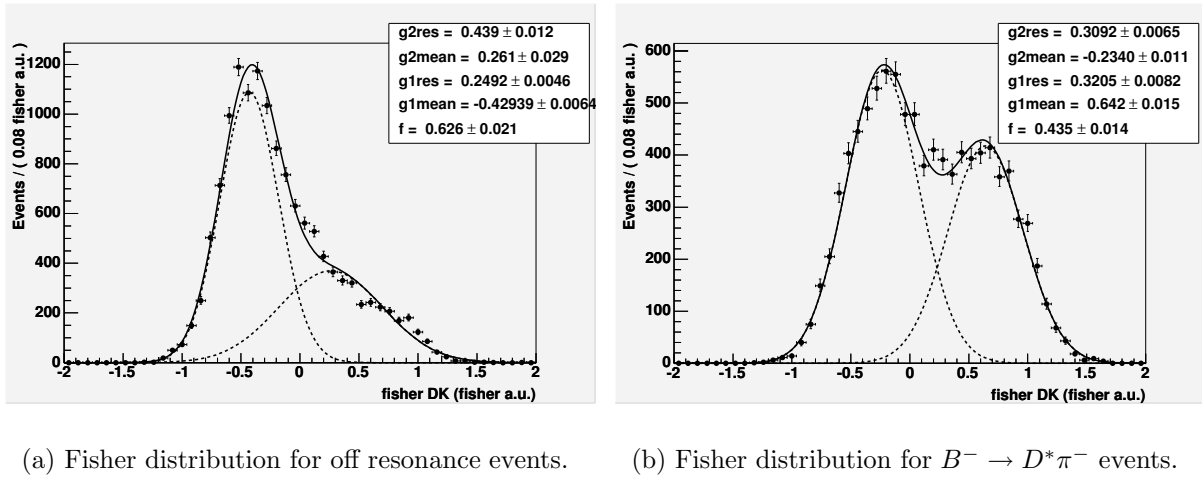
(a) Fisher distribution for off resonance events.

(b) Fisher distribution for $B^- \to D^*\pi^-$ events.

Figure 4.22: *The fisher distributions for off resonance data and $B^- \to D^*\pi^-$ events. Data are represented by point with error bars, the fit PDF is superimposed.*

events and for $B^- \to D^*\pi^-$ events. The agreement is pretty consistent with the Fisher parameterization used for the D^0K analysis.

Fig. 4.22 shows the fisher distributions for off resonance data and $B^- \to D^*\pi^-$ events.

4.3.6 Background Dalitz shape

The Dalitz parameterization for continuum and for $B\bar{B}$ combinatorial events is different in principle, as the continuum events are dominated by combinatorics tracks while the $B\bar{B}$ events have more consistent contamination of signal-like events. The off-resonance events distribution is consistent with a flat distribution as shown in Fig. 4.23 then the Dalitz distribution of continuum events is assumed to be flat. For the Dalitz background parameterization $B\bar{B}$ Monte Carlo events and off-resonance data are selected in order to have a reasonable statistics using the D^0 sidebands in the range $|\Delta E| < 100$ MeV. Due to the low statistics of the $B\bar{B}$ background it cannot be excluded an agreement with a flat distribution in the Dalitz plot for the $D^0\pi^0$, even if a different structure in the $D^0\gamma$ is visible. A fit of the Dalitz distribution for the $m^2(K_S, \pi^+)$ and $m^2(K_S, \pi^-)$ is also performed with a 2D symmetric second order polynomial function:

$$a_0 + a_1(x + y) + a_2(x^2 + y^2 + xy) \, , \tag{4.11}$$

with $m^2(K_s\pi^+) \equiv x$ and $m^2(K_s\pi^-) \equiv y$.
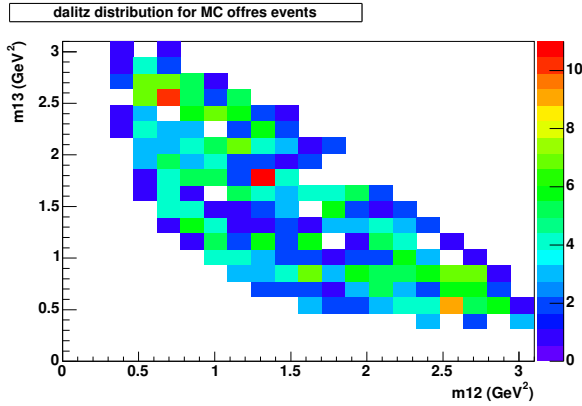
(a) $D^0\pi^0$ distribution
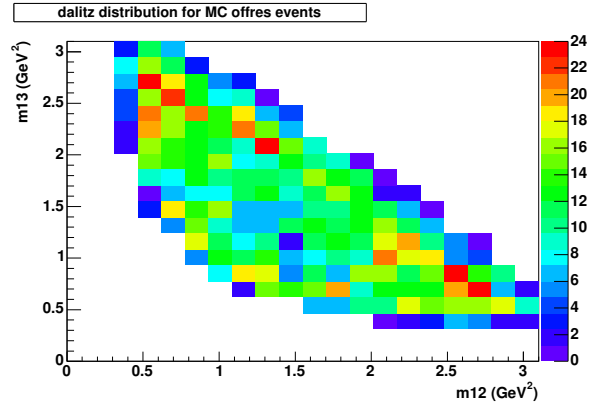
(b) $D^0\gamma$ distribution

(c) $m^2(K_S, \pi^\pm)$ distribution for $B^\pm$ candidates for off-resonance events for $D^0\pi^0$ selection

(d) $m^2(K_S, \pi^\mp)$ distribution for $B^\pm$ candidates for off-resonance events for $D^0\pi^0$ selection.
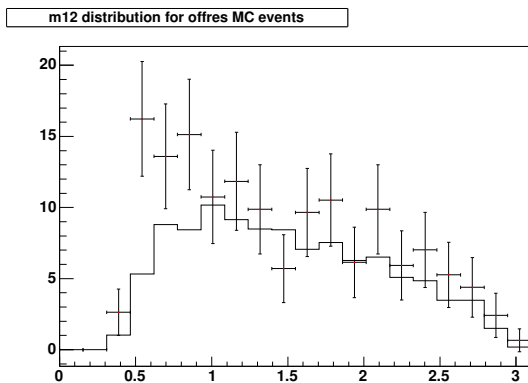
(e) $m^2(K_S, \pi^\pm)$ distribution for $B^\pm$ candidates for off-resonance events for $D^0\gamma$ selection
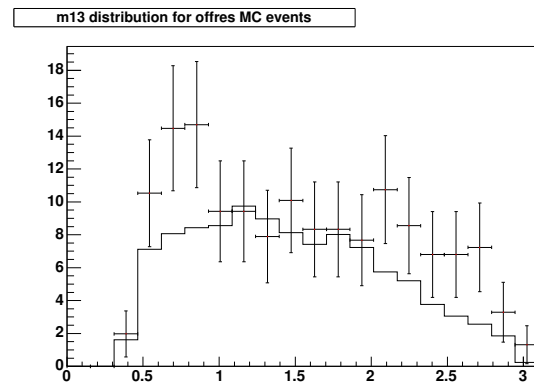
(f) $m^2(K_S, \pi^\mp)$ distribution for $B^\pm$ candidates for off-resonance events for $D^0\gamma$ selection.

Figure 4.23: *Distributions of $m^2(K_S, \pi^\pm)$ and $m^2(K_S, \pi^\mp)$ for $B^\pm$ candidates Off-resonance events are represented by point with error bars, the continuous line represent a flat distribution in the Dalitz plot.*

(a) $D^0 \pi^0$ distribution

(b) $D^0 \gamma$ distribution

(c) $m^2(K_S, \pi^\pm)$ distribution for $B^\pm$ candidates for $B\bar{B}$ events for $D^0 \pi^0$ selection

(d) $m^2(K_S, \pi^\mp)$ distribution for $B^\pm$ candidates for $B\bar{B}$ events for $D^0 \pi^0$ selection.

(e) $m^2(K_S, \pi^\pm)$ distribution for $B^\pm$ candidates for $B\bar{B}$ events for $D^0 \gamma$ selection
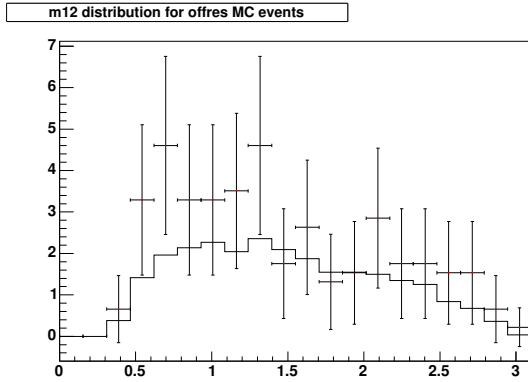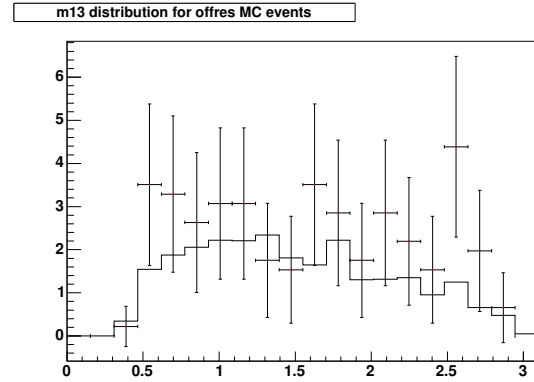
(f) $m^2(K_S, \pi^\mp)$ distribution for $B^\pm$ candidates for $B\bar{B}$ events for $D^0 \gamma$ selection.
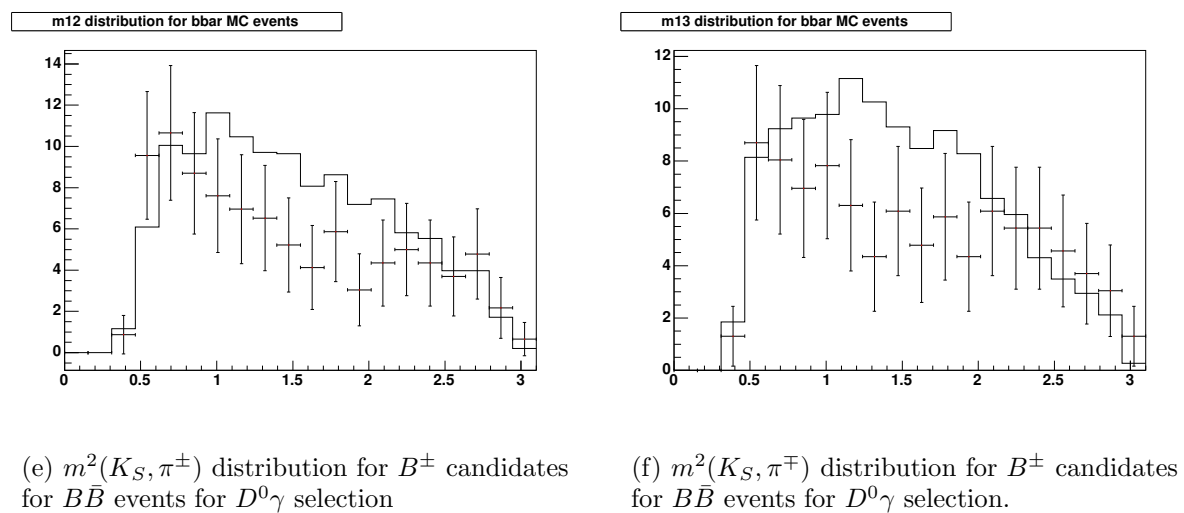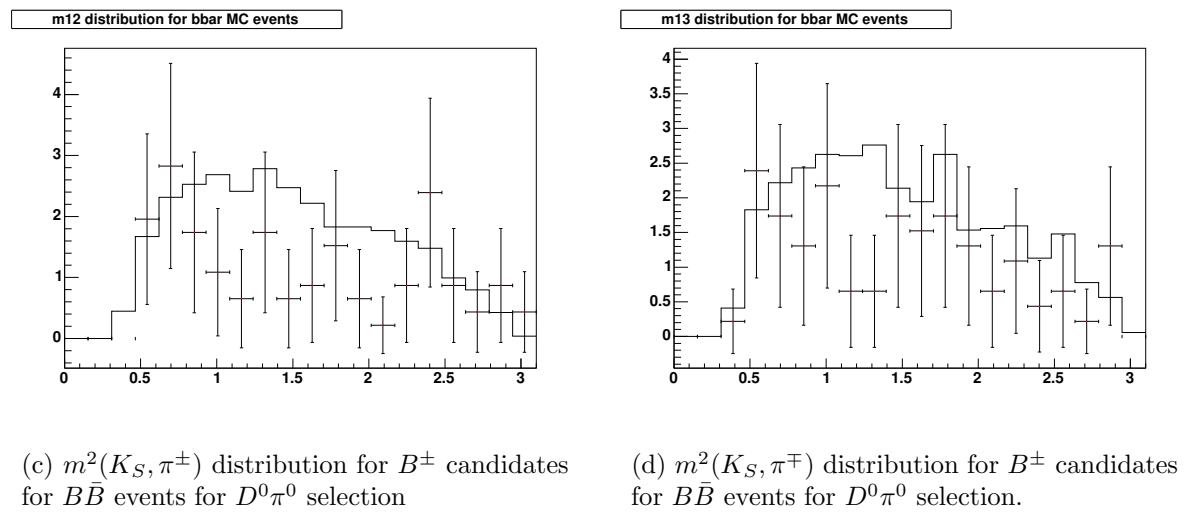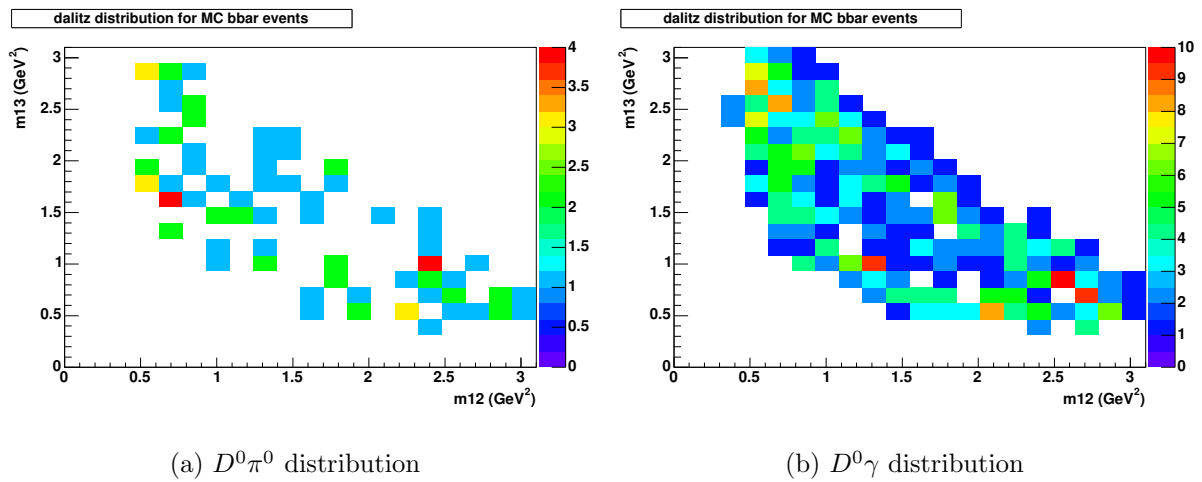
Figure 4.24: *Distributions of $m^2(K_S, \pi^\pm)$ and $m^2(K_S, \pi^\mp)$ for $B^\pm$ candidates. $B\bar{B}$ events are represented by point with error bars, the continuous lines represent a flat distribution in the Dalitz plot.*

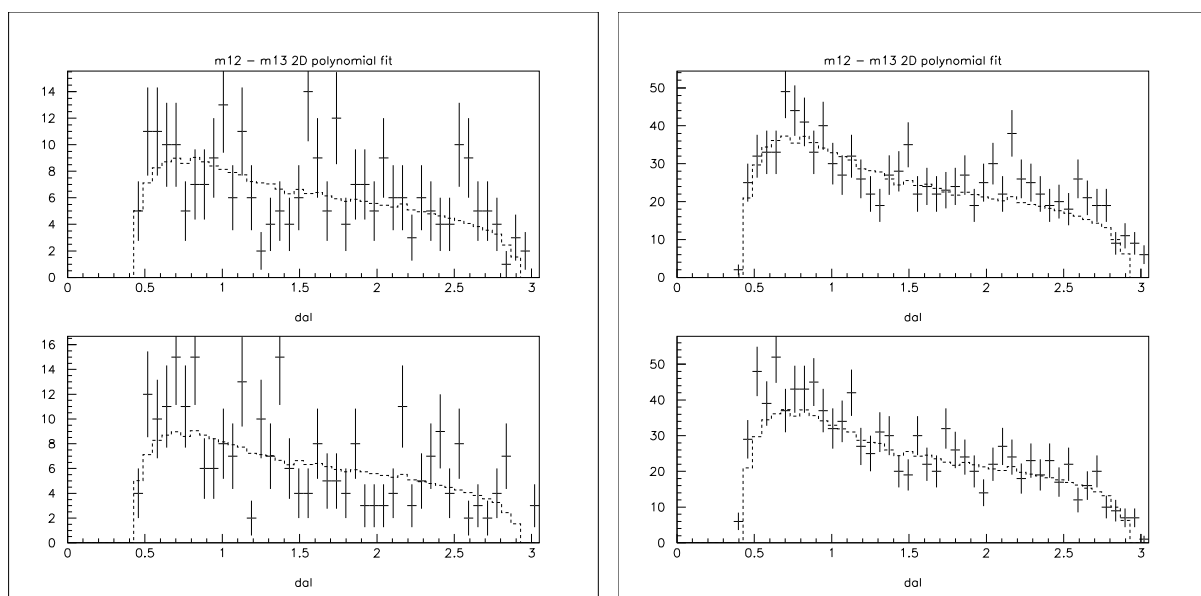(a) Distribution for $D^0\pi^0$ events.　　　　　(b) Distribution for $D^0\gamma$ events.

Figure 4.25: *Distributions of $m^2(K_S, \pi^\pm)$ (top plot) and $m^2(K_S, \pi^\mp)$ (bottom plot) for $B^\pm$. The points represent the $B\bar{B}$ Monte Carlo events, the histogram the result of the second order polynomial fit.*

In Figs. 4.23 and 4.24 are reported the relevant distribution for the $B\bar{B}$ background and for the continuum events. In Fig. 4.25 is reported the distribution for MC $B\bar{B}$ events $((K_s\pi^+) \, vs \, (K_s\pi^-))$. The histogram of the second order polynomial function from the fit is overimposed.

4.4 $B^- \to \tilde{D}^0 K^{*-}$ selection

4.4.1 Events selection

The D^0 and the K_S coming from the D^0 decay are reconstructed using the same selection criteria used for the $B^- \to \tilde{D}^0 K^-$ selection. The K^{*-} is reconstructed in the $K^{*-} \to K_S\pi^-$ channel. Since the K_S from the D^0 and the K_S from the K^{*-} have very similar invariant mass resolution the same selection criteria are used for both of them. It's also required that $\cos\alpha_{K_S}(K^*) > 0.99$ where $\alpha_{K_S}(K^*)$ is the angle between the K_S direction of flight (line between the B vertex, that corresponds to the K^* vertex and the K_S vertex) and its momentum. This cut is useful to suppress background of the type $B^- \to D^0 X^-(X^- \to 3\pi)$ (for example $X^- = a_1^-$).

For the selection the invariant mass of the K^* and the cosine of the helicity angle of the K^* daughters are also used. $\cos\theta_{Hel}$ is defined as the angle in the K^* rest frame between the direction of flight of a K^* daughter with respect to the direction of flight of the K^* in the B rest frame (Fig. 4.26). As a cross check, the significance variation depending on the K^* mass cut and the cosine of the helicity cut is plotted in Fig. 4.27. This plot is in agreement with the previous values than the selection is fixed as $|m_{K^*} - m_{K^*}(PDG)| < 55$ MeV/c^2 and $|\cos\theta_{Hel}| > 0.35$. Since the K^* has spin 1 the angular distribution is a function of the helicity angle, $\frac{dN}{d(\cos\theta_{Hel})} \propto \cos^2\theta_{Hel}$. The distribution for background events instead is rather flat. In order to be consistent with the definition of the Fisher discriminant used for the $B^- \to \tilde{D}^0 K^-$ selection, the same cut on $|cos\theta_{thr}| < 0.8$ is applied.

The final selection criteria, optimized in order to maximize the statistical significance, are:

- $|m_{K_S}(D^0) - m_{K_S}(PDG)| < 9$ MeV/c^2

- $|m_{K_S}(K^*) - m_{K_S}(PDG)| < 9$ MeV/c^2

- $|m_{D^0} - m_{D^0}(PDG)| < 12$ MeV/c^2

- $|\cos\theta_{thr})| < 0.8$

- D^0 and B vertex fit procedure required to converge

- $\cos\alpha_{K_S}(D^0) > 0.99$

- $\cos\alpha_{K_S}(K^*) > 0.99$

- $|m_{K^*} - m_{K^*}(PDG)| < 55$ MeV/c^2

- $|\cos\theta_{Hel}| > 0.35$

- $|\Delta E| < 25$ MeV

- $m_{ES} > 5.2$ MeV/c^2

The overall reconstruction efficiency for signal events is $\epsilon_{Sig} = (11.1 \pm 0.5)\%$ after all selection criteria are applied. The significance of the signal in the final signal region $|\Delta E| < 25$ MeV and $m_{ES} > 5.270$ GeV/c^2 is $S/\sqrt{S+B} = 6.2$.

4.4.2   Sample composition

The larger component of background comes from continuum events. This component can be suppressed with the cut on $|\cos\theta_T| < 0.8$ and with the use of the Fisher discriminant in the CP likelihood fit. The fraction of continuum events, $f_{cont} = \frac{N_{cont}}{N}$, after all the cuts applied in the region $m_{ES} > 5.2$ GeV/c^2 is obtained counting from Monte Carlo simulation and the values obtained is $f_{cont,MC} = 0.60 \pm 0.02$ close to the one obtained with the CP fit $f_{cont,Data} = 0.74 \pm 0.07$ from the data sample. The $B\bar{B}$ events have similar event shape distribution to the signal and they are suppressed with a tight cut on $|\Delta E| < 25$ MeV.

The $B^- \to \tilde{D}^0 K^{*-}$ decay can present background coming from decay modes with the same final state particles of the signal. The signal final state is:

$$D^0 K^{*-} \quad = \quad [(\pi^+\pi^-)_{K_S}\pi^+\pi^-]_{D^0} \quad [(\pi^+\pi^-)_{K_S}\pi^-]_{K^{*-}} \ . \tag{4.12}$$

Different decay modes are considered and they are found negligible.

The $D^0_{4\pi}K^{*-}$ decay mode has a branching ratio smaller than to the signal, $Br(D^0 \to 4\pi) = (7.3 \pm 0.5) \cdot 10^{-3}$. The contribution of this decay mode is negligible after applying the request on $\cos\alpha_{K_S} > 0.99$.
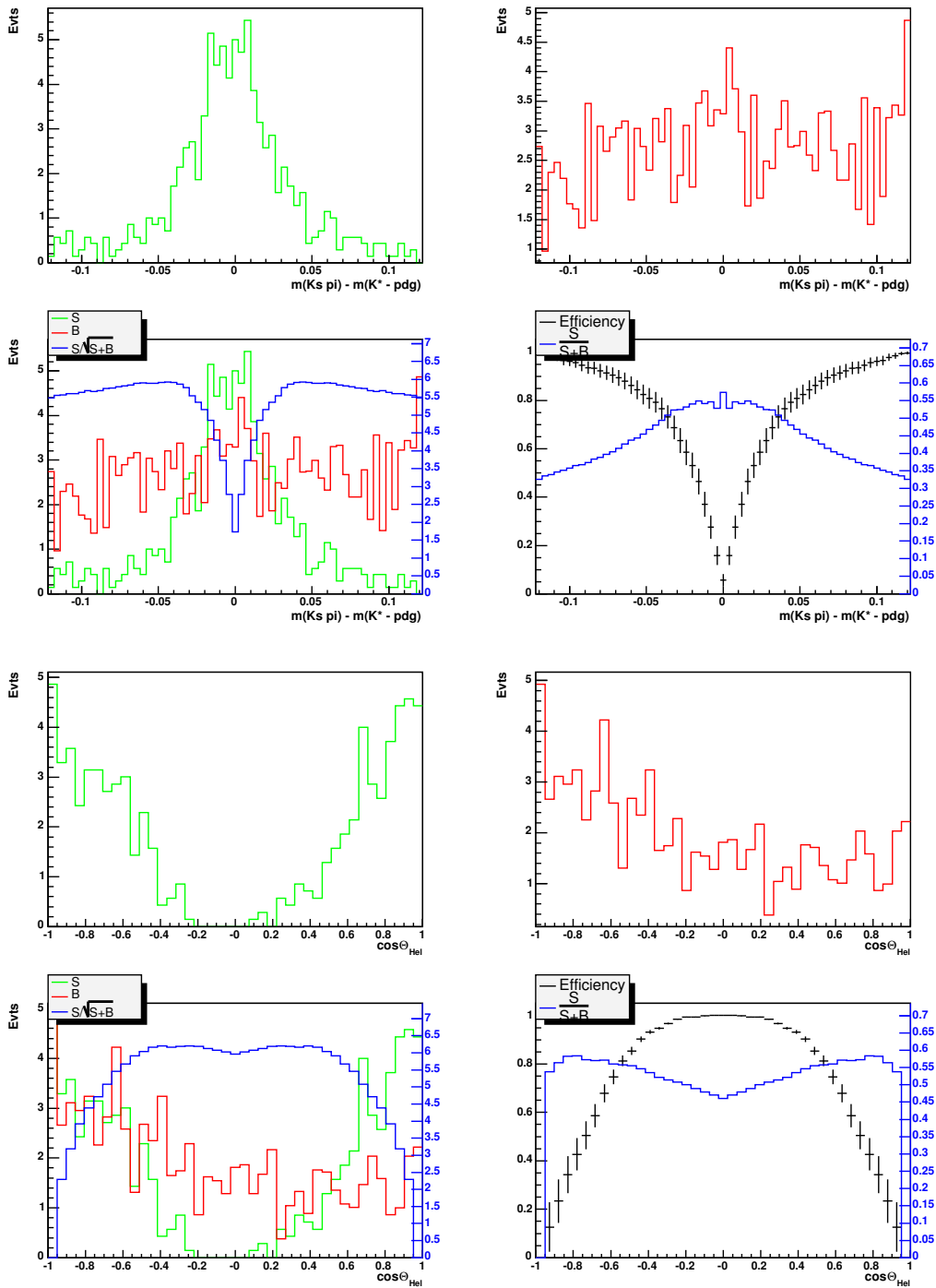
Figure 4.26: *In top-left plot (green) the distribution of the variable for the signal. In the top-right plot the variable distribution for the background. In bottom-left the significance as a function of the cut on the selected variable and in bottom-right the purity (histogram) and the efficiency (point with error bars) as a function of the cut. (Top 4 plots) Sequence of plot described above for the invariant mass of the K^{*-}. (Bottom 4 plots) Same plots for $\cos\theta_{Hel}$ of the K^{*-} daughters.*
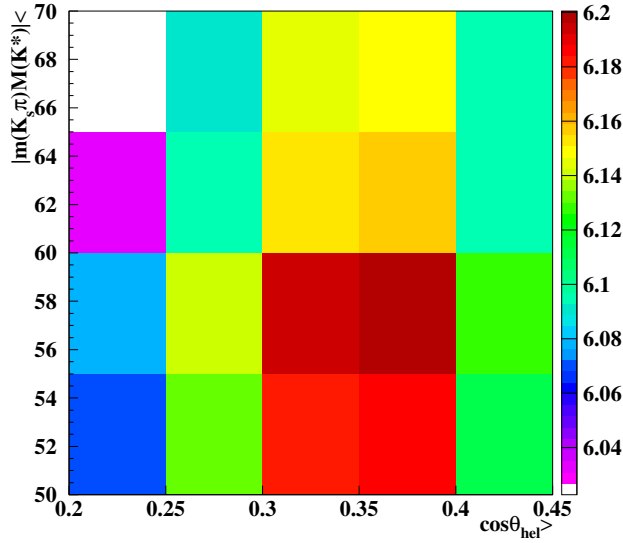
Figure 4.27: *2D plot of the significance with respect to the cut on the K^* mass and the cut on $\cos\theta_{Hel}$. The color scale represent the value of the significance, it increases from blue to red. The maximum value is 6.2 with $|m_{K^*} - m_{K^*}(PDG)| < 55$ MeV/c^2 and $|\cos\theta_{Hel}| > 0.35$.*

The $K_S K_S K^{*-}$ decay mode has a branching ratio not reported on the PDG but it is present in the generic $B\bar{B}$ Monte Carlo used for this analysis. This contribution is found negligible after all the selection criteria are applied. No events are found on $\simeq 1$ ab^{-1} $B\bar{B}$ Monte Carlo sample where the decay mode was generated assuming $Br(B^- \to K^0\bar{K}^0 K^{*-}) = 10^{-5}$. Evidence of this background is searched on data in the D^0 sidebands (*i.e.* $|m_{D^0} - m_{PDG}| > 20$ MeV/c^2 corresponding to almost 5 times the D^0 mass signal region) fitting the m_{ES} distribution after all the selection criteria applied and no statistical evidence of this background is found.

The $D^0\pi^-\pi^+\pi^-$ decay mode has a relatively large branching ratio $Br(B^- \to D^0\pi^-\pi^+\pi^-) = (1.1 \pm 0.4)\%$ and it includes $Br(B^- \to D^0 a_1^-) = (6.0 \pm 3.3) \cdot 10^{-3}$. 3 events of this decay mode are found in $\simeq 1$ab^{-1} $B\bar{B}$ Monte Carlo sample then this contribution can be neglected.

The $D^0 K_S \pi^-$ mode presents an identical final state to the signal but the $(K_S\pi^-)$ system decays with relative angular momentum L=0 instead of L=1. These events are considered actually as signal events in the CP likelihood fit as they reach the final state through $b \to u$ and $b \to c$ interfering amplitudes. These events will be referred in the

(a) Data

(b) Monte Carlo

Figure 4.28: *The fit to the D^0 distribution shows evidence of true D^0 background events. The events are selected in the m_{ES} sidebands ($m_{ES} < 5.27$ GeV/c^2) with all the selection cuts applied.*
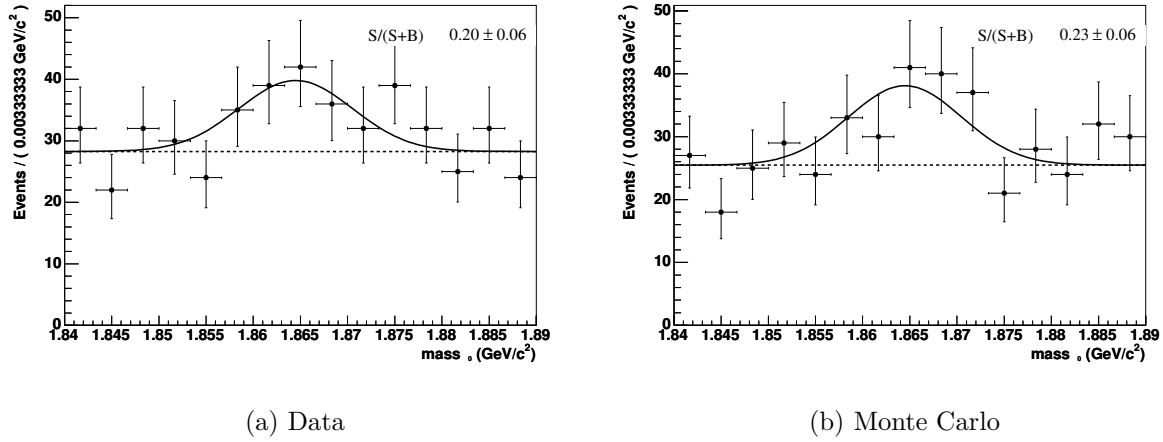
follow as *signal Non-Resonant*. It is shown in [55] that signal Non-Resonant has a relative contribution of $< 5\%$ respect to the $D^0 K^{*-}$, in another $B^- \rightarrow D^0 K^{*-}$ analysis.

As in the case of $B^- \rightarrow \tilde{D}^0 K^-$, the background events are divided in events with true D^0 and with false D^0 in order to characterize the Dalitz shape. The estimate of the fraction of true D^0 (R), is done on Monte Carlo events. The values are reported in Tab. 4.4, together with the fraction of right-sign D^0, $R^{RS} = \frac{N_{D^0 h^{*-}}}{N_{D^0 h^{*-}} + N_{\bar{D}^0 h^{*-}}}$ where h^{*-} is a candidate K^{*-}. The fraction of true D^0 is evaluated also on data considering the m_{ES} sidebands. The fraction can be extracted from a fit to the D^0 invariant mass using as a Gaussian for the D^0 signal plus a constant for the background. Due to the small statistics the mean of the Gaussian is fixed to $\mu_{D^0} = 1864.5$ MeV/c^2 and the width to $\sigma_{D^0} = 6.0$ MeV/c^2 from signal Monte Carlo fitted values. Since the fraction of true D^0 is compatible within the errors in $B\bar{B}$ and continuum Monte Carlo events, it is assumed the same also in data. Fig. 4.28 shows the fit to the D^0 invariant mass distribution for data and for Monte Carlo events.

After all the selection criteria are applied, the multiplicity of candidates on data in the signal region ($M_{ES} > 5.270$ MeV/c^2, $|\Delta E| < 25$ MeV) is $N_{cand} = 1.055 \pm 0.005$. The best candidate per event is chosen according to the minimum value of the $\chi^2 = \chi^2(m_{D^0}, m_{K^*})$:

$$\chi^2(m_{D^0}, m_{K^*}) = \frac{(m_{D^0} - m_{D^0,PDG})^2}{\sigma_{D^0}^2} + \frac{(m_{K^*} - m_{K^*,PDG})^2}{\sigma_{K^*}^2 + \Gamma_{K^*}^2} , \qquad (4.13)$$

Fraction	Estimate from generic MC	Estimate from data
R_{Cont} (real D^0's in Cont)	0.21 ± 0.02	0.20 ± 0.06
$R_{B\bar{B}}$ (real D^0's in $B\bar{B}$)	0.18 ± 0.02	0.20 ± 0.06
R_{Cont}^{RS} ($D^0 K^{*-}$ in Cont)	0.51 ± 0.06	-
$R_{B\bar{B}}^{RS}$ ($D^0 K^{*-}$ in $B\bar{B}$)	0.67 ± 0.06	-

Table 4.4: *D^0 fractions for background events are estimated from generic MC and data, for the region $|\Delta E| < 25$ MeV and $m_{ES} > 5.2$ GeV/c^2. In data the m_{ES} region is restricted to $5.2 < m_{ES} < 5.27$ GeV/c^2 to exclude the signal events.*

where σ is the experimental resolution on Monte Carlo signal events and Γ_{K^*} is the intrinsic width of the K^*. The efficiency of the best candidate choice for signal events is approximatively $\epsilon_{best} = 75\%$, evaluated on Monte Carlo signal events.

4.4.3 Data - Monte Carlo comparison

Data - Monte Carlo comparison is performed for the relevant variables used in the events selection. For all the plots the colored histograms display the various Monte Carlo components and the points the data. Fig. 4.29 shows the comparison for $cos(\theta_{thr})$, $cos\theta_{Hel}$, the D^0 and K_S mass, ΔE and m_{ES}. A shift is evident in the m_{ES} distribution that can be quantified as $\Delta m_{ES} = 1.7$ MeV/c^2.

4.4.4 Efficiency and Background Dalitz shapes

The Dalitz model PDF has to be corrected by efficiency non-uniformities across the Dalitz plot, $\epsilon(m_+^2, m_-^2)$. The correction is obtained by performing an unbinned fit to a third order polynomial to the signal Monte Carlo where the D^0 was allowed to decay isotropically

$$P(x, y) = 1 + a_1 \ (x + y) + a_2 \ (x^2 + y^2 + xy) + a_3 \ (x^3 + y^3 + x^2y + xy^2) \ . \qquad (4.14)$$

The parameterization is symmetrized for $x = m_+^2$ and $y = m_-^2$. Fig. 4.30 shows the Dalitz plot distribution and the m_+^2 and m_-^2 projections for this signal Monte Carlo sample. In this figure the blue curves represent the result of the 3rd order polynomial fit, and the red curves represent the projection for a perfectly flat efficiency. It can be seen that except at the borders of the kinematically allowed region the efficiency correction is quite consistent with a flat distribution.

The Dalitz distributions for the different background components (continuum, $B\bar{B}$), are evaluated from continuum and generic $B\bar{B}$ Monte Carlo events after having removed

(a) $cos(\theta_{thr})$

(b) $cos\theta_{Hel}$

(c) D^0 mass [GeV/c^2]

(d) K_S mass [GeV/c^2]

(e) m_{ES} [GeV/c^2]
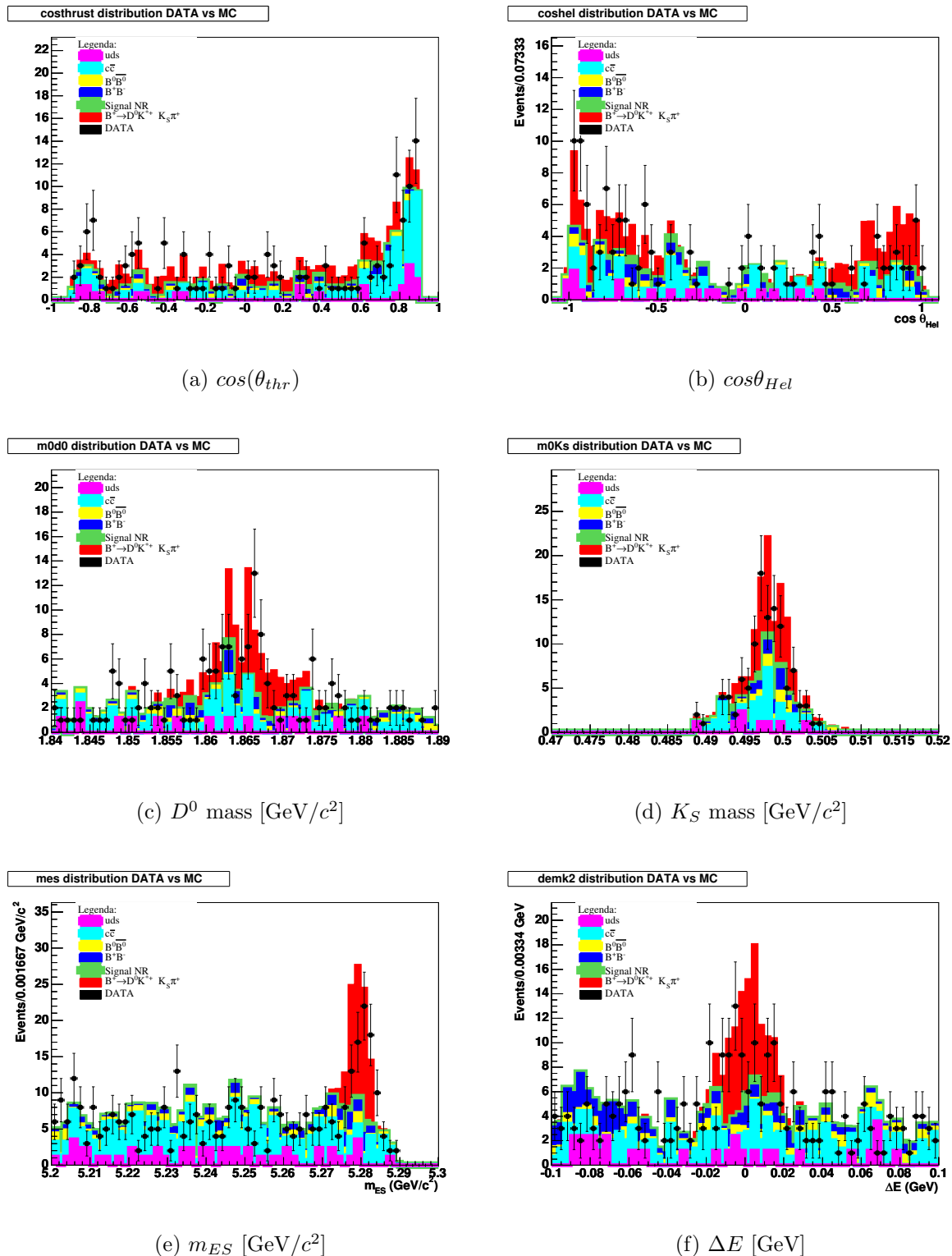

(f) ΔE [GeV]

Figure 4.29: *Data - Monte Carlo comparison of the relevant variables used for the selection cuts. The events in the plots are selected applying all the selection criteria but the one on the displayed variable.*

events with real D^0. The distributions for continuum and $B\bar{B}$ are fitted to a symmetric second order polynomial function, as given in Eq. (4.14) with $a_3 = 0$. The distributions and fit results are shown in Figs. 4.31 and 4.32, for continuum and $B\bar{B}$ respectively.

The continuum Dalitz shape is also extracted from off-resonance data by selecting the D^0 mass sidebands in order to exclude the real D^0 (D^0 mass is required to be smaller than 1.85 GeV/c^2 and larger than 1.88 GeV/c^2. Although the statistics is poor the shape from off-resonance data agrees with that observed from the continuum Monte Carlo.

4.4.5 D^0 fractions

The fraction of true D^0 (R) and right-sign D^0 R^{RS} for continuum and $B\bar{B}$ events is reevaluated on Monte Carlo events by counting as described in section 4.4.2 but after applying the best candidate choice algorithm. The values are reported in Tab. 4.5, which are essentially unchanged compared to Tab. 4.4.

Fraction	Estimate from generic MC
R_{Cont} (real D^0 in Cont)	0.205 ± 0.022
$R_{B\bar{B}}$ (real D^0 in $B\bar{B}$)	0.180 ± 0.021
R_{Cont}^{RS} ($D^0 K^{*-}$ in Cont)	0.53 ± 0.06
$R_{B\bar{B}}^{RS}$ ($D^0 k^{*-}$ in $B\bar{B}$)	0.67 ± 0.06

Table 4.5: D^0 *fractions as estimated from generic MC, for the region* $|\Delta E| < 25$ *MeV and* $m_{ES} > 5.2$ *GeV/c^2.*

4.4.6   Fraction of wrong sign signal events

According to the phase space Monte Carlo and applying the best candidate choice algorithm, the fraction of wrong sign signal events is found to be 0.0043 ± 0.0005 for $m_{ES} > 5.2$ GeV/c^2. Therefore this component is neglected in the final fit.
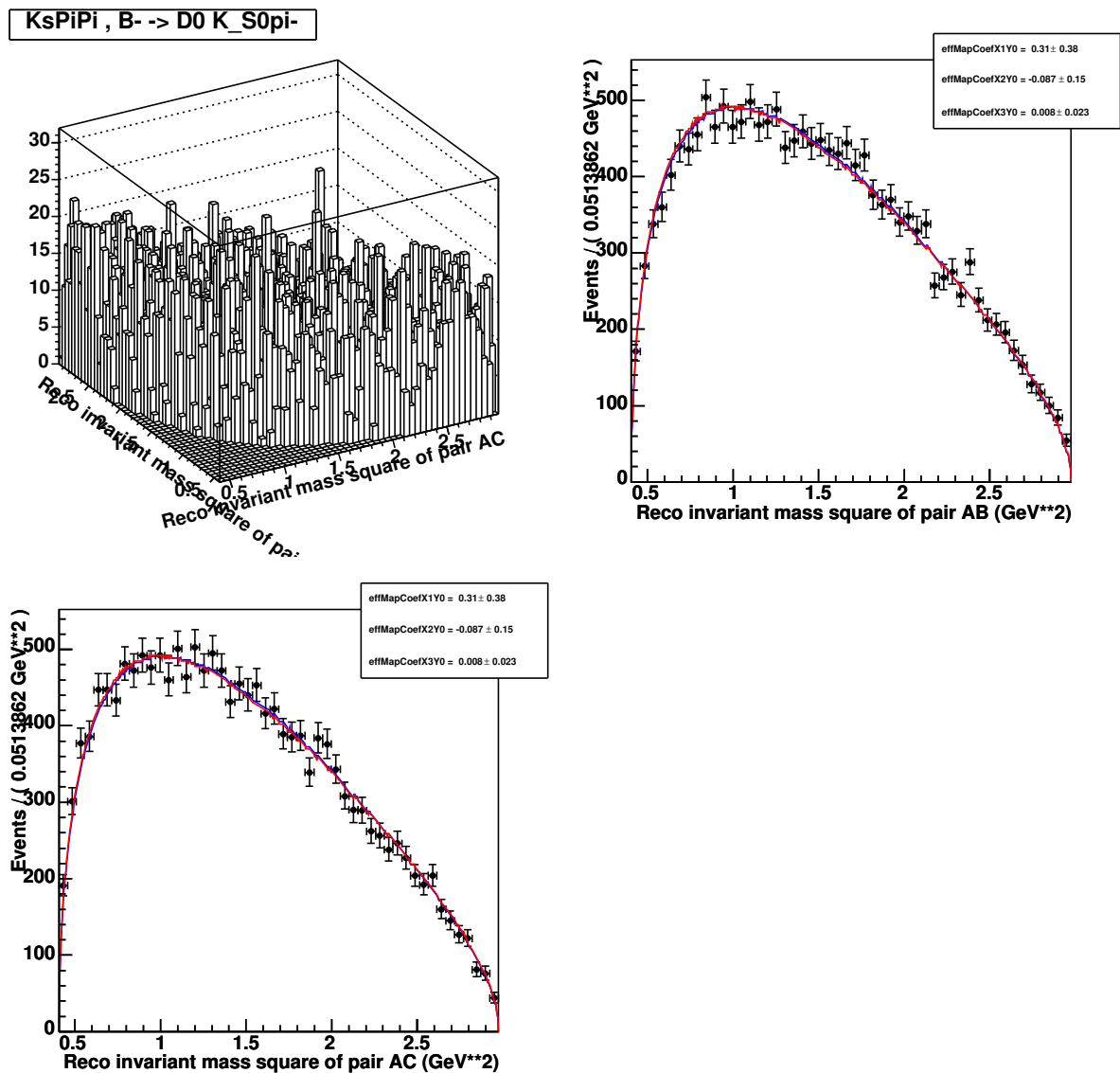
Figure 4.30: *Dalitz efficiency mapping for signal MC (phase space), for $|\Delta E| < 25$ MeV and $m_{ES} > 5.2$ GeV/c^2 ($m^2_{AB} \equiv m^2_+$, $m^2_{AC} \equiv m^2_-$, $m^2_{BC} \equiv m_{\pi^+\pi^-}$). The blue curve is the result of an unbinned likelihood fit to a second order polynomial (after symmetrization of the Dalitz plot) to the $B^- \to \tilde{D}^0 K^{*-}$ signal Monte Carlo, while the red curve corresponds to a phase space distribution.*

Figure 4.31: *continuum background Dalitz shape from generic Monte Carlo, for* $|\Delta E| < 25$ *MeV and* $m_{ES} > 5.2$ *GeV/c^2 ($m^2_{AB} \equiv m^2_+$, $m^2_{AC} \equiv m^2_-$ and $m^2_{BC} \equiv m_{\pi^+\pi^-}$). The blue curve is the result of an unbinned likelihood fit to a second order polynomial (after symmetrization of the Dalitz plot), while the red curve corresponds to a phase space distribution.*

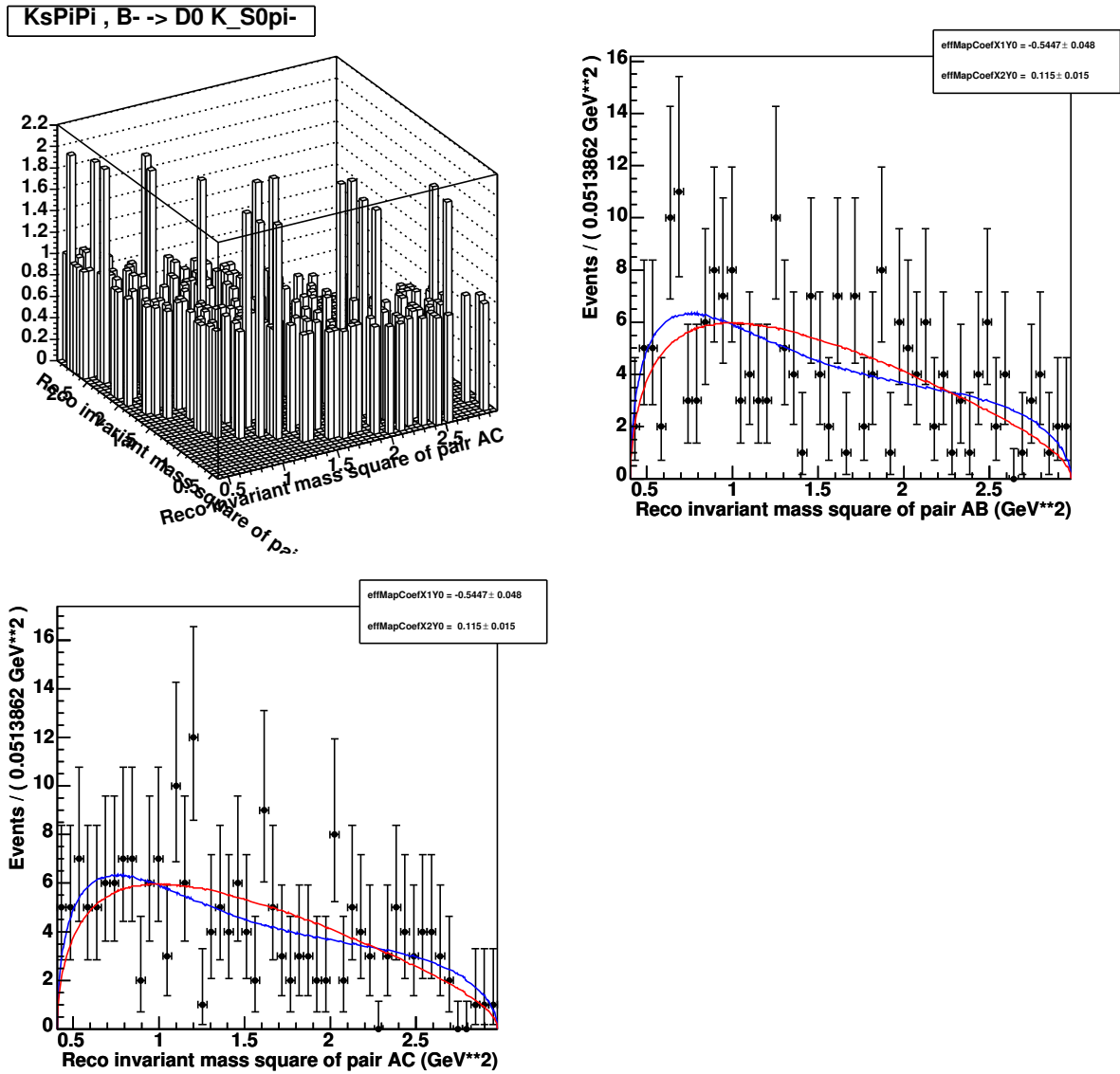Figure 4.32: $B\bar{B}$ background Dalitz shape from generic Monte Carlo, for $|\Delta E| < 25$ MeV and $m_{ES} > 5.2$ GeV/c^2 ($m_{AB}^2 \equiv m_+^2$, $m_{AC}^2 \equiv m_-^2$ and $m_{BC}^2 \equiv m_{\pi^+\pi^-}$). The blue curve is the result of an unbinned likelihood fit to a second order polynomial (after symmetrization of the Dalitz plot), while the red curve corresponds to a phase space distribution.
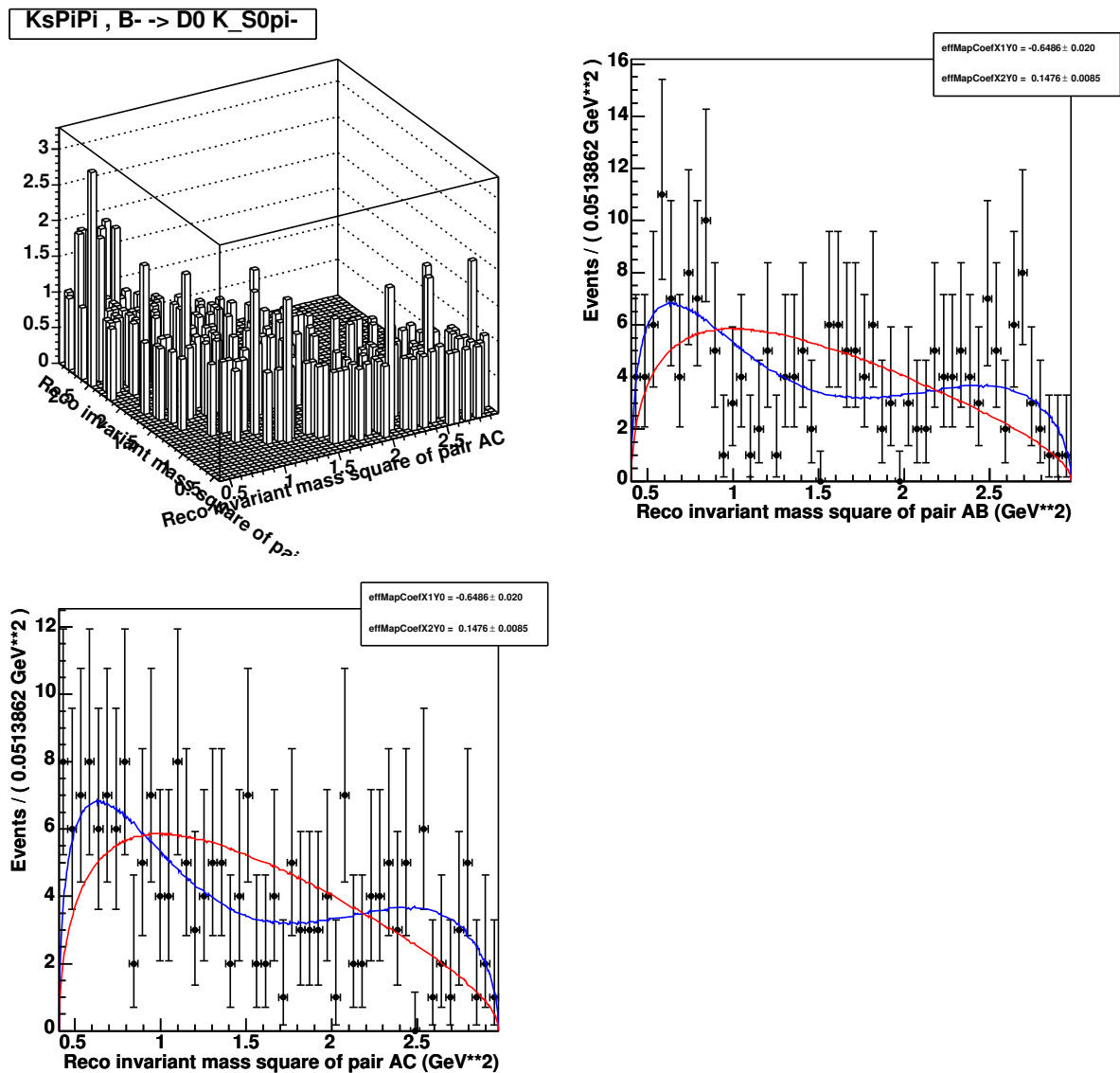
Chapter 5

Measurement of the CP parameters

A maximum likelihood fit technique is used to extract the CP parameters. As described in detail in Sec. 1.4 the decay chain $B^{\mp} \to \tilde{D}^{(*)0}K^{\mp}$ rate can be written as:

$$\Gamma_{\mp} \propto |A_D(m_{\mp}^2, m_{\pm}^2)|^2 + r_B^{(*)2}|A_D(m_{\pm}^2, m_{\mp}^2)|^2 + 2\kappa r_B^{(*)} Re(A_D(m_{\mp}^2, m_{\pm}^2)A_D^*(m_{\pm}^2, m_{\mp}^2)e^{i(\delta_B^{(*)} \mp \gamma)}) \tag{5.1}$$

where $m_{\mp}^2$ is the squared invariant mass of the $K_S\pi^{\mp}$ combination, $A_D(m_-^2, m_+^2)$ is the $D^0 \to K_S\pi^-\pi^+$ decay amplitude, $r_B^{(*)}$ and $\delta_B^{(*)}$ are the amplitude ratio and relative strong phase between the amplitudes $B^- \to \bar{D}^{(*)0}K^-$ and $B^- \to D^{(*)0}K^-$ and κ takes the value $+1$ for $B^- \to \tilde{D}^0K^-$ and $B^- \to \tilde{D}^{*0}(\tilde{D}^0\pi^0)K^-$, and -1 for $B^- \to \tilde{D}^{*0}(\tilde{D}^0\gamma)K^-$.

The likelihood obtained from Eq. 5.1 permits to extract directly the CP parameters $r_B^{(*)}$, $\delta_B^{(*)}$ and γ, but it is effected to large non Gaussian effects. For a relatively small dataset and for a small value of $r_B^{(*)}$, the likelihood fit returns a biased estimate of $r_B^{(*)}$ and of the r.m.s of $\delta_B^{(*)}$ and γ. This is due to the fact that $\sigma^2(\gamma)$ is proportional to $1/(d^2logL/d^2\gamma)$ and $d^2logL/d^2\gamma$ is proportional to $r_B^{(*)}$, therefore it will be smaller for larger $r_B^{(*)}$. Since $r_B^{(*)}$ is positively biased the error returned by the maximum likelihood fit is smaller than what it should be to represent the statistical fluctuation. Moreover, while the linearity of γ and $\delta^{(*)}$ is verified, $r_B^{(*)}$ saturates at low truth values of $r_B^{(*)}$, with a saturation region depending on the statistical contents of the data sample. The saturation effect goes away with a data sample about ten times larger than one used for this analysis. The nature of these non Gaussian effects, scaling with the size of the data sample, is related to the small number of events in the region of the Dalitz plot sensitive to $r_B^{(*)}$ and γ and to the polar coordinates representation of the space of the fit parameters and, more particularly, to the positive definition of $r_B^{(*)}$. Fig 5.1 shows the value of the error on γ as a function of r_B and the saturation effect of r_B .
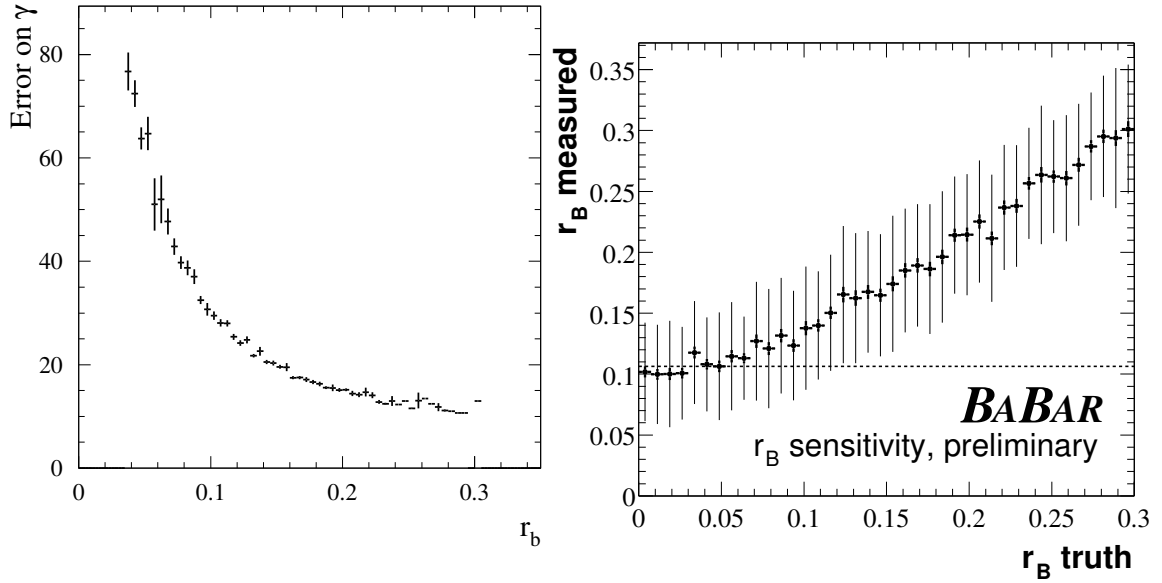
Figure 5.1: **Left:** *Error on γ as a function of r_B.* **Right:** *r_B value obtained in the likelihood fit versus generated r_B.*

To avoid the effects described above the 4-dimensional Cartesian parameter space [1] is defined by the variables $z_\pm = (x_\pm, y_\pm)$, with

$$x_\pm \equiv Re(r_{B\pm}e^{i(\delta \pm \gamma)}) = r_{B\pm}\cos(\delta \pm \gamma)$$
$$y_\pm \equiv Im(r_{B\pm}e^{i(\delta \pm \gamma)}) = r_{B\pm}\sin(\delta \pm \gamma) \tag{5.2}$$

where $\pm$ refers to $B^\pm$ decays. With the choice of this particular basis no physics boundaries have to be imposed to the fit variables and then there will be not non Gaussian effects and biases in the fit results. In addition, Cartesian coordinates are largely uncorrelated, while (r_B, γ, δ) are significantly correlated.

Moreover, the Cartesian coordinates are sensitive to the direct CP violation: the distance d between the measured (x, y) coordinates for B^+ and B^- coordinates is

$$d = [(x_- - x_+)^2 + (y_- - y_+)^2]^{1/2} = 2r_B|\sin\gamma| . \tag{5.3}$$

Therefore a non null distance means evidence of direct CP violation.

In Cartesian coordinates Eq. 5.1 can be written as:

$$\Gamma_\mp(m_-^2, m_+^2) \propto |A_{D\mp}|^2 + r_B^2|A_{D\pm}|^2 + 2\left\{x_\mp Re[A_{D\mp}A_{D\pm}^*] + y_\mp Im[A_{D\mp}A_{D\pm}^*]\right\} \tag{5.4}$$

---

[1]Here it is referred to $B^\pm \to \tilde{D}^0 K^\pm$ decays.

with $A_{D\mp} \equiv A_D(m_{\mp}^2, m_{\pm}^2)$ and $r_B^2 = x_{\mp}^2 + y_{\mp}^2$.

Eq. 5.4 is valid for both $B^{\pm} \to \tilde{D}^0 K^{\pm}$ and $B^{\pm} \to \tilde{D}^{*0} K^{\pm}$ decays. For $B^{\pm} \to \tilde{D}^0 K^{*\pm}$ decays, following what is proposed in [28], the decay rates can be written as:

$$\Gamma_{\mp}(m_-^2, m_+^2) \propto |A_{D\mp}|^2 + r_s^2|A_{D\pm}|^2 + 2\left\{x_{s\mp}Re[A_{D\mp}A_{D\pm}^*] + y_{s\mp}Im[A_{D\mp}A_{D\pm}^*]\right\} \quad (5.5)$$

where

$$x_{s\pm} \equiv Re(\kappa r_{B\pm}e^{i(\delta_s \pm \gamma)}) = \kappa r_{B\pm}\cos(\delta_s \pm \gamma)$$
$$y_{s\pm} \equiv Im(\kappa r_{B\pm}e^{i(\delta_s \pm \gamma)}) = \kappa r_{B\pm}\sin(\delta_s \pm \gamma) \quad (5.6)$$

with $x_{s\mp}^2 + y_{s\mp}^2 = \kappa r_s^2$ and $0 < \kappa < 1$. In the limit of a null $B^{\mp} \to \tilde{D}^0(K_S\pi^{\mp})_{\mathrm{non}-K^*}$ contribution, $\kappa \to 1$, $r_s \to r_b$ and $\delta_s \to \delta$.

5.1 Likelihood fit procedure

To extract the CP parameters a fit procedure in different steps is performed. In order to get from the data sample as many as possible parameters of the PDF shapes a yields fit is performed. Once selection PDF shapes and yields are known, the Dalitz model is added to the likelihood and a fit with only the CP parameters floated is performed.

5.1.1 Likelihood parameterization

The probability density function (PDF) distinguishes the following signal-background components:

Signal(Sig).

Wrong sign signal (SigWS).

Continuum background (Cont), subdivided into two categories:

- real D^0 (D⁰): The PDF distinguishes between real D^0 mesons with a right (RS, i.e. the D^0 is seen as D^0) or a wrong (WS, i.e. the D^0 is seen as $\bar{D}^0$) sign random bachelor track. This splitting is needed in order to account for the misinterpretation of D^0 decays as $\bar{D}^0$, which is relevant for the Dalitz structure. As the background source are continuum events, this component does not contain CP violation (i.e. $r_B = 0$).

- fake D^0 (comb).

$B\bar{B}$ background, subdivided into three categories:

- $D\pi$ for DK events and DK for $D\pi$ events (Dh). This background has different r_B and strong phase δ as the signal, but the same weak phase γ. This background is not present in the case of $B^\pm \to \tilde{D}^0 K^{*\pm}$ decays.

- real D^0's coming from a CP violating channel (like signal) and a combinatorial wrong sign bachelor track from the other B (SigWS, i.e. the D^0 is seen as $\bar{D}^0$). This component has the same CP violation parameters as the signal, but the D^0 is seen as $\bar{D}^0$.

- other than $D\pi/K$ (B$\overline{\text{B}}$). This includes $D^{(*)0}X$ candidates with either a missing particle or a particle from the other B decay, as well as events with a fake (combinatorial) D^0. This background type contains both peaking and non-peaking components (in m_{ES} and ΔE). This category is itself separated into two subtypes:

  - real D^0 (D^0). As before, the PDF distinguishes between real D^0 mesons with a right (RS) or a wrong (WS) sign random bachelor track. By definition this category does not contain CP violating channels (i.e. $r_B = 0$), which have their own component (SigWS);

  - fake D^0 (comb).

The explicit separation of SigWS from $B\bar{B}$ is needed since the $D^0 - \bar{D}^0$ interference (CP violating effects) is different. In the case of SigWS the interference effects are as in the signal (with the D^0 seen as $\bar{D}^0$, and vice versa), while in $B\bar{B}$ the contribution from wrong sign is either non-interfering, or it is different to that of the signal (in case that there are CP violating residual channels).

The overall probability density function $\mathcal{P}^\alpha$ can then be written as:

$$
\begin{aligned}
\mathcal{P}^\alpha = {}& f_{\text{Sig}}\mathcal{P}^\alpha_{\text{Sig}} + f_{\text{Dh}}\mathcal{P}^\alpha_{\text{Dh}} + f_{\text{SigWS}}\mathcal{P}^{\overline{\alpha}}_{\text{SigWS}} + \\
& f_{\text{Cont}}\left\{(1 - R_{\text{Cont}})\mathcal{P}^{\text{comb}}_{\text{Cont}} + R_{\text{Cont}}\left[R^{RS}_{\text{Cont}}\mathcal{P}^\alpha_{\text{Cont}} + (1 - R^{RS}_{\text{Cont}})\mathcal{P}^{\overline{\alpha}}_{\text{Cont}}\right]\right\} + \\
& f_{\text{B}\overline{\text{B}}}\left\{(1 - R_{\text{B}\overline{\text{B}}})\mathcal{P}^{\text{comb}}_{\text{B}\overline{\text{B}}} + R_{\text{B}\overline{\text{B}}}\left[R^{RS}_{\text{B}\overline{\text{B}}}\mathcal{P}^\alpha_{\text{B}\overline{\text{B}}} + (1 - R^{RS}_{\text{B}\overline{\text{B}}})\mathcal{P}^{\overline{\alpha}}_{\text{B}\overline{\text{B}}}\right]\right\}
\end{aligned} \tag{5.7}
$$

for $B^{\pm} \to \tilde{D}^0 K^{\pm}$ and $B^{\pm} \to \tilde{D}^{*0} K^{\pm}$, and

$$
\begin{aligned}
\mathcal{P}^{\alpha} = \ & f_{\mathsf{Sig}}(1 - \kappa_{\mathsf{SigWS}})\mathcal{P}_{\mathsf{Sig}}^{\alpha} + f_{\mathsf{Sig}}\kappa_{\mathsf{SigWS}}\mathcal{P}_{\mathsf{Sig}}^{\overline{\alpha}} + \\
& f_{\mathsf{Cont}}\left\{(1 - R_{\mathsf{Cont}})\mathcal{P}_{\mathsf{Cont}}^{\mathsf{comb}} + R_{\mathsf{Cont}}\left[R_{\mathsf{Cont}}^{RS}\mathcal{P}_{\mathsf{Cont}}^{\alpha} + (1 - R_{\mathsf{Cont}}^{RS})\mathcal{P}_{\mathsf{Cont}}^{\overline{\alpha}}\right]\right\} + \\
& f_{\mathsf{B\overline{B}}}\left\{(1 - R_{\mathsf{B\overline{B}}})\mathcal{P}_{\mathsf{B\overline{B}}}^{\mathsf{comb}} + R_{\mathsf{B\overline{B}}}\left[R_{\mathsf{B\overline{B}}}^{RS}\mathcal{P}_{\mathsf{B\overline{B}}}^{\alpha} + (1 - R_{\mathsf{B\overline{B}}}^{RS})\mathcal{P}_{\mathsf{B\overline{B}}}^{\overline{\alpha}}\right]\right\}
\end{aligned}
\tag{5.8}
$$

for $B^{\pm} \to \tilde{D}^0 K^{*\pm}$. The parameters of Eq. 5.7 and 5.8 represent:

- $\alpha = \mathsf{D}^0, \overline{\mathsf{D}}^0$, and $\overline{\alpha}$ denotes the CP conjugate state of α

- f_j is the fraction for component $j = \mathsf{Sig}, \mathsf{Cont}, \mathsf{Dh}, \mathsf{SigWS}, \mathsf{B\overline{B}}$

- κ_{SigWS} is the fraction of wrong sign signal relative to (right sign) signal

- R_{Cont} ($R_{\mathsf{B\overline{B}}}$) is the fraction of real $D^0/\bar{D}^0$ in Cont ($\mathsf{B\overline{B}}$) background component

- $R_{\mathsf{Cont}}^{\mathsf{RS}}$ ($R_{\mathsf{B\overline{B}}}^{\mathsf{RS}}$) is the fraction of right sign $D^0/\bar{D}^0$ in Cont ($\mathsf{B\overline{B}}$) background component;

- $\mathcal{P}_j^{\alpha}$ is the PDF for component j and real D^0 ($\alpha = \mathsf{D}^0$) or $\bar{D}^0$ ($\alpha = \overline{\mathsf{D}}^0$), while $\mathcal{P}_j^{\mathsf{comb}}$ is the PDF for component j and fake D^0.

5.1.2 Yields fit

Before extracting the CP parameters, a simpler fit can be performed in order to extract the yields (fractions) of the different signal and background components, as well as many as possible selection PDF shape parameters. The explicit dependence of the PDF:

$$
\mathcal{P}_j^{\alpha} \equiv \mathcal{P}_j^{\alpha}(m_{ES}, \Delta E, F) .
\tag{5.9}
$$

The extraction of the component fractions and selection PDF shapes can be then performed using an extended likelihood function

$$
\mathcal{L}_{ext} = \frac{e^{-\eta}\eta^N}{N!} \prod_{\alpha} \prod_{i=1}^{N_{\alpha}} \mathcal{P}^{\alpha}(i)
\tag{5.10}
$$

where $\mathcal{P}^{\alpha}(i)$ is the total PDF given by Eq. (5.7 and 5.8) for event i, $N = N_{\mathsf{D}^0} + N_{\overline{\mathsf{D}}^0}$ is the total number of observed events, and η its expected value according to Poisson statistics. The yields N_j can be calculated simply as $N_j = \eta f_j$, the fractions verifying $\sum_j f_j = 1$.

The multidimensionality of the PDF is factorized assuming that all these variables are uncorrelated for all the components:

$$\mathcal{P}_j^\alpha(m_{ES}, \Delta E, F) = \mathcal{P}_j^\alpha(m_{ES})\mathcal{P}_j^\alpha(\Delta E)\mathcal{P}_j^\alpha(F) \ . \qquad (5.11)$$

It is verified that for the final set of variables and their cuts used in the final fit the correlations are either negligible or have no effect on the measurements. In the case of $B^- \to \tilde{D}^0 K^{*-}$ the variable ΔE are not used in the fit since the main reason to use ΔE in the $B^- \to \tilde{D}^{(*)0} K^-$ analysis is to provide discrimination of the $B^- \to \tilde{D}^{(*)0} \pi^-$ background events and there is no equivalent background in the $B^- \to \tilde{D}^0 K^{*-}$ analysis.

The variable m_D is excluded from the likelihood in order to avoid correlations with the other discriminant variables and a tight cut at 2 sigma of the D^0 mass is applied.

The yields fit is performed separately for $B^- \to \tilde{D}^{(*)0} K^-$ and $B^- \to \tilde{D}^0 K^{*-}$.

For $\boldsymbol{B^- \to \tilde{D}^{(*)0} K^-}$ the $D^0 K$, $(D^0\pi^0)K$, $(D^0\gamma)K$, $D^0\pi$, $(D^0\pi^0)\pi$ and $(D^0\gamma)\pi$ samples are used simultaneously in the ΔE region $[-80, 120]$ ($[20, 80]$) MeV for DK ($D\pi$) samples. For the $D\pi$ samples loose kaon PID veto is applied to remove contamination from kaon sample and to insure that the samples are mutually exclusive. The signal, continuum and $B\bar{B}$ shapes of each $D^0 K$ sample are assumed to be the same as for its $D^0\pi$ sample partner, but are different among the different $D^0 K$ (i.e. $D^0 K$, $D^0\pi^0 K$, $D^0\gamma K$) samples, with two exceptions. First, in the Monte Carlo simulation the ARGUS $B\bar{B}$ parameter for $D^0 K$ and $D^0\pi$ samples are found to be significantly different, therefore they are assumed to be different. Due to the small amount $B\bar{B}$ contamination these parameters are fixed to the values estimated from Monte Carlo in the ΔE signal region, $[-30, 30]$ MeV and $[20, 80]$ MeV for $D^0 K$ and $D^0\pi$ samples. For $D^0 K$ samples the signal ΔE signal range is taken, rather than the full range, to take into account the dependence of the combinatorial $B\bar{B}$ background shape with the ΔE cut, since the final CP fit is performed in the signal ΔE region (as described below). The effect of choosing these values rather than those of the full ΔE range has a negligible effect in the determination of the other shape parameters. The second exception is due to the presence of $B\bar{B}$ m_{ES} peaking background on top of the ARGUS combinatorial shape in the $D^0\pi$ samples only. According to the Monte Carlo simulation the fraction of this type of background with respect to the combinatorial $B\bar{B}$ is about 40%, with a width around 3.4 MeV/c^2. Therefore, in the final fit and only for $D^0\pi$ samples is added a Gaussian to the $B\bar{B}$ background component, allowing to vary the fraction since ΔE provides a handle to separate it. The Fisher shape for signal and
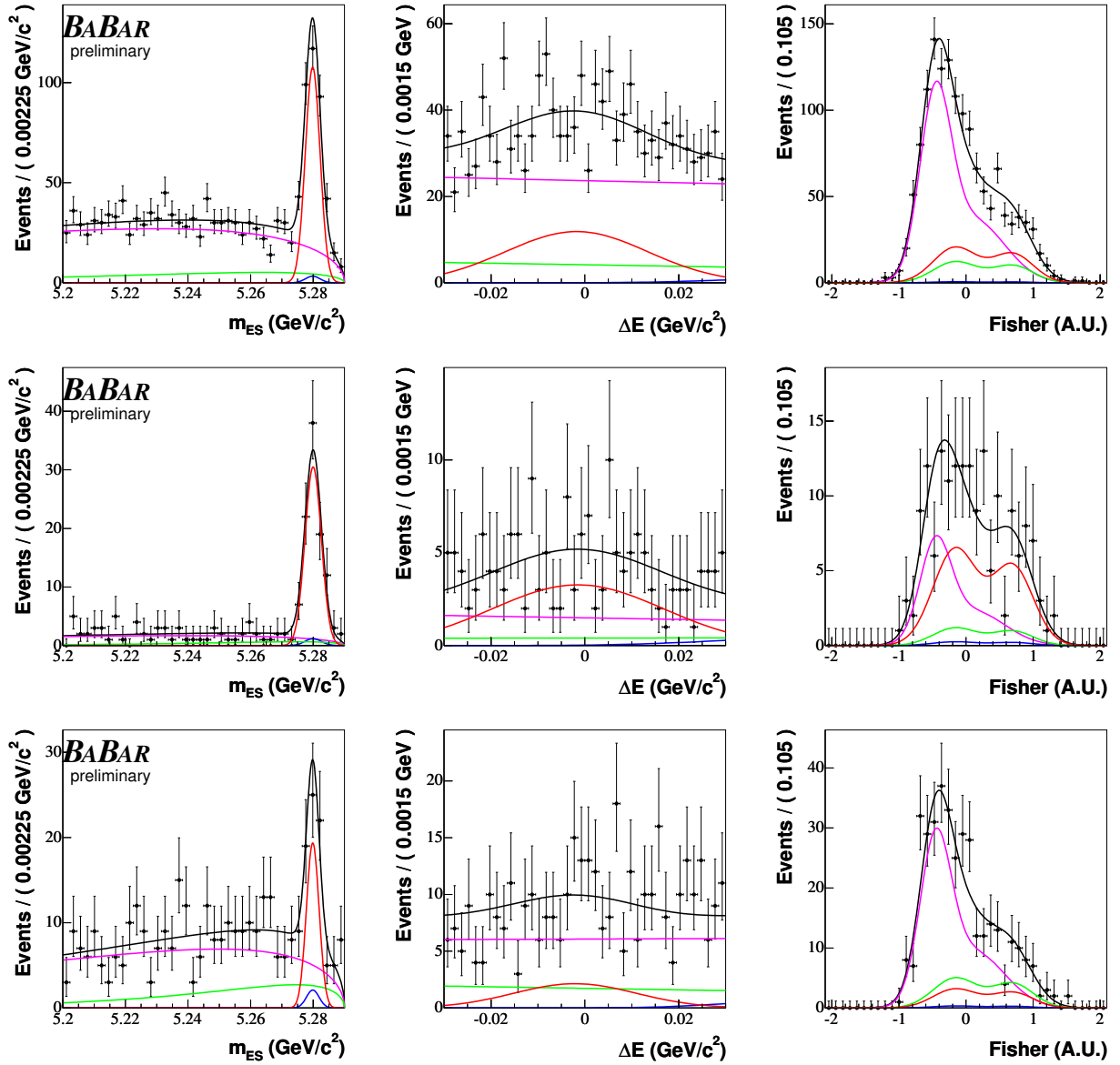
Figure 5.2: D^0K (top row), $(D^0\pi^0)K$ (middle row) and $(D^0\gamma)K$ (bottom row) m_{ES}, ΔE, and Fisher shapes in the ΔE region $[-30, 30]$ MeV, compared to the data. Also shown are the different background components: Sig(red), $D\pi$ (blue), B$\overline{\text{B}}$(green) and Cont(magenta).
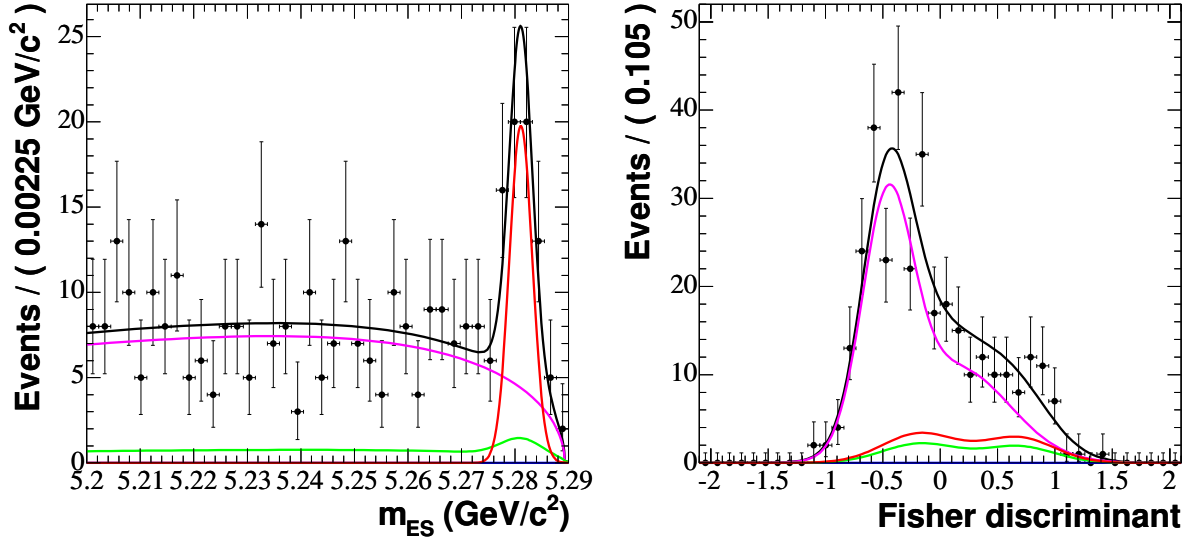
Figure 5.3: $B^- \rightarrow \tilde{D}^0 K^{*-}$ m_{ES}, and Fisher shapes extracted from the fit in the ΔE region $[-25, 25]$ MeV, compared to the data. Also shown are the different background components: Sig(red), B$\overline{\text{B}}$ (green) and Cont(magenta).

continuum is assumed to be common to all decay modes, after checking its consistency among the different samples in the Monte Carlo simulation. The shape for $B\bar{B}$ and Dh background are taken as for the signal. The yields for all the different samples are taken as independent and are floated simultaneously. This also includes the continuum and $B\bar{B}$ yields since the Fisher discriminant provides some separation power. The m_{ES} variable determines the fraction of signal while the Fisher discriminant determines the relative background fractions for continuum and $B\bar{B}$ background events.

For $B^- \rightarrow \tilde{D}^0 K^{*-}$, as said before, the ΔE variable is not used in the fit and the region $[-25, 25]$ MeV is selected. Moreover, since there is no equivalent $B^- \rightarrow \tilde{D}^{(*)0}\pi^-$ channel, only the $D^0 K^*$ sample is used. The m_{ES} shape for the continuum is assumed to be the same for $B^- \rightarrow \tilde{D}^0 K^{*-}$ and $B^- \rightarrow \tilde{D}^{(*)0}\pi^-$, as verified comparing continuum Monte Carlo for both selections. For the signal component a common m_{ES} resolution for $B^- \rightarrow \tilde{D}^0 K^{*-}$ and $B^- \rightarrow \tilde{D}^{(*)0}\pi^-$ is used, while the mean value is taken different in order to accommodate the apparent shift of $\Delta m_{ES} = 1.7$ MeV/c^2 for $B^- \rightarrow \tilde{D}^0 K^{*-}$ data. The ARGUS end point is left floating and assumed to be the same for $B^- \rightarrow \tilde{D}^0 K^{*-}$ and $B^- \rightarrow \tilde{D}^{(*)0}\pi^-$. It was verified that the apparent m_{ES} shift for $B^- \rightarrow \tilde{D}^0 K^{*-}$ does not move the endpoint (this was checked by allowing two independent ARGUS

endpoints). The Fisher discriminant is parameterized using two Gaussians, and the actual values of the parameters for Signal and $B\bar{B}$ component and for continuum are taken from $B^- \to \tilde{D}^{(*)0}\pi^-$ control sample.

The yields extracted from the fit are shown in Tab. 5.1 and 5.2 respectively for $B^- \to \tilde{D}^{(*)0}K^-$ and $B^- \to \tilde{D}^0K^{*-}$. The fit projections for m_{ES}, ΔE, and Fisher for $B^- \to \tilde{D}^{(*)0}K^-$ are shown in Fig. 5.2. The fit projections for m_{ES} and Fisher for $B^- \to \tilde{D}^0K^{*-}$ are shown in Fig. 5.3.

Component	D^0K Yield	$D^0\pi$ Yield
	D^0K	$D^0\pi$
B$\bar{\text{B}}$	480 ± 129	912 ± 139
Cont	3091 ± 137	1968 ± 99
Dh	131 ± 15	3554 ± 122
Sig	292 ± 21	68 ± 33
	$(D^0\gamma)K$	$(D^0\gamma)\pi$
B$\bar{\text{B}}$	305 ± 47	797 ± 85
Cont	735 ± 51	308 ± 38
Dh	21 ± 8	407 ± 76
Sig	42 ± 9	-18 ± 11
	$(D^0\pi^0)K$	$(D^0\pi^0)\pi$
B$\bar{\text{B}}$	98 ± 23	141 ± 39
Cont	199 ± 24	111 ± 20
Dh	27 ± 7	829 ± 41
Sig	94 ± 11	28 ± 20

Table 5.1: *D^0K, $(D^0\pi^0)K$, $(D^0\gamma)K$, $D^0\pi$, $(D^0\pi^0)\pi$ and $(D^0\gamma)\pi$ yields as extracted from the combined shapes fit in the ΔE region $[-80, 120]$ MeV for kaon samples and $[20, 80]$ MeV for pion data.*

Component	D^0K^* Yield
B$\bar{\text{B}}$	31 ± 26
Cont	260 ± 28
Sig	47 ± 9

Table 5.2: *$B^- \to \tilde{D}^0K^{*-}$ yields from PDF shapes fit in Δ in$[-25, 25]$ MeV region.*

5.1.3 Dalitz plot model

When the Dalitz plot model is added, the explicit dependence of the PDF becomes:

$$\mathcal{P}_j^\alpha \equiv \mathcal{P}_j^\alpha(m_{ES}, \Delta E, F)\mathcal{P}_j^\alpha(m_{ab}^2, m_{ac}^2) \tag{5.12}$$

where $\mathcal{P}_j^\alpha(m_{ab}^2, m_{ac}^2)$ is the Dalitz plot dependent part of the PDF.

In the current analysis two models are used to parameterize the Dalitz structure: in the first model the Dalitz amplitude is parameterized with a sum of Breit-Wigner functions (Breit-Wigner model), in the second model the $\pi\pi$ S-wave component of the Dalitz amplitude is replaced by the K-matrix formalism (K-matrix model). A detailed description of both methods is provided in Chapter 3. Even if the K-matrix model takes better into account the dynamic in case of overlapping resonances, and not needs the presence of non-established resonances, the BW model is used for this measurement since the K-matrix model still lacks a complete evaluation of the systematics for all the components of the Dalitz amplitude.

The K-matrix model is used in this analysis, as explained in Sec. 5.3.7 to evaluate the contribution to the systematic error coming from the parameterization of the $\pi\pi$ S-wave of the Dalitz amplitude and in particular from the introduction of the non-established resonances σ and σ'. The K-matrix model will then used in the future as the reference model for the extraction of the CP parameters.

An expression similar to Eq. 5.12 applies for fake D^0, comb, where $\mathcal{P}_j^{\text{comb}}(m_{ab}^2, m_{ac}^2)$ can be configured in a similar way to $\mathcal{P}_j^\alpha(m_{ab}^2, m_{ac}^2)$. The Dalitz shape for combinatorial continuum events is estimated by using off-resonance data, as described in Chapter 4. The correction for $B\bar{B}$ combinatorial background is obtained from Monte Carlo simulation. Note that by definition $\mathcal{P}_{\text{SigWS}}^{\bar{\alpha}}(m_{ab}^2, m_{ac}^2) = \mathcal{P}_{\text{Sig}}^\alpha(m_{ab}^2, m_{ac}^2)$. $\mathcal{P}_j^\alpha(m_{ab}^2, m_{ac}^2)$ for $j = \text{Sig}, \text{Dh}$ contain the $D^0 - \bar{D}^0$ interference (i.e. $r_B \neq 0$), while $\mathcal{P}_j^\alpha(m_{ab}^2, m_{ac}^2)$ for $j = \text{Cont}, \text{B}\bar{\text{B}}$ and $\mathcal{P}_j^{\text{comb}}(m_{ab}^2, m_{ac}^2)$ do not contain $D^0 - \bar{D}^0$ interference ($r_B = 0$). An independent set of CP-violation parameters is considered for $j = \text{B}\bar{\text{B}}$ (by default fixed to zero) in order to study systematic errors induced by residual CP violating channels contributing to the $\text{B}\bar{\text{B}}$ background. The CP violation parameters of the Dh background component are the same as those of the signal of the other π/K bachelor signal mode.

The PDF described in Eq. 5.12 is then used for the extraction of the CP parameters. The $(D^0\pi^0)K$ and $(D^0\gamma)K$ channels can be combined from the point of view of CP physics taking into account the opposite strong phase $(\delta^*(D^0\pi^0) = -\delta^*(D^0\gamma)$, see Sec. 1.4.4) in

order to have more statistics (the different background levels is properly accounted for in the full likelihood). The CP fit is performed to the $B^- \to \tilde{D}^{(*)0}K^-$ samples in the ΔE signal region range $[-30, 30]$ MeV to reduce background contributions, especially from $B^- \to \tilde{D}^{(*)0}\pi^-$ events. Thus the yields are also floated in the CP fit to account for differences with respect to the previous shapes fit due to the different ΔE cut. The fractions of real D^0 and right sign D^0 in both the Cont and B$\overline{\text{B}}$ background components are fixed to the estimates found in Chapter 4. The additional input to the CP fit are the efficiency correction across the Dalitz plot and the Dalitz shape for continuum and BB background, both described in detail in Chapter 4.

5.2   Sensitivity on the angle γ

After the parameterization of the likelihood it is possible to explicitly show which are the regions in the Dalitz plot which contribute the most to the determination of the angle γ. In Gaussian approximation:

$$\sigma^2(\gamma) \propto \frac{1}{\frac{d^2 log(L)}{d^2\gamma}} \qquad\qquad Sensitivity \propto \frac{d^2 log(L)}{d^2\gamma} \qquad (5.13)$$

where L is the likelihood defined in Sec. 5.1.

For this reason a very high statistics Toy Monte Carlo sample of signal events is generated according to the Breit-Wigner model and, event by event, the second derivative with respect to γ of the log-likelihood is evaluated. The result is shown in Figure 5.4 where each event is weighted by the value of the second derivative with respect to γ of the log-likelihood. The region with higher sensitivity on γ is the one where the Cabibbo allowed and double Cabibbo suppressed decays interfere.

5.3   Systematic uncertainties

Since in Cartesian coordinates base the CP parameters have Gaussian behavior, systematic uncertainties can be included very easily just by replacing $\sigma_{x_\pm}$ and $\sigma_{y_\pm}$ by $\sqrt{\sigma_{x_\pm}^2 + \sigma_{x_\pm,syst}^2}$ and $\sqrt{\sigma_{y_\pm}^2 + \sigma_{x_\pm,syst}^2}$, respectively. As the statistical uncertainties dominate yet this measurement and the largest systematic uncertainties are uncorrelated among the samples, it is appropriate to assume that the global correlations $\rho_\pm$ remain unchanged with respect to their statistical values. In any case, it is checked that the
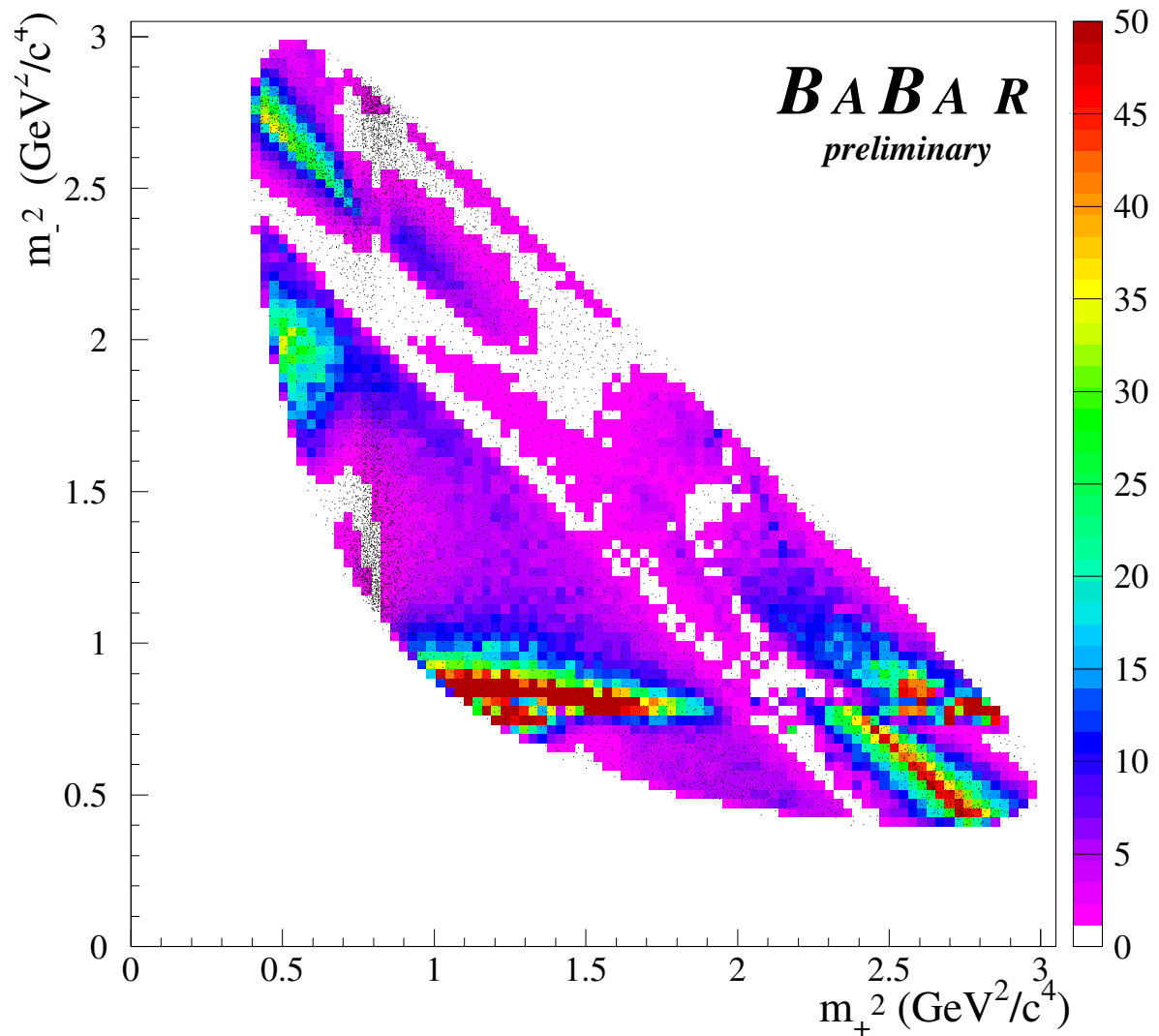
Figure 5.4:   *Dalitz distribution of the very high statistics Toy Monte Carlo sample of signal events. The values used to generate the sample are: $r_B = 0.125$, $\gamma = 75°$, $\delta = -180°$. Each event is entering into the plot with a weight given by the value of the second derivative with respect to γ of the log-likelihood. A maximum value for the weight to be plotted is fixed in order to see in a finer way the structure of the weights over the Dalitz plot. The black points correspond to the same events with weight equal to unity.*

Source	x_+	y_+	x_-	y_-	x_+^*	y_+^*	x_-^*	y_-^*
$m_{ES}, \Delta E, F$ shapes	0.0105	0.0086	0.0088	0.0141	0.0196	0.0218	0.0218	0.0146
Real D^0 fraction	0.0050	0.0047	0.0061	0.0036	0.0035	0.0049	0.0028	0.0032
Right sign D^0's	0.0157	0.0090	0.0070	0.0211	0.0065	0.0163	0.0108	0.0103
Eff. in the Dalitz plot	0.0078	0.0085	0.0089	0.0119	0.0067	0.0119	0.0040	0.0079
Tracking efficiency	0.0082	0.0080	0.0095	0.0123	0.0058	0.0109	0.0051	0.0046
Cont bkg. Dalitz shape	0.0195	0.0096	0.0160	0.0149	0.0133	0.0084	0.0083	0.0046
BB bkg. Dalitz shape	0.0026	0.0072	0.0069	0.0130	0.0061	0.0098	0.0029	0.0003
Invariant mass resolution	0.0031	0.0023	0.0022	0.0016	0.0031	0.0023	0.0022	0.0016
Dalitz amplitude and phases	0.0012	0.0069	0.0050	0.0033	0.0043	0.0138	0.0079	0.0079
SubTotal	0.0301	0.0226	0.0258	0.0368	0.0275	0.0373	0.0280	0.0223
Dalitz model (CLEO)	0.0317	0.053	0.0187	0.0215	0.0251	0.0676	0.0222	0.0270
Dalitz model (K-Matrix)	0.005	0.007	0.0025	0.0033	0.0031	0.0045	0.0068	0.0061

Table 5.3: *Summary of the contributions to the systematic error in Cartesian coordinates,* $(x_\pm, y_\pm)$ *and* $(x_\pm^*, y_\pm^*)$.

Source	x_{s+}	y_{s+}	x_{s-}	y_{s-}
m_{ES}, F shapes	0.098	0.116	0.079	0.116
Real D^0 fraction	0.028	0.036	0.033	0.025
Right sign D^0's	0.033	0.047	0.032	0.042
Efficiency in the Dalitz plot	0.067	0.091	0.059	0.044
Tracking efficiency	0.008	0.011	0.010	0.012
Background Dalitz shape	0.038	0.091	0.044	0.087
Invariant mass resolution	0.003	0.002	0.002	0.002
Dalitz amplitude and phases	0.004	0.014	0.008	0.008
SubTotal	0.132	0.184	0.118	0.160
Dalitz model (CLEO model)	0.033	0.046	0.034	0.034
Dalitz model (K-matrix)	0.007	0.006	0.008	0.006

Table 5.4: *Summary of the contributions to the systematic error in Cartesian coordinates* $(x_s\pm, y_{s\pm})$.

impact of the correlation on the confidence regions-intervals is very small (this check was performed using the average correlation from Toy MC experiments instead of the values measured in the data). Tab. 5.3 and 5.4 summarize the main systematic uncertainties of the measurement in Cartesian coordinates, for the three decay modes.

5.3.1 m_{ES}, ΔE and Fisher shapes

The effect of fixing the PDF shapes in the CP fit is evaluated by performing a simultaneous PDF shape and CP fit. Since the extraction of the shapes relies mainly on the $D\pi$ sample, the CP and shapes fit is performed simultaneously to the $D^{(*)}K$ or DK^* and $D\pi$ samples, with shapes fixed and floated. The systematics was then taken as the quadratic difference of the errors reported by the two fits. In all cases the difference between the central values of the two fits is well below the statistical difference.

For $B^- \to \tilde{D}^{(*)0}K^-$ the m_{ES} endpoint in the ARGUS parameterization is fixed in the fit to 5.290 GeV/c^2 (the same value is also used as integration limit of the m_{ES} PDF). To estimate the effect of it in the determination of the signal yields and its impact on the CP parameters it is varied by ± 0.5 MeV/c^2. The effect was found to be completely negligible. For $B^- \to \tilde{D}^0 K^{*-}$ the m_{ES} endpoint in the ARGUS parameterization is left floating in the fit.

The effect of fixing in the fit the fraction of peaking $B\bar{B}$ is evaluated. The fraction is varied within the error calculated on signal Monte Carlo. Similarly the effect of fixing the shape (from Monte Carlo estimate) of the $B\bar{B}$ ARGUS parameterization for m_{ES} is evaluated. In all cases the difference between the central values of the two fits is well below the statistical difference.

5.3.2 Background composition

The fraction of real D^0 is estimated from data and Monte Carlo, as explained in Chapter 4, and the two values agree within the errors. The uncertainty due to the fraction of real D^0 in background is estimated by varying this parameter within its statistical error from the D^0 mass fit on data, and then repeating the fit to the data sample. The larger between the half difference between the two fits and the quadratic difference of the fit errors is assigned as systematic uncertainty.

A potential difference in the number of real D^0 in the continuum background between

B^+ and B^- events could fake CP violating effects in the signal. No significant difference between B^+ and B^- is found in Monte Carlo. Nevertheless, any potential effect are taken in account by introducing an independent set of CP parameters for the continuum background with a real D^0. By repeating the nominal fit with this new set of parameters a negligible impact on the CP parameters is found.

The fraction of right sign (RS) D^0's is taken from Monte Carlo simulation. This contribution is estimated from the variation of the CP parameters in the fit to the data sample when a value of 0.5 is assumed instead of the values given in Chapter 4. As before, the larger between the difference of central values and the quadratic difference of fit errors is taken. The change observed on the CP parameters is consistent with the larger between the bias and the rms from a set of Toy MC experiments generated with the nominal value and fit with 0.5.

5.3.3   Dalitz efficiency

To estimate the effect from the Dalitz efficiency the nominal CP fit is repeated by assuming a flat distribution instead of the 3rd order polynomial parameterization given in Chapter 4. In addition, a systematic uncertainty due to tracking and K_S reconstruction efficiency over the Dalitz plot is evaluated by repeating the fit using alternative values of the 3rd order polynomial parameterization coefficients with: i) the tracking efficiency correction applied on the 2 pions from the D^0 decay and the bachelor kaon; and ii) tracking efficiency correction applied to the pions from the K_S decay. In all cases the larger between the difference of central values and the quadratic difference of fit errors are taken. The uncertainties from the two corrections are added quadratically.

5.3.4   Dalitz shape for combinatorial background

The Dalitz shape for combinatorial continuum events is estimated by using off-resonance data, as described in Chapter 4. The correction for $B\bar{B}$ combinatorial background is obtained from Monte Carlo simulation. The systematics from this correction is estimated from the difference on the CP parameters when flat distributions are assumed instead. The larger between the difference of central values and the quadratic difference of fit errors is taken.

5.3.5 Limited mass resolution

The nominal Dalitz model assumes perfect mass resolution. Given that all the resonances present in the $D^0 \rightarrow K_S \pi^- \pi^+$ decay are quite wide compared to the estimated mass resolution (about 4 MeV^2 for a $K_S \pi^+$ mass squared of about 1 GeV^2, the effect is expected to be completely negligible. Only the $\omega(782)$ has an intrinsic width comparable to the mass resolution (about 6 MeV^2 for a squared $\pi^+ \pi^-$ mass of 0.8 GeV^2, but the sensitivity of the CP parameters is in this case suppressed. To evaluate the effect of the limited mass resolution on the Dalitz plot, two different fits are performed to the reweighed signal MC. The first fit used the reconstructed $K_S \pi^+$ and $K_S \pi^-$ masses, while the second was performed with the MC truth masses (perfect resolution). The difference of fit values was taken as our systematic uncertainty. The errors from the fit for the different parameters were basically unchanged between the two fits.

5.3.6 Statistical errors on Dalitz amplitudes and phases

The phases and amplitudes of the Dalitz model are fixed to the values found from the fit to the high statistics $D^{*+} \rightarrow D^0 \pi^+$ control sample described in detail in Chapter 3. The effect coming from the statistical errors on the Dalitz amplitudes and phases is expected to be not large. It is estimated by performing a simultaneous CP and Dalitz fit with all these parameters floated. The uncertainty was taken as the largest value between the difference of central values and the quadratic difference of the errors reported by the two fits. The difference of central values is in all cases consistent with the quadratic difference of the statistical errors.

5.3.7 Dalitz model systematic uncertainty

The systematic uncertainty related to the phenomenological parameterization of the D^0 decay amplitude represents the main systematic error of the analysis. To evaluate it a Toy Monte Carlo technique is used: a great number of Toy Monte Carlo experiments are generated according to the Breit-Wigner Dalitz model. The experiments were then fit using alternative models. To get ride of statistical fluctuations and avoid double counting with the data statistical error, each sample is generated with very hight statistics.

The problem with this technique is which values for $r_B^{(*)}$, r_s, $\delta_B^{(*)}$, δ_s and γ, are used in the generation of the experiments. Given the current large statistical errors taking the
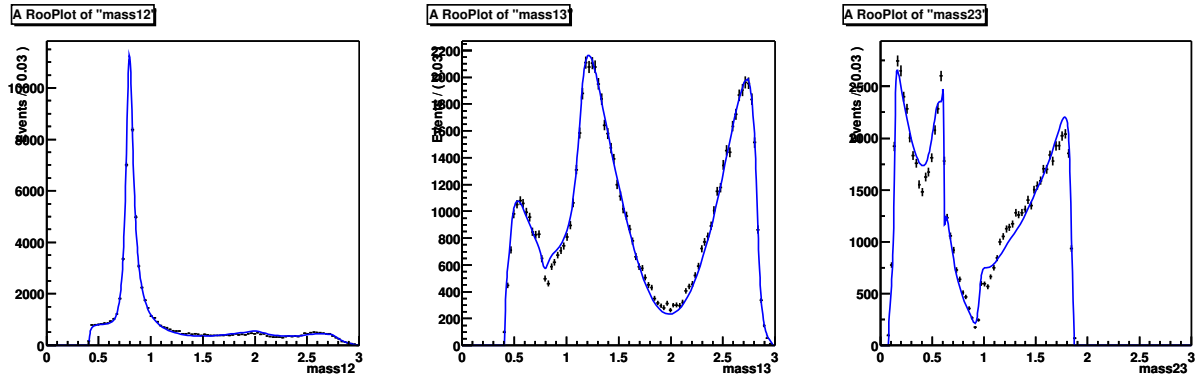
Figure 5.5: *Dalitz analysis projections when the CLEO model is used. the three projections are displayed : Cabibbo allowed $(K_s\pi^-)$, the $(K_s\pi^+)$ and the $(\pi^+\pi^-)$ (from left to right respectively).*

central values would be just a choice among others, especially if the effect turns out to be multiplicative with the generated value. Unfortunately, it is verified that the systematic uncertainty for all Cartesian components evaluated in this way strongly depends with the values of $r_B^{(*)}$, and r_s, and smoothly with the values of $\delta_B^{(*)}$, δ_s and γ.

To avoid this problem each single experiment is generated with all the Cartesian component generated randomly following independent Gaussian distributions with mean and width values as measured in the data; this is possible since the Cartesian coordinates behave almost perfectly as independent Gaussians. The rest of the procedure is identical to what was described above. Taking the systematic uncertainty from the mean and rms of the experiment-by-experiment differences for each component, the result is integrated over the others then represent 1σ interval, independent of all the other variables.

To quote the systematic the CLEO model [42] is used: this model is equivalent to the Breit-Wigner model but excluding the σ, σ', $K_0^*(1430)$ DCS, $K_2^*(1430)$ DCS, $K^*(1410)$, and $\rho(1450)$ resonances. Fig. 5.5 shows a Dalitz fit to the $D^{*+} \rightarrow D^0\pi^+$ control sample using the CLEO model: it is clear that this model doesn't give a good description of the data sample.

Although σ and σ' are not established resonances, they are introduced in the Brit-Wigner Dalitz parameterization to better fit the data distribution. In general all the $(\pi^+\pi^-)$ S-wave contribution is not well described with a sum of Breit-Wigner function. To evaluate the effect of the bad description of the $(\pi^+\pi^-)$ S-wave contribution, the K-matrix model is used. The value of the systematic due to the $(\pi^+\pi^-)$ S-wave is smaller

than the one obtained from the CLEO model, as expected from Fig. 5.4 where the $(\pi^+\pi^-)$ S-wave gives a small sensitivity to the angle γ.

5.4   Results of the CP parameters

Using the likelihood defined in Eq. 5.12 the results of the CP parameter for for $B^- \to \tilde{D}^0 K^-$, $B^- \to \tilde{D}^{*0} K^-$, and $B^- \to \tilde{D}^0 K^{*-}$ are:

$$
\begin{aligned}
x_- \equiv Re(r_{B-}e^{i(\delta-\gamma)}) &= 0.077 \pm 0.069(\text{stat.}) \pm 0.026(\text{exp. syst.}) \pm 0.019(\text{model syst.}) \\
y_- \equiv Im(r_{B-}e^{i(\delta-\gamma)}) &= 0.064 \pm 0.092(\text{stat.}) \pm 0.037(\text{exp. syst.}) \pm 0.042(\text{model syst.}) \\
x_+ \equiv Re(r_{B+}e^{i(\delta+\gamma)}) &= -0.129 \pm 0.070(\text{stat.}) \pm 0.030(\text{exp. syst.}) \pm 0.032(\text{model syst.}) \\
y_+ \equiv Im(r_{B+}e^{i(\delta+\gamma)}) &= 0.019 \pm 0.079(\text{stat.}) \pm 0.023(\text{exp. syst.}) \pm 0.021(\text{model syst.}) \\
x_-^* \equiv Re(r_{B-}^*e^{i(\delta^*-\gamma)}) &= -0.131 \pm 0.093(\text{stat.}) \pm 0.028(\text{exp. syst.}) \pm 0.021(\text{model syst.}) \\
y_-^* \equiv Im(r_{B-}^*e^{i(\delta^*-\gamma)}) &= -0.143 \pm 0.105(\text{stat.}) \pm 0.022(\text{exp. syst.}) \pm 0.025(\text{model syst.}) \\
x_+^* \equiv Re(r_{B+}^*e^{i(\delta^*+\gamma)}) &= 0.140 \pm 0.093(\text{stat.}) \pm 0.028(\text{exp. syst.}) \pm 0.025(\text{model syst.}) \\
y_+^* \equiv Im(r_{B+}^*e^{i(\delta^*+\gamma)}) &= 0.013 \pm 0.120(\text{stat.}) \pm 0.037(\text{exp. syst.}) \pm 0.056(\text{model syst.}) \\
x_{s-} \equiv Re(r_{s-}e^{i(\delta_s-\gamma)}) &= -0.197 \pm 0.201(\text{stat.}) \pm 0.118(\text{exp. syst.}) \pm 0.008(\text{model syst.}) \\
y_{s-} \equiv Im(r_{s-}e^{i(\delta_s-\gamma)}) &= 0.255 \pm 0.303(\text{stat.}) \pm 0.034(\text{exp. syst.}) \pm 0.006(\text{model syst.}) \\
x_{s+} \equiv Re(r_{s+}e^{i(\delta_s+\gamma)}) &= -0.066 \pm 0.234(\text{stat.}) \pm 0.132(\text{exp. syst.}) \pm 0.033(\text{model syst.}) \\
y_{s+} \equiv Im(r_{s+}e^{i(\delta_s+\gamma)}) &= -0.011 \pm 0.324(\text{stat.}) \pm 0.184(\text{exp. syst.}) \pm 0.046(\text{model syst.})
\end{aligned}
$$

Fig. 5.6 shows the 68.3% (dark blue) and 95% (bright blue) confidence-level contours (stat. only) in the $(x_\pm, y_\pm)$ Cartesian fit parameter space for $B^- \to \tilde{D}^0 K^-$, $B^- \to \tilde{D}^{*0} K^-$, and $B^- \to \tilde{D}^0 K^{*-}$. Translate these results in term of the parameters $r_{(s)}^{(*)}$, $\delta_{(s)}^{(*)}$ and γ require a statistical treatment; both frequestist and Bayesian approach are used. The statistical treatment will be discussed in detail in Chapter 6.
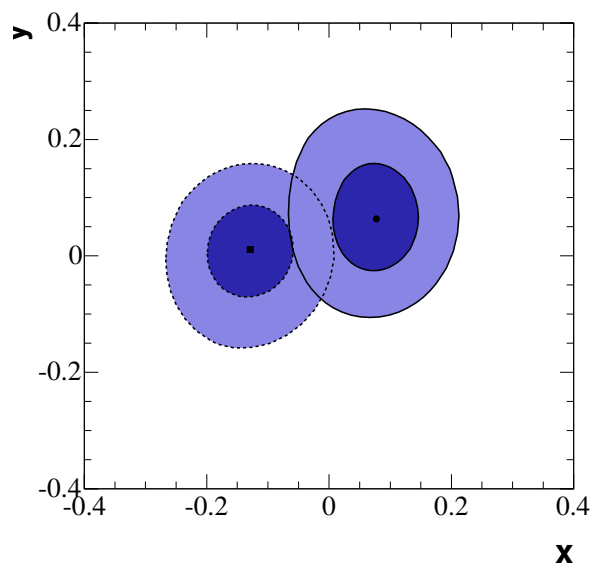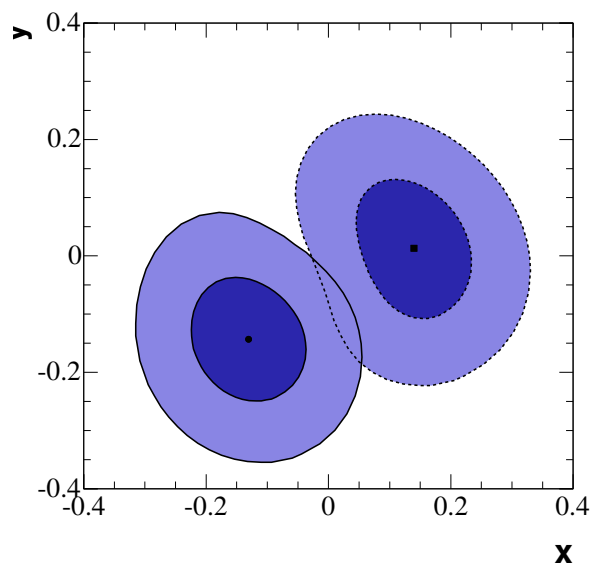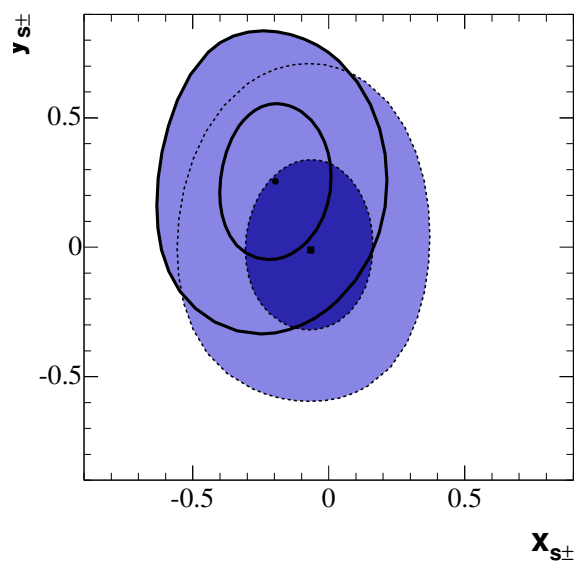
(a) $B^{\pm} \to \tilde{D}^0 K^{\pm}$

(b) $B^{\pm} \to \tilde{D}^{*0} K^{\pm}$

(c) $B^{\pm} \to \tilde{D}^0 K^{*\pm}$

Figure 5.6: *68.3% (dark blue) and 95% (bright blue) confidence-level contours in the* $(x_{\pm}, y_{\pm})$ *Cartesian fit parameter space*

Chapter 6

Interpretation of the results and measurement of γ

In Chapter 5 the results of the CP parameters in Cartesian coordinates (see Eqs. 5.2 and 5.6) for the $B^{\pm} \to \tilde{D}^{(*)} K^{(*)\pm}$ decay modes were provided. Cartesian coordinates were introduced in order to avoid the non Gaussian effects present in the likelihood function of the parameters r_B, δ and γ. Moreover the statistical error on γ depends on the value of r_B, value that results biased in polar coordinates. For these reasons the translation of the results of the CP parameters in term of $r_{(s)}^{(*)}$, $\delta_{(s)}^{(*)}$ and γ requires a statistical treatment; both frequentist and Bayesian approach are used.

6.1   Frequentist interpretation of the results

In the classical (frequentist) approach, the confidence interval $[p_1, p_2]$ for parameter p, whose true value p^t is unknown, is such that has a probability

$$P(p \in [p_1, p_2]) = 1 - \alpha, \tag{6.1}$$

of containing the unknown true value. The limits of the interval, p_1 and p_2, are functions of the measured value of p. In particular the confidence interval will contain the unknown true point p^t in a fraction $1 - \alpha$ of the experiments, or in other words, if the experiment is carried out many times, a fraction $1 - \alpha$ of those experiments will find the measured point within the given confidence region. If Eq. (6.1) is satisfied, than the defined interval *covers* at the stated confidence level, or that the interval has the correct *coverage*. In the case of this analysis the confidence level is not 1-dimensional but 3-dimensional or

7-dimensional as the unknown vector parameters of parameters is:

$$\mathbf{p}^{\mathrm{t}} = (r_B^t, \gamma^t, \delta^t) \qquad \text{or} \qquad \mathbf{p}^{\mathrm{t}} = (r_B^t, \gamma^t, \delta^t, r_B^{*t}, \delta^{*t}, r_s^t, \delta_s^t) \ . \tag{6.2}$$

The 3-dimensional (7-dimensional) confidence level regions determined are $\alpha = 19.9\%$, 72.1% (0.52%, 22.02%) corresponding to 1, 1.96 standard deviations respectively for each single parameter (regardless the others), in the case of a 3-dimensional (7-dimensional) Gaussian distribution or equivalently, χ^2 distribution with 3 (7) degrees of freedom.

Finally for the statistical error on the single parameter is quoted the one corresponding to the 19.9% confidence region (1 standard deviation ellipsoid). The methodology used requires knowledge of the probability density function, PDF, of the fitted parameters $\mathbf{z}$, as a function of the true parameters $\mathbf{p}^{\mathrm{t}}$. This PDF can be obtained using toy MC techniques, where large sets of experiments are generated and fitted using the full experimental likelihood function $\mathcal{L}_{exp}$.

6.1.1 Description of the method

Since the Cartesian fit parameter space presents a Gaussian and linearity behavior an analytical parameterization of the PDF can be constructed:

$$\begin{aligned}
\frac{d^4P}{d^2\mathbf{z}_+ d^2\mathbf{z}_-}(\mathbf{z}_+, \mathbf{z}_-|\mathbf{p}^{\mathrm{t}}) &= G_2\left(\mathbf{z}_+; r_B^t \cos(\delta^t + \gamma^t), r_B^t \sin(\delta^t + \gamma^t), \sigma_{x_+}, \sigma_{y_+}, \rho_+\right) \times \\
&\quad G_2\left(\mathbf{z}_-; r_B^t \cos(\delta^t - \gamma^t), r_B^t \sin(\delta^t - \gamma^t), \sigma_{x_-}, \sigma_{y_-}, \rho_-\right)
\end{aligned} \tag{6.3}$$

where

$$G_2\left(\mathbf{z}; \mu_x, \mu_y, \sigma_x, \sigma_y, \rho\right) = \frac{1}{2\pi\sigma_x\sigma_y\sqrt{1-\rho^2}} e^{-\frac{1}{2(1-\rho^2)}\left[\frac{(x-\mu_x)^2}{\sigma_x^2} + \frac{(y-\mu_y)^2}{\sigma_y^2} - \frac{2\rho(x-\mu_x)(y-\mu_y)}{\sigma_x\sigma_y}\right]} \tag{6.4}$$

and $\mathbf{z}_\pm = (x_\pm, y_\pm)$ and $\mathbf{p} = (r_B, \gamma, \delta)$. The vectors $\mathbf{z}_\pm^{\mathrm{t}}$ and $\mathbf{p}^{\mathrm{t}}$, defined equivalently to $\mathbf{z}_\pm$ and $\mathbf{p}$ respectively, are the corresponding parameters in the truth parameter space. The Gaussian widths ($\sigma_{x_\pm}$, $\sigma_{y_\pm}$) and the correlations $\rho_\pm$ (all the other correlations are neglected) distributions can obtained either from the full experimental likelihood $\mathcal{L}_{exp}$ Toy MC experiments or from the fit to the data sample itself, since the agreement with the values found in data is very good.

Once the PDF of the fit parameters is constructed as a function of the true parameters, the technical procedure to construct 3-dimensional confidence regions and their 1- and

2-dimensional is as follows. The confidence level $1 - \alpha$ for each set of true parameters $\mathbf{p}^\mathrm{t}$ is calculated as

$$\alpha(\mathbf{p}^\mathrm{t}) \;=\; \int_D \frac{d^4 P}{d^2 \mathbf{z}_+ d^2 \mathbf{z}_-}(\mathbf{z}_+, \mathbf{z}_-|\mathbf{p}^\mathrm{t}) d^2 \mathbf{z}_+ d^2 \mathbf{z}_- \; , \tag{6.5}$$

where the integration domain D (the confidence region) is given by the condition

$$\frac{d^4 P}{d^2 \mathbf{z}_+ d^2 \mathbf{z}_-}(\mathbf{z}_+, \mathbf{z}_-|\mathbf{p}^\mathrm{t}) \geq \frac{d^4 P}{d^2 \mathbf{z}_+ d^2 \mathbf{z}_-}(\mathbf{z}_+^\mathrm{data}, \mathbf{z}_-^\mathrm{data}|\mathbf{p}^\mathrm{t}) \; , \tag{6.6}$$

i.e. it includes all points in the fit parameter space closer to the truth point than the data point. The values of $\mathbf{z}_\pm^\mathrm{data}$ are those given in section 5.4.

To construct the 3-dimensional confidence region ($\mathbf{p}^\mathrm{t}$ space) a large set of points are generated $\mathbf{p}^\mathrm{t} \equiv (r_B^t, \gamma^t, \delta^t)$, in the ranges $[0, 0.4]$, $[-180°, 180°]$ and $[0, 360°]$. For each generated point $\mathbf{p}^\mathrm{t}$ the integral $\alpha(\mathbf{p}^\mathrm{t})$ is evaluated according to equations 6.5 and 6.6.

To build a 3-dimensional region of joint probability $1 - \alpha_0$, only those points for which $\alpha(\mathbf{p}^\mathrm{t}) \leq \alpha_0$ are selected. The 2-dimensional and 1-dimensional contours are then built by projecting the 3-dimensional joint probability regions. The values $\alpha_0 = 0.19875, 0.72092$ correspond to the 1 and 1.96 standard deviations 3-dimensional ellipsoids, thus the 1-dimensional projections represent the 1 and 1.96 standard deviations of each individual parameter (1.96σ corresponds to a 95% probability content for the case of a 1-dimensional Gaussian distribution [41, 56]) regardless the other parameters. These values of α_0 are the cumulative (upper) integral of a χ^2 probability distribution for $\chi^2 = 1^2, 1.96^2$ and $\nu = 3$ degrees of freedom [41, 56].

This procedure results in a confidence domain with the minimum possible area and so has maximum power to exclude alternative hypotheses. The integral 6.5 with the contour condition given by Eq. 6.6 can be evaluated numerically, but an analytical evaluation is also possible by performing a change of variable to 4-dimensional hyper-spheric coordinates.

The Neyman's freedom to define the likelihood ordering offers also the possibility to use alternatively the likelihood ordering proposed in [57] instead of that given in Eq. (6.6). In this paper it is raised the issue of under-coverage produced by the usual orderings, like the one used here, when measured parameters are bounded by physical limits. In addition to the alternative ordering proposed by Feldman and Cousins [57], a possible way out (also pointed out in their paper) is to allow the measured parameters to take unphysical values. This requires knowing the PDF for non-physical values, which often

Parameter	1σ	1.96σ
r_B	[0.051,0.184]	[0,0.238]
γ	[33,108] [213,288]	–
δ	[67,142] [247,322]	–
r_B^*	[0.090,0.248]	[0.027,0.318]
γ^*	[36,106] [216,286]	[11,140] [191,320]
δ^*	[262,332] [82,152]	[234,363] [54,183]

Table 6.1: *The 1σ (1.96σ) intervals for r_B, δ, γ (D^0K) and r_B^*, γ^* and δ^* ($D^{*0}K$). For γ and δ the ± 180 degree solution is also indicated.*

raises conceptual problems. However, in this analysis this problem is not present since the fit parameter space (Cartesian coordinates) is not bounded. Obviously, this does not imply that the chosen and that of Feldman-Cousins provide exactly the same confidence regions (this is the inherent freedom to the Neyman's definition) but both provide regions with the correct statistical coverage.

6.1.2 1- and 2-dimensional projections of confidence regions for D^0K, $D^{*0}K$ and D^0K^*

Applying this procedure separately to D^0K, $D^{*0}K$ and D^0K^*, and projecting in 1 and 2 dimensions the projections of the 3-dimensional regions of $1 - \alpha_0$ joint probability is obtained. Figs. 6.1 and 6.2 show the 2-dimensional projections of the the 19.9% (dark blue) and 72.1% (bright blue) confidence-level 3-dimensional regions for the D^0K and $D^{*0}K$ modes. Similarly, figures 6.4 and 6.5 show the 1-dimensional projections, which correspond to 1 and 1.96 standard deviation of each single parameter, regardless the values of the others. The small statistic of the D^0K^* signal sample is not sufficient to put significant constraints on the γ value itself: only the ($kr_s - \gamma$) 2-dimensional projection is shown in Fig. 6.3.

In the 1-dimensional projections the projection of the PDF is also shown. Notice that both the 2- and 1-dimensional projections show the $\pm 180°$ ambiguity in $\gamma^{(*)}$ and $\delta^{(*)}$. The probability density functions for r_B and r_B^* show clearly the non-Gaussian behavior and the poor sensitivity to small values as expected.

Table 6.1 reports numerically the one dimensional 1σ and 1.96σ intervals The results include the intrinsic two fold ambiguity for $\gamma^{(*)}$ and $\delta^{(*)}$.
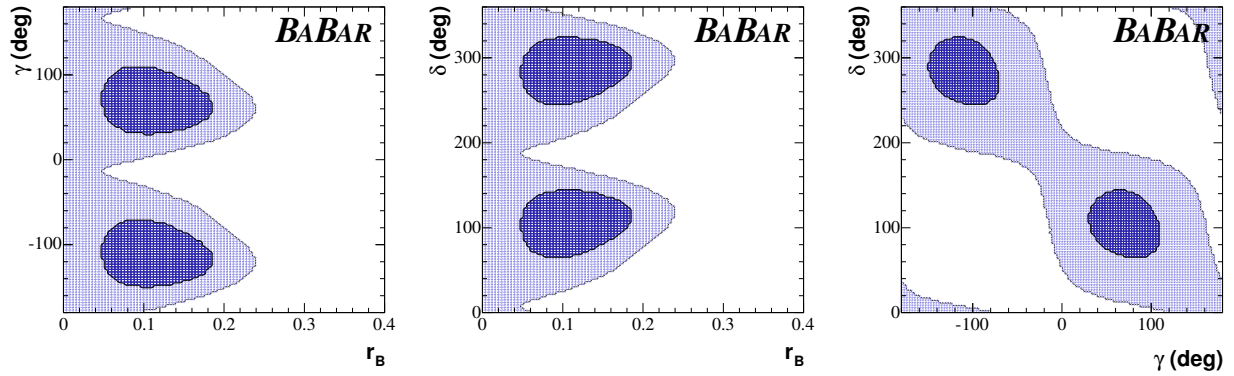
Figure 6.1: *2-dimensional projections of the 19.9% (dark blue) and 72.1% (bright blue) confidence-level 3-dimensional regions for the $D^0 K$ mode.*
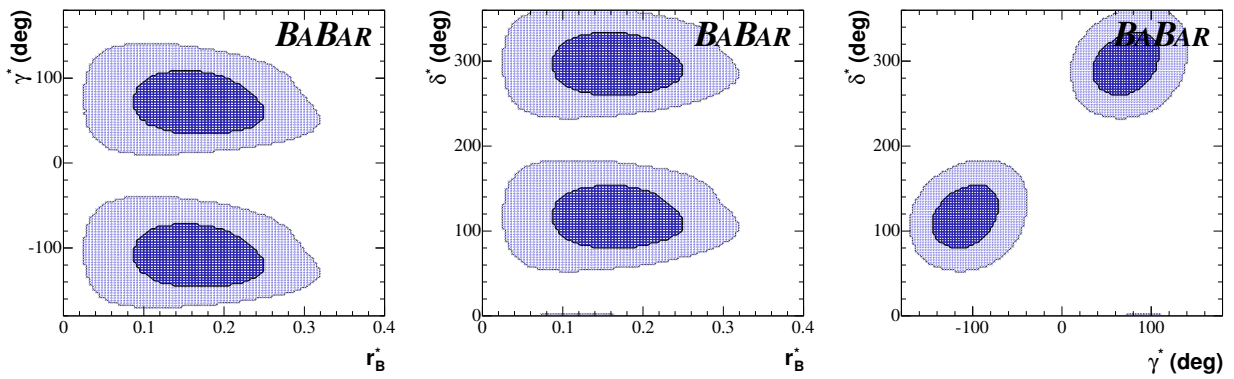

Figure 6.2: *2-dimensional projections of the 19.9% (dark blue) and 72.1% (bright blue) confidence-level 3-dimensional regions for the $D^{*0} K$ mode.*
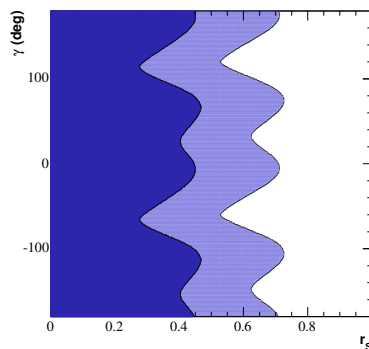

Figure 6.3: *Two-dimensional projections of the 19.9% (dark blue) and 72.1% (bright blue) confidence-level 3-dimensional regions in the $kr_s - \gamma$ plane for $D^0 K^*$.*
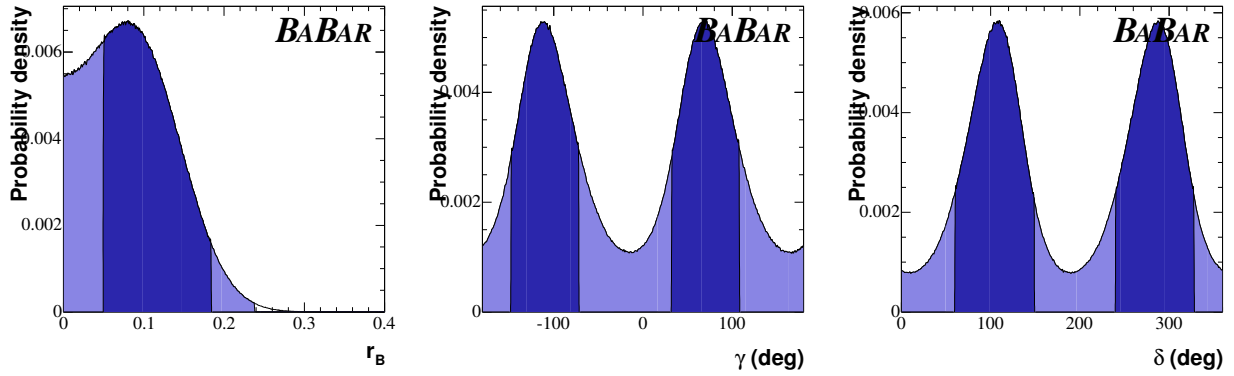
Figure 6.4: *Probability density functions for r_B, γ and δ together with the 1-dimensional projections of the 19.9% (dark blue) and 72.1% (bright blue) confidence-level 3-dimensional regions for the D^0K mode.*
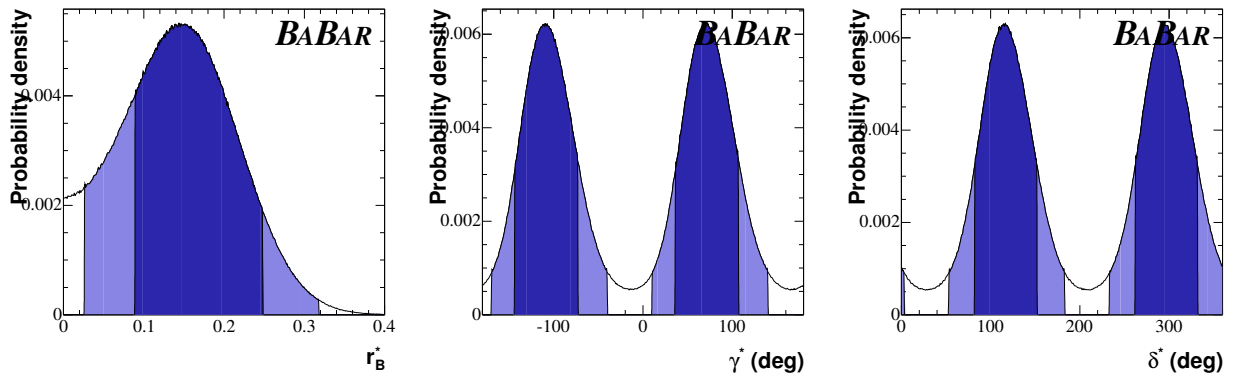

Figure 6.5: *Probability density functions for r_B^*, γ and δ^* together with the 1-dimensional projections of the 19.9% (dark blue) and 72.1% (bright blue) confidence-level 3-dimensional regions for the $D^{*0}K$ mode.*

6.1.3 Combination of D^0K, $D^{*0}K$ and D^0K^* decay modes

In order to obtain a more accurate measurement of γ the D^0K, $D^{*0}K$ and D^0K^* decay modes are combined. The used method for the combination of the results is identical to that used for each B decay mode separately, but now there are seven true parameters $\mathbf{p}^t=$ $(r_B^t, \gamma^t, \delta^t, r_B^{*t}, \delta^{*t}, r_s^t, \delta_s^t)$ and an 12-dimensional Cartesian space for the measured parameters $(\mathbf{z}_\pm, \mathbf{z}_\pm^*, \mathbf{z}_{s\pm}) = (x_\pm, y_\pm, x_\pm^*, y_\pm^*, x_{s\pm}, y_{s\pm})$. The PDF in this case reads

$$\frac{d^{12}P}{d^2\mathbf{z}_+ d^2\mathbf{z}_- d^2\mathbf{z}_+^* d^2\mathbf{z}_-^* d^2\mathbf{z}_{s+} d^2\mathbf{z}_{s-}}(\mathbf{z}_+, \mathbf{z}_-, \mathbf{z}_+^*, \mathbf{z}_-^*, \mathbf{z}_{s+}, \mathbf{z}_{s-}|\mathbf{p}^t) = \tag{6.7}$$

$$\frac{d^4P}{d^2\mathbf{z}_+ d^2\mathbf{z}_-}(\mathbf{z}_+, \mathbf{z}_-|r_B^t, \gamma^t, \delta^t) \times \frac{d^4P}{d^2\mathbf{z}_+^* d^2\mathbf{z}_-^*}(\mathbf{z}_+^*, \mathbf{z}_-^*|r_B^{*t}, \gamma^t, \delta^{*t}) \times \frac{d^4P}{d^2\mathbf{z}_{s+} d^2\mathbf{z}_{s-}}(\mathbf{z}_{s+}, \mathbf{z}_{s-}|r_s^t, \gamma^t, \delta_s^t) \, .$$

The confidence level $1 - \alpha$ for each set of true parameters $\mathbf{p}^t$ is now calculated as

$$\alpha(\mathbf{p}^t) = \int_D \frac{d^{12}P}{d^2\mathbf{z}_+ d^2\mathbf{z}_- d^2\mathbf{z}_+^* d^2\mathbf{z}_-^* d^2\mathbf{z}_{s+} d^2\mathbf{z}_{s-}}(\mathbf{z}_+, \mathbf{z}_-, \mathbf{z}_+^*, \mathbf{z}_-^*, \mathbf{z}_{s+}, \mathbf{z}_{s-}|\mathbf{p}^t)$$

$$d^2\mathbf{z}_+ d^2\mathbf{z}_- d^2\mathbf{z}_+^* d^2\mathbf{z}_-^* d^2\mathbf{z}_{s+} d^2\mathbf{z}_{s-} \, , \tag{6.8}$$

where the integration domain D (the confidence region) is given by the condition

$$\frac{d^{12}P}{d^2\mathbf{z}_+ d^2\mathbf{z}_- d^2\mathbf{z}_+^* d^2\mathbf{z}_-^* d^2\mathbf{z}_{s+} d^2\mathbf{z}_{s-}}(\mathbf{z}_+, \mathbf{z}_-, \mathbf{z}_+^*, \mathbf{z}_-^*, \mathbf{z}_{s+}, \mathbf{z}_{s-}|\mathbf{p}^t) \geq$$

$$\frac{d^{12}P}{d^2\mathbf{z}_+ d^2\mathbf{z}_- d^2\mathbf{z}_+^* d^2\mathbf{z}_-^* d^2\mathbf{z}_{s+} d^2\mathbf{z}_{s-}}(\mathbf{z}_+^{\text{data}}, \mathbf{z}_-^{\text{data}}, \mathbf{z}_+^{*\,\text{data}}, \mathbf{z}_-^{*\,\text{data}}, \mathbf{z}_{s+}^{\text{data}}, \mathbf{z}_{s-}^{\text{data}}|\mathbf{p}^t) \, . \tag{6.9}$$

Fig. 6.6 shows the two-dimensional projections in the $r_B^{(*)} - \gamma$ and $kr_s - \gamma$ planes for D^0K, $D^{*0}K$ and D^0K^*. The errors are statistical plus experimental systematics. The region of 1 (2) sigma equivalent 7D-ellipsoid corresponds to the one where αC is smaller than 0.52% (22.02%)

The combination yields

$$\gamma = (67 \pm 28 \pm 13 \pm 11)^\circ \, , \tag{6.10}$$

where the first error is statistical, the second is the experimental systematic uncertainty and the third reflects the Dalitz model uncertainty. The contribution to the Dalitz model uncertainty due to the description of the $\pi\pi$ S-wave in $D^0 \to K_S\pi^-\pi^+$ is 3°.

From this combination kr_s is constrained to be < 0.50 (0.75) at one (two) standard deviation level. It is worth noting that the value of kr_s depends on the selected phase space region of $B^- \to D^-(K_S\pi^-)$ events without introducing any bias on the extraction of γ.
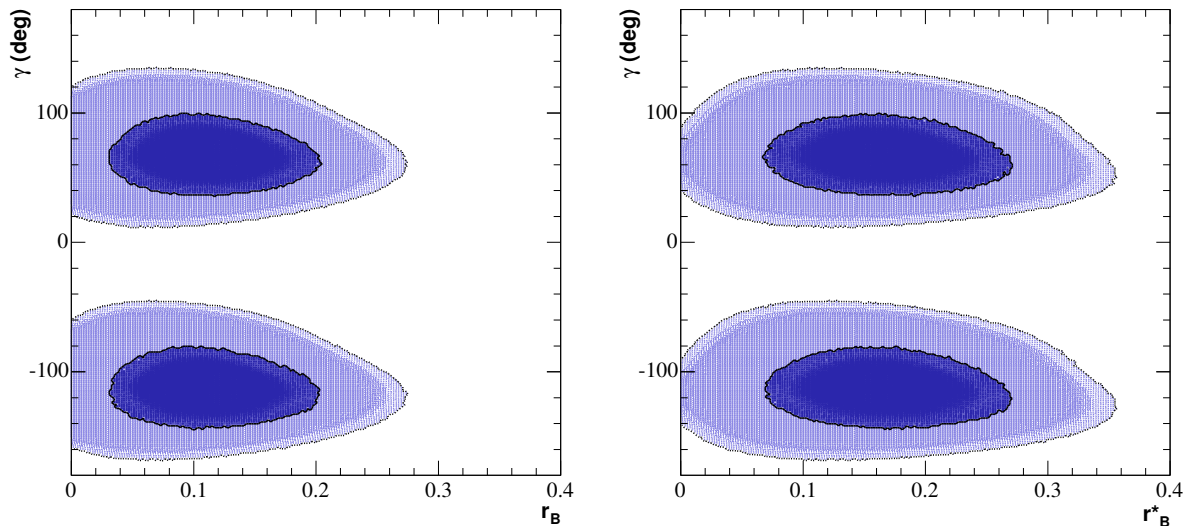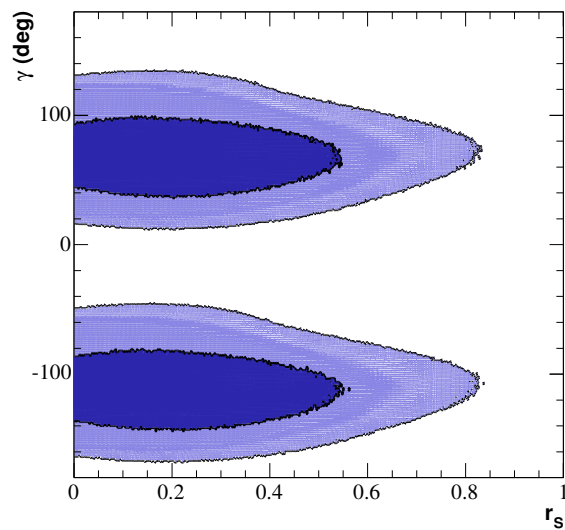
(a) $B^- \to \tilde{D}^0 K^-$

(b) $B^- \to \tilde{D}^{*0} K^-$

(c) $B^- \to \tilde{D}^0 K^{*-}$

Figure 6.6: *Two-dimensional projections in the* $r_B^{(*)} - \gamma$ *and* $kr_s - \gamma$ *planes of the seven-dimensional one- (dark) and two- (light) standard deviation regions, for* $D^0 K$, $D^{*0} K$ *and* $D^0 K^*$.

6.2 Bayesian interpretation of the results

The Bayesian interpretation of the results was used for the first measurement of γ with the D^0K and $D^{*0}K$ decay modes. It doesn't make use of the Cartesian coordinates since Bayesian approach, using the information of the complete likelihood function, is independent on the shape of the likelihood then is not affected by non Gaussian effects. Moreover the effect of the bias on r_B is completely irrelevant for γ and δ measurements since no use is made of the concept of fitted r_B value.

The likelihood function is interpreted as a probability density function for the truth parameters, a correct estimator can be given by the average value of each parameter according to its own PDF. This method to obtain an *a posteriori* distribution for each parameter requires an *a priori* distribution, which is assumed flat in the space of polar coordinates.

6.2.1 Description of the method

The estimation of the confidence regions/intervals with the Bayesian approach requires the evaluation of the likelihood function $\mathcal{L}_{exp} \equiv \mathcal{L}_{exp}(r_B, \gamma, \delta)$ in the whole range of definition of r_B, γ and δ, $[0, 1]$, $[-\pi, \pi]$ and $[0, 2\pi]$, respectively, with the yields floated at each given CP point. The estimate of the confidence region for the CP parameters implies a choice of a priori distribution. A uniform a priori distribution is assumed for each of the CP parameters r_B, γ and δ.

The confidence region $D(\mathcal{C})$ at a given $\mathcal{C}$ confidence level the region in $\gamma - r_B$ space is defined as:

$$\frac{\int_{D(\mathcal{C})} dr_B d\gamma \int_0^{2\pi} d\delta \mathcal{L}_{exp}(r_B, \gamma, \delta)}{\int_0^1 \int_{-\pi}^{\pi} \int_0^{2\pi} \mathcal{L}_{exp}(r_B, \gamma, \delta)\, dr_B d\gamma d\delta} = \mathcal{C} \ . \tag{6.11}$$

The $D(\mathcal{C})$ definition is arbitrary (this is always the case for confidence region), it is chosen to define it by starting the integration procedure by the maximum of the likelihood function and by requiring that the likelihood value at any point in the boundary of D be the same (integration over all likelihood values larger than the value at the boundary). Notice that this can easily give disjoint region.

Similarly it is possible to define the 1-dimensional confidence interval at $\mathcal{C}$ confidence

Parameter	68% CL (stat. only)	95% CL (stat. only)	Central value with error (1σ)
γ	[-147,-65] [33,114]	[-180,-23] [-2,157] [179,180]	70 ± 44
γ^*	[-140,-72] [41,108]	[-172,-31] [9,148]	73 ± 35
δ	[74,155] [253,335]	[0,13] [189,192] [212,360]	114 ± 41
δ^*	[89,157] [269,337]	[0,16] [55,195] [234,360]	303 ± 34
r_B	[0.01,0.13]	[0,0.19]	$0.087^{+0.041}_{-0.074}$
r_B^*	[0.08,0.22]	[0,0.27]	$0.155^{+0.070}_{-0.077}$
γ (combined)	[-132,-83] [48,97]	[-156,-50] [23,130]	70 ± 26

Table 6.2: *Bayesian confidence intervals for $\gamma^{(*)}$, $\delta^{(*)}$ and $r_B^{(*)}$ (statistical only). Angles are given in degree. The Bayesian confidence intervals for the combination of the $D^0 K$ and $D^{*0} K$ channels is also given. In the last column the central values with 1σ errors are also reported. For the $\gamma^{(*)}$ and $\delta^{(*)}$ intervals the $\pm 180°$ solution is also indicated. For the central values the expectation value using the experimental likelihood is quoted, and the 1σ error is given by the 68% confidence limit region around the expectation value. For the phases the errors is symmetrized taking the largest between the positive and negative errors.*

level for, say, r_B, as

$$\frac{\int_{I(\mathcal{C})} dr_B \int_{-\pi}^{+\pi} d\gamma \int_0^{2\pi} d\delta \mathcal{L}_{exp}(r_B, \gamma, \delta)}{\int_0^1 \int_{-\pi}^{\pi} \int_0^{2\pi} \mathcal{L}_{exp}(r_B, \gamma, \delta) \, dr_B d\gamma d\delta} = \mathcal{C} \ , \tag{6.12}$$

where again $I(\mathcal{C})$ can be a set of disjoint interval. In this way it is expected that such intervals have the correct coverage. Notice that the effect of the bias on r_B is completely irrelevant for γ and δ measurements (no use is made of the concept of fitted r_B value).

6.2.2   1- and 2-dimensional confidence regions for $D^0 K$ and $D^{*0} K$

Fig. 6.7 shows the confidence region for $\gamma^{(*)}$ versus $r_B^{(*)}$, for $D^0 K$ and $D^{*0} K$. The red region is the 68% CL region while the yellow one is the 95% CL. Similarly, figures 6.8 and 6.9 show the confidence regions for $\gamma^{(*)}$ versus $\delta^{(*)}$ and $\delta^{(*)}$ versus $r_B^{(*)}$, for $D^0 K$ and $D^{*0} K$. Figs. 6.10 and 6.11 show the probability density functions for $r_B^{(*)}$, $\gamma^{(*)}$ and $\delta^{(*)}$ for $D^0 K$ and $D^{*0} K$, respectively, obtained by integrating the experimental likelihood for all the values of the other variables: $\gamma^{(*)}$, $\delta^{(*)}$; $r_B^{(*)}$, $\delta^{(*)}$; and $r_B^{(*)}$, $\gamma^{(*)}$.

On the same figures the confidence intervals at 68% (red) and 95% (yellow) CL are shown. Notice that the likelihood distribution is nicely showing the $\pm \pi$ ambiguity in $\gamma^{(*)}$ and $\delta^{(*)}$. The probability density function for $r_B^{(*)}$ shows clearly the non-Gaussian behavior as expected, showing the poor sensitivity to small values of $r_B^{(*)}$.
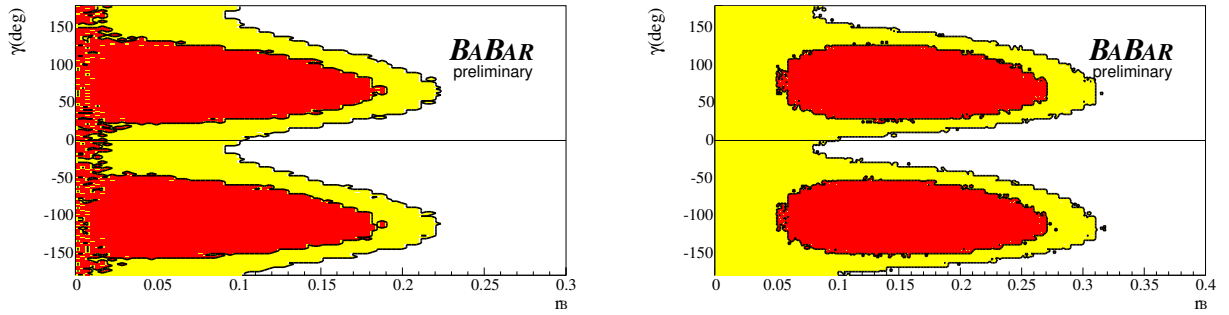
Figure 6.7: *68% (red) and 95% (yellow) Bayesian confidence region in $\gamma^{(*)} - r_B^{(*)}$ plane for D^0K (left) and $D^{*0}K$ (right).*
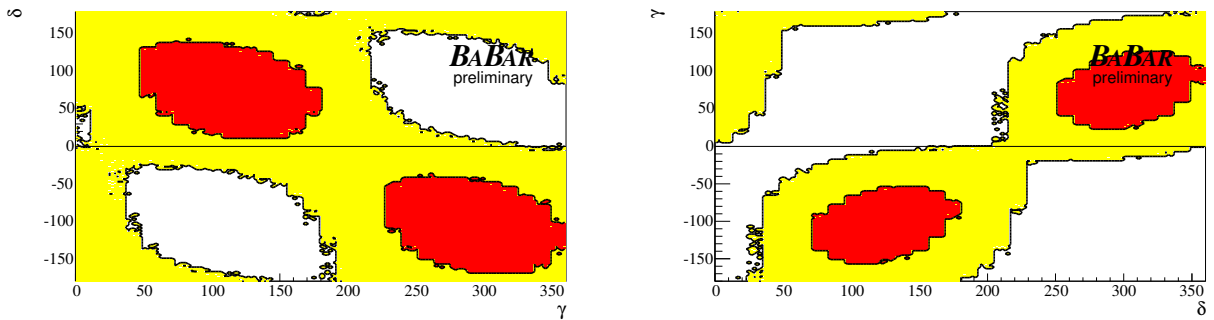

Figure 6.8: *68% (red) and 95% (yellow) Bayesian confidence region in $\gamma^{(*)} - \delta^{(*)}$ plane for D^0K (left) and $D^{*0}K$ (right).*
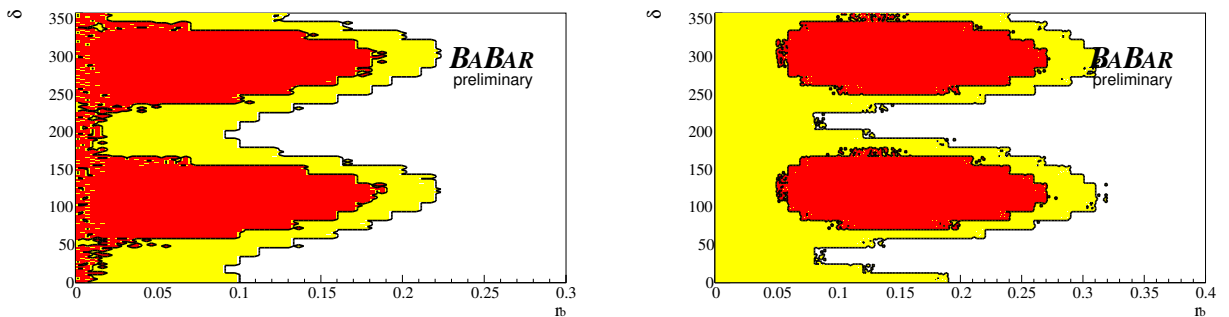

Figure 6.9: *68% (red) and 95% (yellow) Bayesian confidence region in $\delta^{(*)} - r_B^{(*)}$ plane for D^0K (left) and $D^{*0}K$ (right).*
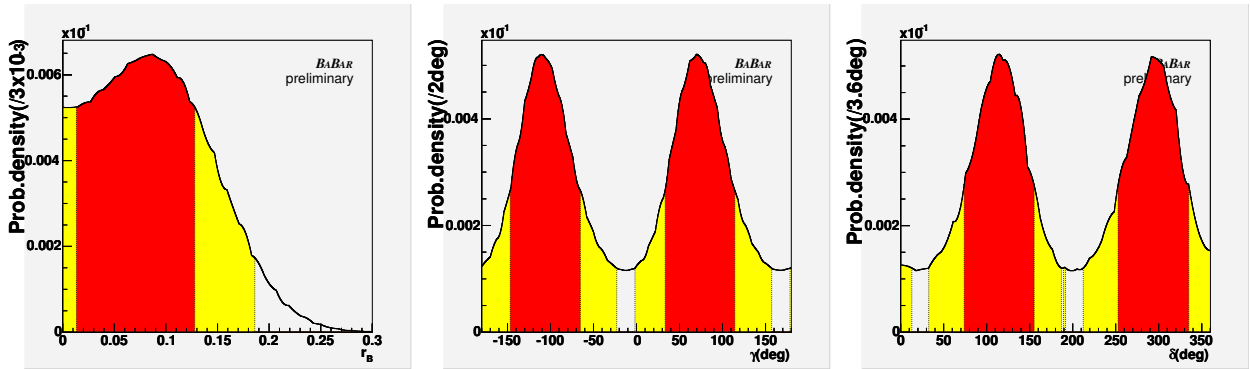
Figure 6.10: *Probability density functions for r_B, γ and δ for $D^0 K$. 68% (red) and 95% (yellow)Bayesian confidence intervals are shown.*
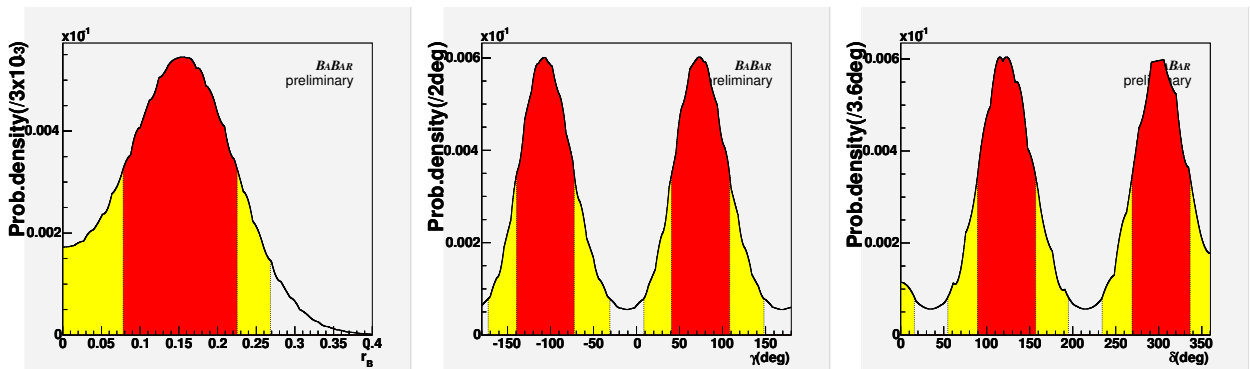

Figure 6.11: *Probability density functions for r_B^*, γ^* and δ^* for $D^{*0} K$. 68% (red) and 95% (yellow) Bayesian confidence intervals are shown.*
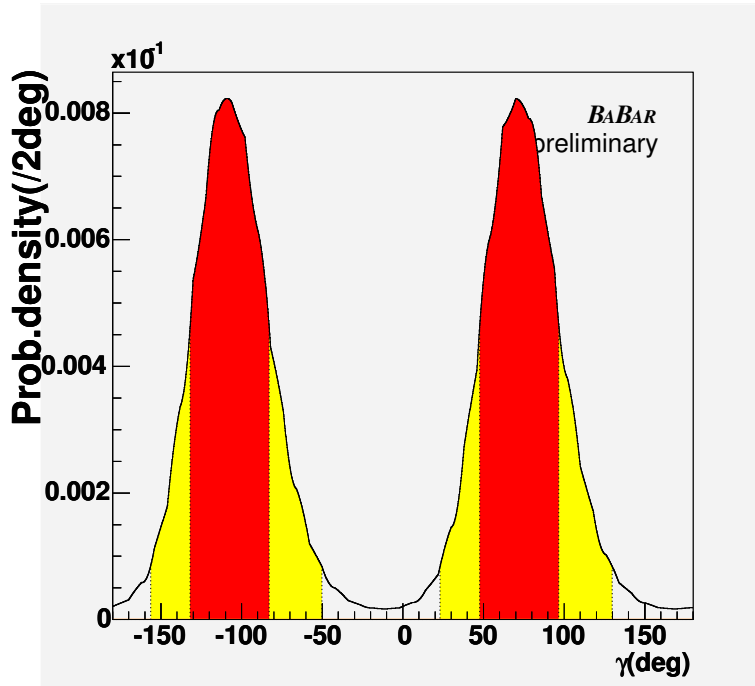
Figure 6.12: *Probability density function for γ for the $D^0 K - D^{*0} K$ combination. 68% (red) and 95% (yellow) Bayesian confidence intervals are shown.*

Tab. 6.2 reports the confidence intervals for the various parameters (statistical only). For the central values the expectation value using the experimental likelihood is quoted, and the 1σ error is given by the 68% confidence limit region around the expectation value. For the phases the errors is symmetrized taking the largest between the positive and negative errors. The results include the intrinsic two fold ambiguity for the weak and strong phases.

Fig. 6.12 shows the probability density function for γ from the combination of the $D^0 K$ and $D^{*0} K$ likelihoods, integrated over r_B, r_B^*, δ and δ^*. The combination of the $D^0 K$ and $D^{*0} K$ likelihoods yields

$$\gamma = (70 \pm 26 \pm 10 \pm 10)^\circ, \tag{6.13}$$

where the first error is statistical, the second is the experimental systematic uncertainty and the third reflects the Dalitz model uncertainty.
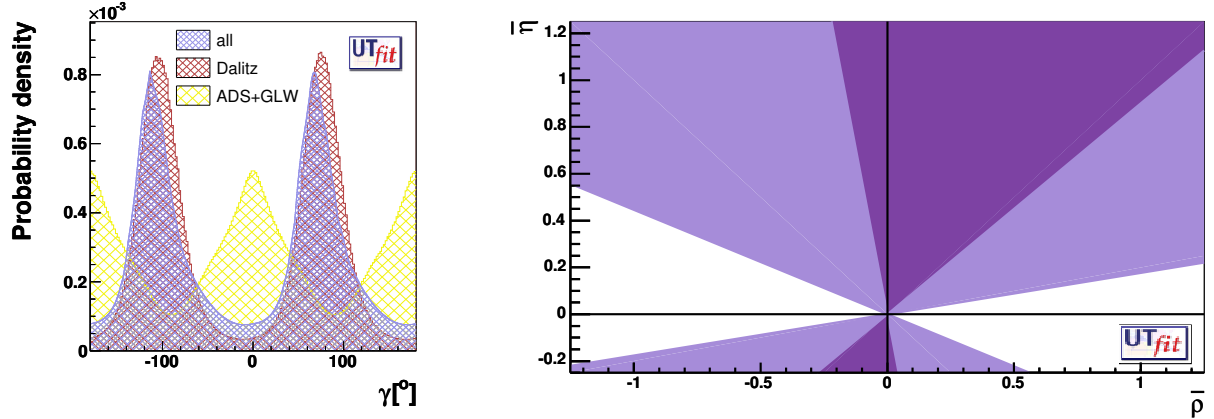
Figure 6.13: **Left:** *comparison of total γ distribution of BaBar results from $D^0 K$, $D^{*0} K$ and $D^0 K^*$ to Dalitz and ADS+GLW methods alone [9].* **Right:** *bound from $D^0 K$, $D^{*0} K$ and $D^0 K^*$ decays with present measurements from BaBar using all the methods [9].*

6.3   Final results and constraint on the $\bar{\rho}, \bar{\eta}$ plane

Starting from the results of the CP parameters in Cartesian coordinates given in Sec. 5.4 using a frequentist method the following values for $\delta_B^{(*)}$ and $r_B^{(*)}$ are found:

$$\delta = 104(284)° \pm 45°(\text{stat.})^{+17°}_{-21°}(\text{exp. syst.})^{+16°}_{-24°}(\text{model syst.})\ \ [0°, 360°]\ ,$$

$$\delta^* = 296(116)° \pm 41°(\text{stat.})^{+14°}_{-12°}(\text{exp. syst.}) \pm 15°(\text{model syst.})\ \ [0°, 360°]\ ,$$

$$r_B = 0.118 \pm 0.079(\text{stat.}) \pm 0.034(\text{exp. syst.})^{+0.036}_{-0.034}(\text{model syst.})\ \ [0, 0.277]\ ,$$

$$r_B^* = 0.169 \pm 0.096(\text{stat.})^{+0.030}_{-0.028}(\text{exp. syst.})^{+0.029}_{-0.026}(\text{model syst.})\ \ [0, 0.352]\ .$$

The small statistic of the $D^0 K^*$ signal sample is not sufficient to put significant constraints on the γ, δ and r_s values.

Combining the $D^0 K$, $D^{*0} K$ and $D^0 K^*$ decays γ results:

$$\gamma = (67 \pm 28 \pm 13 \pm 11)°\ , \tag{6.14}$$

where the first error is statistical, the second is the experimental systematic uncertainty and the third reflects the Dalitz model uncertainty. The contribution to the Dalitz model uncertainty due to the description of the $\pi\pi$ S-wave in $D^0 \to K_S \pi^- \pi^+$ is valuated using the K-matrix Dalitz fit and found to be $3°$.

These results agree fairly well with those obtained using a Bayesian technique with flat prior for γ, $\delta^{(*)}$ and $r_B^{(*)}$.
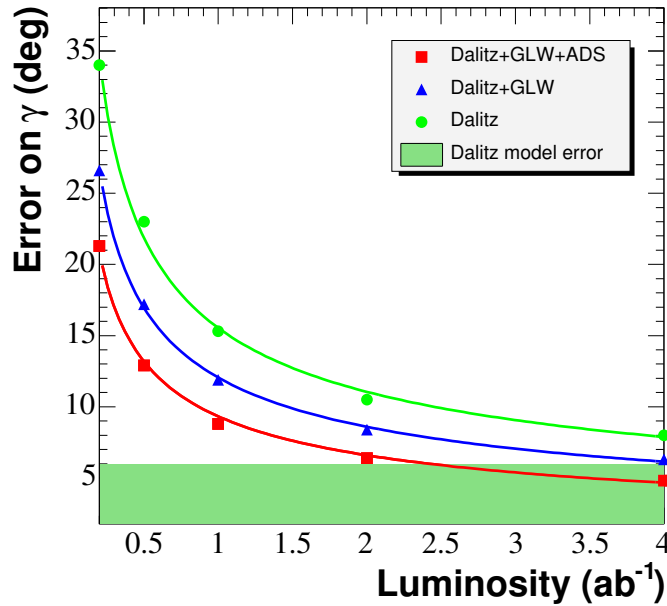
Figure 6.14: Projected errors on γ for the combination of several methods and all decay modes described in the text, for $r_B = 0.1$.

Fig. 6.13 shows the γ posterior probability density function obtained from [9] with a Bayesian approach comparing the $BaBar$ results from $D^0 K$, $D^{*0} K$ and $D^0 K^*$ to Dalitz and ADS+GLW methods alone and the selected $(\bar{\rho}, \bar{\eta})$ region from the $BaBar$ measurements with all methods.

The current measurement of the angle γ is still dominated from the statistic. The larger contribution to the systematic error comes from the Dalitz model uncertainty. This contribution will be sensibly reduced when the K-matrix fit will contain the complete evaluation of the systematics for all the component of the Dalitz amplitude and will become the only model used for the γ measurement. Since the statistical error of γ depends by the value of $r_B^{(*)}$ and no precise measurement of $r_B^{(*)}$ exists it is difficult to project the error on γ with the increasing of the integrated luminosity. Fig. 6.14 shows the projected errors on γ for both the Dalitz method alone and the combination of all methods assuming $r_B = 0.1$: the points correspond to the values obtained with simulations, the curve is the smoothed expectation obtained from a fit to those points assuming a $1/\sqrt{\int L dt} + constant$ scaling with integrated luminosity. The horizontal band is the Dalitz model uncertainty ($\approx 6°$). Note that for the assumed r_B, the Dalitz model systematic uncertainty will not be a limiting factor, for both the Dalitz method alone and the combination of all methods.

Conclusions

This thesis presents a measurements of γ from the Dalitz analysis of the $\tilde{D}^0 \to K_S \pi^- \pi^+$ decays in $B^- \to \tilde{D}^{(*)} K^-$ decays. Using a frequentist approach the following value of γ is found:

$$\gamma = (67 \pm 28 \pm 13 \pm 11)^\circ \; ,$$

where the first error is statistical, the second is the experimental systematic uncertainty and the third reflects the Dalitz model uncertainty.

These results agree fairly well with those obtained using a Bayesian technique with flat prior for γ, $\delta^{(*)}$ and $r_B^{(*)}$.

For the measurement of γ the Dalitz amplitude is parameterized as a sum of relativistic Breit-Wigner resonances (Breit-Wigner model). This parameterization gives a large systematic uncertainty to the measurement of γ and in general cannot give a satisfactory parameterization of the $D^0 \to K_S \pi^- \pi^+$ amplitude since it works well only in the case of narrow, isolated resonances. This is not true in the case of the $\pi\pi$ S-wave of the $D^0 \to K_S \pi^- \pi^+$ decay amplitude.

A second parameterization of the $D^0 \to K_S \pi^- \pi^+$ Dalitz amplitude is performed using The K-matrix formalism for the $\pi\pi$ S-wave (K-matrix model). This parameterization is used to evaluate the contribution to the systematic uncertainty due to the non correct description of the $\pi\pi$ S-wave. This contribution is found to be 3°.

The contribution to the systematic error that comes from the Dalitz model uncertainty, that now is the larger contribution, will be sensibly reduced when the K-matrix fit will contain the complete evaluation of the systematic error and the K-matrix model will become the only model used for the γ measurement.

The K-matrix Dalitz fit has also proved that the two scalar resonances σ and σ' are not necessary for the parameterization of the $\pi\pi$ S-wave component and that they appear only when a Breit-Wigner model is used.

The current measurement of the angle γ is still dominated by the statistic. With the increase of integrated luminosity recorded by the $BaBar$ detector the studies performed on the K-Matrix will become critical to reduce the error.

With higher statistic the model independent approach will become useful for the measurement of γ. In this perspective the measurement from CLEO$-$C of the parameter c_i and s_i of Eq. 1.54 will help to reduce the statistical error.

The only D^0 decay mode considered so far is $D^0 \rightarrow K_S\pi^-\pi^+$ since it is the one that provides the best sensitivity on γ because of its resonance structure. Other modes, such as $D^0 \rightarrow K_S K^- K^+$, even if less sensitive on γ, will help to reduce the statistical uncertainty.

Bibliography

[1] J. H. Christenson, J. W. Cronin, V. L. Fitch and R. Turlay, Phys. Rev. Lett. **13**, 138 (1964).

[2] *BABAR* Collaboration, B. Aubert *et al.*, Phys. Rev. Lett. **89**, 201802 (2002); *BELLE* Collaboration, K. Abe *et al.* Phys. Rev. D **66**, 071102 (2002).

[3] S.L. Glashow, Nucl. Phys. **22** (1961) 579;
S. Weinberg, Phys. Rev. Lett. **19** (1967) 1264;
A. Salam, in *Proc. 8th Nobel Symp.*, ed. N. Swartholm,
Almquist and Wiksells, Stockholm (1968).

[4] P. W. Higgs, Phys. Lett. **12**, 132 (1964).

[5] N. Cabibbo, Phys. Rev. Lett. **10** (1963) 531.

[6] M. Kobayashi and T. Maskawa, Prog. Th. Phys. **49** (1973) 652.

[7] L. Wolfenstein, Phys. Rev. Lett. **51** (1983) 1945.

[8] G. Buchalla, A. J. Buras and M. E. Lautenbacher, Rev. Mod. Phys. **68**, 1125 (1996) [arXiv:hep-ph/9512380].

[9] M. Bona *et al.* [UTfit Collaboration], arXiv:hep-ph/0501199. For the last updates http://www.utfit.org.

[10] T. Inami and C.S. Lim, Prog. Theor. Phys. **65** (1981) 297; *ibid.* **65** (1981) 1772.

[11] A.J. Buras, M. Jasmin and P.H. Weisz, *Nucl. Phys.* **B347** (1990) 491.

[12] S. Herrlich and U. Nierste, *Nucl. Phys.* **B419** (1994) 192;
G. Buchalla, A.J.Buras and M.E. Lautenbacher, *Rev. Mod. Phys.* **68**, (1996) 1125.

[13] M. Battaglia *et al.*, "The CKM matrix and the unitarity triangle". Proceedings Workshop, Geneva, Switzerland, February 13-16, 2002 arXiv:hep-ph/0304132.
Proceedings of the Second Workshop on the CKM Unitarity Triangle, hosted by the SLAC eConf service, with identifier eConf C0304052 (2003).
CKM 2005 Workshop, http://ckm2005.ucsd.edu/index_main.html.

[14] Heavy Flavor Averaging Group http://www.slac.stanford.edu/xorg/hfag

[15] XXII International Symposium on Lepton-Photon Interactions at High Energy, http://lp2005.tsl.uu.se/ lp2005/

[16] P. Harrison and H.R. Quinn, *The BaBar Physics Book*, SLAC-R-504 (1998).

[17] M. Gronau, D. Wyler, Phys. Rev. Lett. **B253** (1991) 483.

[18] M. Gronau, D. London, Phys. Rev. Lett. **B265** (1991) 172.

[19] I. Dunietz, Phys. Rev. Lett. **B270** (1991) 75;
I. Dunietz, Phys. Rev. Lett. **D52** (1995) 3048.

[20] D. Atwood, I. Dunietz and A. Soni, Phys. Rev. Lett. **78**, 3257 (1997) [arXiv:hep-ph/9612433].

[21] Dalitz R.H., Phil. Mag. **44**, 1068 (1953).

[22] A. Giry, Yu. Grossman, A. Soffer, J. Zupan, Phys. Rev. D **68**, 054018 (2003).

[23] Y. Grossman, A. Soffer and J. Zupan, Phys. Rev. D **72**, 031501 (2005)

[24] A. Soffer, arXiv:hep-ex/9801018.

[25] M. Gronau, Y. Grossman and J. L. Rosner, Phys. Lett. B **508**, 37 (2001) [arXiv:hep-ph/0103110].

[26] J. P. Silva and A. Soffer, Phys. Rev. D **61**, 112001 (2000) [arXiv:hep-ph/9912242].

[27] A. Bondar and T. Gershon, Phys. Rev. D **70** (2004) 091503 [arXiv:hep-ph/0409281].

[28] M. Gronau, *Phys. Lett.* **B557**, 198-206 (2003).

[29] E.P. Wigner, Phys. Rew. **70** (1946) 15.

[30] E.P. Wigner and L.Eisenbud, Phys. Rew. **72** (1947) 29.

[31] R.H. Dalitz and S. Tuan, Ann. Phys. **10** 1960 307.

[32] W.Heisemberg, Z.Phy. **120** (1943) 513

[33] K.L. Au, D. Morgan, M.R. Penningtom, Phys. Rew. D**35** (1987) 1633

[34] JP Cummings, DP Weygand - Brookhaven Report BNL-64637, unpublished (1997) - phy.bnl.gov

[35] J. Blatt and V.E. Weisskopf, Theoretical Nuclear Physics, Willey (N.Y.) (1952),p.361

[36] F.v. Hippel and C. Quigg, Phys. Rev **5** (1972) 624

[37] I. J. R. Aitchison, Nucl. Phys. **A189**, 417 (1972).

[38] *BaBar* Collaboration, B. Aubert *et al.*, Nucl. Instr. and Methods **A479**, 117 (2002).

[39] P. Billoir, Nucl. Instr. and Meth. A **225** (1984) 225.

[40] D.N. Brown, E.A. Charles, D.A. Roberts, The *BaBar* Track Fitting Algorithm, *Proceedings of CHEP 2000*, Padova, Italy (2000).

[41] Particle Data Group, S. Eidelman *et al.*, Phys. Lett.**592**, 1 (2004).

[42] CLEO Collaboration, S. Kopp *et al.*, Phys. Rev. D **63**, 092001 (2001); H. Muramatsu *et al.*, Phys. Rev. Lett. **89**, 251802 (2002),Erratum-ibid: **90**, 059901 (2003).

[43] G.J. Gounaris and J.J. Sakurai, Phys. Rev. Lett. **21**, 244 (1968).

[44] Belle Collaboration, K. Abe *et al.*, hep-ph/0308043, contributed to 21st *International Symposium on Lepton and Photon Interactions at High Energies* (LP 03), Batavia, Illinois, 11-16 Aug. 2003.

[45] Review on Scalar Mesons in Ref. [41].

[46] V. V. Anisovich and A. V. Sarantev, Eur. Phys. Jour. A **16**, 229 (2003).

[47] FOCUS Collaboration, J. M. Link *et al.*, Phys. Lett. B**585**, 200 (2004). One should note that there is a misprint of the $(1 - s_{A0})$ factor in the Adler zero expression.

[48] S. L. Adler, Phys. Rev. **137**, B1022 (1965).

[49] V. V. Anisovich and A. V. Sarantev, private communication.

[50] W. Dunwoodie, private communication.

[51] G. C. Fox and S. Wolfram, Nucl. Phys B **149** (1979) 413

[52] S. Brandt, Ch. Peyrou, R. Sosnowski, and A. Wroblewski, Phys. Lett. B **12**, 57 (1964); E. Fahri, Phys. Rev. Lett. **39**, 1587 (1977).

[53] R. A. Fisher, Annals of Eugenics **7** (1936) 179; M. S. Srivastava and E. M. Carter, North Holland, Amsterdam (1983).

[54] *ARGUS* Collaboration, H. Albrecht *et al.*, Z. Phys. C **48**, 543 (1990).

[55] Aubert et al.(BaBar Collaboration), (hep-ex/0508001).

[56] G. Zech, (hep-ex/0106023).

[57] G.J. Feldman and R.D. Cousins, Phys. Rev. D **57** 3873 (1998).